

THESIS

STEADY-STATE CIRCULATIONS FORCED BY DIABATIC HEATING AND WIND  
STRESS IN THE INTERTROPICAL CONVERGENCE ZONE

Submitted by

Alex Omar Gonzalez

Department of Atmospheric Science

In partial fulfillment of the requirements

for the Degree of Master of Science

Colorado State University

Fort Collins, Colorado

Fall 2011

Master's Committee:

Advisor: Wayne H. Schubert

Eric D. Maloney

Don J. Estep

## ABSTRACT

### STEADY-STATE CIRCULATIONS FORCED BY DIABATIC HEATING AND WIND STRESS IN THE INTERTROPICAL CONVERGENCE ZONE

A number of studies have shown the importance of using idealized models to gain insight into large-scale atmospheric circulations in the tropics, especially when investigating phenomena that are not well understood. The recent discovery of the Shallow Meridional Circulation (SMC) in the tropical East Pacific and West Africa is a perfect example of a phenomenon that is not well understood (Zhang et al., 2004). The vertical structure of the SMC is similar to the Hadley circulation, but its return flow is located at the top of the boundary layer. The current theory of the SMC is entirely different dynamically than the Hadley circulation because it has been thought of as a large-scale "sea-breeze" circulation rather a geostrophic balance in the meridional momentum equation. The SMC is a vital aspect of the general circulation since it can transport more moisture than the traditional deep Hadley circulation. Climate models often misrepresent the SMC, making many model simulations incomplete (Zhang et al. 2004; Nolan et al. 2007). We aim to better understand the dynamics near the Intertropical Convergence Zone (ITCZ) that involve both deep and shallow circulations using a steady-state linearized model on the equatorial  $\beta$ -plane that is solved analytically.

The model is forced by prescribed diabatic heating and boundary layer wind stress curl. The circulations that arise from deep diabatic heating profiles suggest that both

the Hadley and Walker circulations are always present, with the Hadley circulation being more prevalent as the deep heating is elongated in the zonal direction, similar to the ITCZ in the East Pacific. The Hadley circulation strengthens because the horizontal surface convergence increases in the meridional direction. Also, the zonal and meridional surface wind anomalies enhance as the deep heating is displaced farther from the equator. The surface wind field associated with this deep heating also forces a significant wind stress curl north of the equator. The atmosphere responds to the wind stress curl by opposing the initial dynamical fields, and generating Ekman pumping in the boundary layer. For example, the surface consists of anomalous negative vorticity in a region that previously contained positively vorticity. This is often referred to as spin down. The Ekman pumping in the boundary layer forces shallow circulations when the frictional forcing is zonally-elongated and sufficiently displaced off of the equator. This shallow circulation makes sense in the East Pacific, where the ITCZ is always north of the equator and is often zonally-elongated. There are two SMCs that develop, one north of the Ekman pumping, and the other to its south. The cross-equatorial SMC is shallower and is stretched in the meridional direction compared to the SMC north of the Ekman pumping since the Rossby length is very large near the equator.

It turns out that the frictional forcing does not provide enough vertical or meridional motion to be seen when deep diabatic heating is also present using our simple model. Since the ITCZ is a transient phenomenon and the frictional forcing is more steady, there are days where this Ekman pumping can be seen when deep convection is suppressed. Future research should concentrate on better understanding the effect of the wind stress and surface temperatures on the buildup of subsequent convection using idealized models.

## ACKNOWLEDGEMENTS

My sincerest gratitude goes out to my advisor, Professor Wayne H. Schubert. His patience, intelligence, and love for science is more than inspiring. I have been humbled by this entire experience, but most especially his knowledge, and his approach to solving problems. He takes any concept that he is trying to gain insight into, and makes it seem logical, and easy to comprehend. I don't know how he does it!

I also would like to acknowledge the Significant Opportunities in Atmospheric Science and Research (SOARS) internship program. If I did not have the opportunity to do research in their program, I may not be conducting research at CSU. I began doing research with Professor Schubert in 2007, as a summer protege in SOARS. Let's just say I became very engulfed in our research, and began to thrive being a part of the Schubert research group. I applied to CSU for grad school, and the rest is history.

I must thank a number of other people, but first Matt Masarik, for his M.S. research was basically my bible! I used his computer model and his advice to help guide my computer model. I also want to thank all of the people I have and have been collaborating with at NCAR, especially Dr. Clara Deser, Dr. Bob Tomas, and Dr. Brian E. Mapes. Their guidance and friendships have been vital to my growth as a scientist.

The other people who also deserve acknowledgment are Dr. Levi G. Silvers, Paul Cieslieski, Brain McNoldy, Rick Taft, Marcus Walter, James Ruppert, Walter Hannah, and Kate Musgrave. They have all helped me and given me encouragement somewhere along the road. I also thank my family because their love and support has been essential to keeping

me confident during stressful times.

The friends that I have made at CSU also deserve to be mentioned. I am truly blessed to have met such a great group of people who not only inspire me to push myself academically, but remind me to enjoy Colorado and life. Gracias guys!

This research was supported by the Center for Multiscale Modeling of Atmospheric Processes (CMMAP) at Colorado State University under Cooperative Agreement No. ATM-0425247 and the NSF Award No. 0837932.

## DEDICATION

*This is dedicated to my mother, father, Melisa, Yary, grandparents, and last but certainly not least Caesar, the Bichon Frise! None of this would be possible without their love and support.*

## TABLE OF CONTENTS

<b>1 Introduction</b>	<b>1</b>
1.1 Relevance of Idealized Models . . . . .	1
1.2 Atmospheric Equatorial Waves . . . . .	2
1.3 Mean Meridional Circulations . . . . .	4
1.4 Discovery of the Shallow Meridional Circulation . . . . .	6
1.5 Current Theory of Shallow Circulations . . . . .	17
1.6 The Tropical East Pacific Ocean . . . . .	20
<b>2 Methods - Stratified Model of Three-Dimensional Tropical Circulations</b>	<b>25</b>
2.1 Linearized Primitive Equations on the Equatorial $\beta$ -plane . . . . .	25
2.2 Vertical Normal Mode Transform . . . . .	27
2.3 Zonal Fourier Transform . . . . .	34
2.4 Meridional Hermite Transform . . . . .	35
2.5 Final Solution of the Prognostic Fields . . . . .	40
<b>3 Methods - Experiment Layout and Model Forcings</b>	<b>42</b>
3.1 Deep Heating Profile . . . . .	42
3.2 Shallow Non-Precipitating Heating Profile . . . . .	44
3.3 Planetary Boundary Layer Frictional Profile . . . . .	46
3.4 Accuracy of Forcings in Spectral Space . . . . .	50
<b>4 Results</b>	<b>58</b>
4.1 The Annual March of the Intertropical Convergence Zone . . . . .	58
4.2 The Deep Hadley and Walker Circulations . . . . .	66
4.3 Surface Wind Stress and Ekman Layer Dynamics . . . . .	74
4.4 Shallow Circulations Forced by Ekman Pumping . . . . .	80
<b>5 Conclusions</b>	<b>87</b>
<b>Appendix</b>	
<b>A Derivation from the Original Primitive Equations in Cartesian Coordinates</b>	<b>93</b>
<b>B Vertical Mode Transform for Case 3 when <math>z_T = z_{\text{crit}}</math></b>	<b>96</b>

<b>C Skew-Hermitian Property of <math>\mathcal{L}</math> for the Equatorial <math>\beta</math>-Plane</b>	<b>98</b>
<b>Bibliography</b>	<b>104</b>

## FIGURES

1.1	The dispersion diagram for all wave types - Rossby waves (blue), Kelvin waves (red), inertia-gravity waves (green), and mixed Rossby-gravity waves (black). The Lamb's parameter is used here, $\epsilon = 4\Omega^2 a^2 / c^2 = 500$ . . . . .	3
1.2	The steady-state SMC produced in Schneider and Lindzen (1977) driven by surface temperature gradients. The streamfunction is contoured with a contour interval of $10^{13} \text{g s}^{-1}$ . . . . .	7
1.3	The vertical structure functions of the mass weighted divergent velocity field from (left) NCEP and (right) ECMWF reanalyses seasonal mean fields for 1979-1993 for the first two EOFs of Trenberth et al. (2000). The units of the vectors are $\text{kg m}^{-1} \text{s}^{-1}$ . . . . .	7
1.4	A vertical-meridional cross section schematic illustrating the Hadley cell (dashed lines) and the recently observed SMC (solid). From Zhang et al. (2004). . . . .	8
1.5	vertical-meridional cross sections of the meridional winds (vector) and relative humidity (shaded) from TAO soundings: (a) time mean at $95^\circ$ and $110^\circ\text{W}$ from August-December 1995-2002; (b) November 2-11 2000 at $95^\circ\text{W}$ . From Zhang et al. (2004). . . . .	9
1.6	A vertical-meridional cross section of the (a) perturbation pressure and (b) horizontal pressure gradient force computed from the analytical sea-breeze model. The contour interval in (a) is 0.25 hPa, and is $10^{-4} \text{m s}^{-2}$ in (b). From Nolan et al. (2007). . . . .	11
1.7	A vertical-meridional cross section schematic illustrating the four main layers of the mean meridional circulation: LLI, SRF, MLI, and ULO. From Nolan et al. (2007). . . . .	12
1.8	Vertical profiles of the mean meridional water transport (water and condensate) at three different latitudes: $4^\circ\text{N}$ , $6^\circ\text{N}$ , and $8^\circ\text{N}$ for (a) time-zonal mean, (b) strong SRF composite, and (c) weak SRF composite. From Nolan et al. (2007). . . . .	13
1.9	A vertical-meridional cross section schematic illustrating the two types of SMCs: (a) marine ITCZ type SMC and (b) monsoon type SMC. From Zhang et al. (2008). . . . .	15

1.10	The annual march (repeated once for clarity) of the vertical structure of the meridional wind field for the East Pacific Ocean (left) and Wes Africa (right) in three global reanalyses: (a) 40-yr European Centre for Medium-Range Weather Forecasts (ECMWF) Re-Analysis (ERA40), (b) the National Centers for Environmental Prediction-National Center for Atmospheric Research (NCEP-NCAR) reanalysis 1 (NCEP1), and (c) NCEP-Department of Energy (DOE) Atmospheric Model Intercomparison Project (AMIP II) reanalysis (NCEP2). The contour interval is $1 \text{ m s}^{-1}$ . From Zhang et al. (2008). . . . .	16
1.11	Mean winds and SSTs in the tropical East Pacific during September 2000-2007. This data was recorded using Quikscat data. From Mora (2008). . . .	17
1.12	Global Scatterometer Climatology of Ocean Winds (SCOW) and (bottom) NCEP99 wind stress curl maps for (left) January and (right) July. The wavelike variations that appear throughout the NCEP99 fields are artifacts of spectral truncation of mountain topography in the spherical harmonic NCEP-NCAR reanalysis model (Milliff and Morzel, 2001). From Risien and Chelton (2008). . . . .	19
1.13	Line contours of $r\psi$ forced solely by Ekman pumping. The sense of the circulation is clockwise. The four panels are created for $z_B = 1 \text{ km}$ , $z_T = 5\pi \text{ km}$ , $\alpha = 0.0465 \text{ k m}^{-1}$ , $w_0 = 3.75 \text{ m s}^{-1}$ , and $\Gamma = 256, 64, 16, 4$ . Colored contours indicate the vertical pressure velocity $\omega$ . Warm colors are upward, cool colors are downward, and the contour interval is $20 \text{ hPa hr}^{-1}$ . From Schubert and McNoldy (2010). . . . .	21
2.1	$\mathcal{Z}_\ell(z)$ for $\ell = 0, 1, 2, 3, 4$ . These functions were computed using (2.33) and (2.42). . . . .	33
2.2	$\mathcal{H}_n(\hat{y}_\ell)$ for $\ell = 1$ ( $\epsilon_1 = 323.42$ , equivalent depth = $272.23 \text{ m}$ ) and $n = 0, 1, 2, 3, 4$ over the equatorial band ( $35^\circ\text{S}, 35^\circ\text{N}$ ). These satisfy the orthonormality condition (2.63). Note that $\hat{y}_\ell$ gets larger as $\ell$ increases. . . . .	39
3.1	The vertical structure of the normalized prescribed deep heating profile, $Z(z)$ , (left) and the deep heating observed in Yanai et al. (1973), $Q_1(z)$ , (right). The maximum heating for both profiles is in the mid-troposphere and the tropopause is around 100-200 hPa. Note that $Q_R$ stays relatively constant with height. . . . .	43
3.2	The horizontal structure $Q_0X(x)Y(y)$ used in the prescribed deep and shallow heating profiles. The constants are $Q_0 = 7.5 \text{ K day}^{-1}$ , $a_0 = 2500 \text{ km}$ , $b = 500 \text{ km}$ , and $y_d = 1000 \text{ km}$ . The contour interval is $0.01 \text{ J kg}^{-1}\text{s}^{-1}$ . . .	45
3.3	The vertical structure of the prescribed shallow heating profile, $Z(z)$ , (left) and the deep heating observed in Nitta and Esbensen (1974), $Q_1$ , (right). The maximum heating for both profiles is within the first 100 hPa of the surface and the trade inversion is in the vicinity of 150-400 hPa above the surface. Note that the vertical axis in the figure on the left is $p$ and the right figure is $p^* = p_s - p$ , where $p_s$ is the surface pressure and that $Q_R$ stays relatively constant with height. . . . .	45

3.4	The normalized vertical structure $Z(z)$ used in the prescribed BL frictional profiles, where $p_B = 800$ hPa. . . . .	47
3.5	Mean winds and divergence in the tropical East Pacific during September 2000-2007. This data was recorded using Quikscat data. From Mora (2008).	48
3.6	The horizontal structure of the prescribed wind stress curl of $F$ , where $a_0 = 2500$ km, $b = 500$ km, $y_d = 1000$ km, $p_B = 800$ hPa, $F_0 = -6.5 \times 10^{-5}$ m s <sup>-2</sup> , and $\rho = 1.2$ kg m <sup>-3</sup> . The contour interval is 1 N m <sup>-2</sup> per 10 <sup>4</sup> km. . . .	49
3.7	The vertical structure of the zonal wind stress $\tau_x(z)$ used for the BL frictional forcing $F$ . The constants used are $p_B = 800$ hPa, $F_0 = -6.5 \times 10^{-5}$ m s <sup>-2</sup> , and $\rho = 1.2$ kg m <sup>-3</sup> . . . . .	50
3.8	The zonal structure of all of the forcings before taking the Fourier transform (black) and after taking the Fourier transform (red). The percent error (or difference) between the zonal structure before and after taking the Fourier transforms (blue). . . . .	51
3.9	The meridional structure of the deep and shallow heating forcings before taking the Hermite transform (black) and after taking the Hermite transform (red). The percent error (or difference) between the meridional structure before and after taking the Hermite transforms (blue). . . . .	52
3.10	The meridional structure of the frictional forcings before taking the Hermite transform (black) and after taking the Hermite transform (red). The percent error (or difference) between the meridional structure before and after taking the Hermite transforms (blue). Note that $y_d = 1000$ km in both plots. . . .	53
3.11	The vertical structure of the deep heating forcing before taking the normal mode transform (black) and after taking the normal mode transform (red). The percent error (or difference) between the vertical structure of the frictional forcings before and after taking the normal mode transforms (blue). . .	55
3.12	The vertical structure of the shallow heating forcing before taking the normal mode transform (black) and after taking the normal mode transform (red). The percent error (or difference) between the vertical structure of the shallow heating forcing before and after taking the normal mode transforms (blue). . .	56
3.13	The vertical structure of the frictional forcings before taking the normal mode transform (black) and after taking the normal mode transform (red). The percent error between the vertical structure of the frictional forcings before and after taking the normal mode transforms (blue). . . . .	57
4.1	The annual march of the ITCZ over the tropical atmosphere (25°S, 25°N). The vales represent the number of days per month the given grid point was “covered” by deep convection (subjectively determined) using 17 years of monthly highly reflective cloud (HRC) data. From Waliser and Gautier (1993).	59

4.2	The steady-state horizontal structure forced by a deep heating profile on the $p = 1010$ hPa pressure level of the geopotential height anomaly field (m) and the wind anomaly field ( $\text{m s}^{-1}$ ) with the same zonal half-width $a_0 = 1250$ km and different meridional displacements: $y_d = \pm 500, 500, 1000,$ and $1500$ km in (a)–(d). The geopotential height field is shaded and contoured at an interval of 2 m. The solid contours represent positive values while the dashed contours represent negative values. The zero contour line is in bold. The maximum magnitude of the geopotential height is 15.457 m. The wind field is illustrated using vectors, with a maximum wind speed of $6.747 \text{ m s}^{-1}$ (used as a reference vector). . . . .	61
4.3	The steady-state horizontal structure forced by a deep heating profile on the $p = 1010$ hPa pressure level of the geopotential height anomaly field (m) and the wind anomaly field ( $\text{m s}^{-1}$ ) with the same zonal half-width $a_0 = 1250$ km, but different meridional displacements ( $y_d = \pm 500$ km - top, $y_d = 0$ km - bottom), and different diabatic heating rates ( $Q_0 = 3.75 \text{ K day}^{-1}$ - top, $Q_0 = 7.5 \text{ K day}^{-1}$ - bottom). The geopotential height field is shaded and contoured at an interval of 0.5 m. The solid contours represent positive values while the dashed contours represent negative values. The zero contour line is in bold. The maximum magnitude of the geopotential height anomaly is 3.585 m. . . . .	62
4.4	The magnitude of the difference in steady-state horizontal structure on the $p = 1010$ hPa pressure level of the zonal wind anomaly field ( $\text{m s}^{-1}$ ) with the same zonal half-width $a_0 = 1250$ km between different meridional displacements: Fig. 4.2c - Fig. 4.2b, Fig. 4.2d - Fig. 4.2c, and Fig. 4.2d - Fig. 4.2a (top to bottom). The zonal wind anomaly field difference is shaded and contoured at an interval of $1 \text{ m s}^{-1}$ . The maximum difference in zonal wind is $7.368 \text{ m s}^{-1}$ . . . . .	64
4.5	The magnitude of the difference in steady-state horizontal structure on the $p = 1010$ hPa pressure level of the meridional wind field ( $\text{m s}^{-1}$ ) with the same zonal half-width $a_0 = 1250$ km between different meridional displacements: Fig. 4.2c - Fig. 4.2b, Fig. 4.2d - Fig. 4.2c, and Fig. 4.2d - Fig. 4.2a (top to bottom). The meridional wind field difference is shaded and contoured at an interval of $0.5 \text{ m s}^{-1}$ . The maximum difference in meridional wind is $3.798 \text{ m s}^{-1}$ . . . . .	65
4.6	The steady-state vertical-meridional structure forced by deep diabatic heating at $x_s = -778$ km in (a), $x_s = +778$ km in (b), and $x_s = 0$ km in (c) of the vertical-pressure velocity field ( $\text{hPa day}^{-1}$ ) and the wind field with the same zonal half-width $a_0 = 1250$ km and meridional displacement $y_d = 1000$ km. The vertical-pressure velocity field is shaded and contoured with the same contour specifications as Fig. 4.2, at an interval of $20 \text{ hPa day}^{-1}$ . The maximum magnitude of the vertical-pressure velocity is $97.632 \text{ hPa day}^{-1}$ . Note that in order to draw vectors of the meridional velocity anomalies and the vertical-pressure velocity we have kept the meridional velocity in $\text{m s}^{-1}$ and converted the vertical-pressure velocity into $\text{Pa s}^{-1}$ , multiplying by 10. Therefore the wind vector units are meaningless. . . . .	67

4.7	The steady-state vertical-zonal structure forced by deep diabatic heating at $y_s = 600$ in (a), $y_s = 1400$ km in (b,) and $y_s = 1000$ km in (c) of the vertical-pressure velocity field ( $\text{hPa day}^{-1}$ ) and the wind field with the same zonal half-width $a_0 = 1250$ km and meridional displacement $y_d = 1000$ km. The vertical-pressure velocity field is shaded and contoured with the same contour specifications as Fig. 4.6. The maximum magnitude of the vertical-pressure velocity is $97.632 \text{ hPa day}^{-1}$ . The same procedure applied in Fig. 4.6 is used for calculating wind vector magnitudes. . . . .	68
4.8	The steady-state vertical-meridional structure forced by a deep heating profile at $x_s = 0$ km of the vertical-pressure velocity field ( $\text{hPa day}^{-1}$ ) and the wind field with the same zonal half-width $a_0 = 1250$ km at different meridional displacements: $y_d = \pm 500, 500, 1000,$ and $1500$ km in (a)–(d). The vertical-pressure velocity field is shaded and contoured with the same contour specifications as Fig. 4.6. The maximum magnitude of the vertical-pressure velocity is $97.402 \text{ hPa day}^{-1}$ . The same procedure applied in Fig. 4.6 is used for calculating wind vector magnitudes. . . . .	70
4.9	The steady-state vertical-meridional structure at $x_s = 0$ km of the vertical-pressure velocity field ( $\text{hPa day}^{-1}$ ) and the wind anomaly field at the same meridional displacement $y_d = 1000$ km with different zonal half-widths: $a_0 = 1250, 2500, 5000,$ and $10000$ km in (a)–(d). The vertical-pressure velocity field is shaded and contoured with the same contour specifications as Fig. 4.6. The maximum magnitude of the vertical-pressure velocity is $96.638 \text{ hPa day}^{-1}$ . The same procedure applied in Fig. 4.6 is used for calculating wind anomaly vector magnitudes. . . . .	71
4.10	The steady-state vertical-zonal structure at $y_s = 1000$ km of the vertical-pressure velocity field ( $\text{hPa day}^{-1}$ ) and the wind anomaly field at the same meridional displacement $y_d = 1000$ km with different zonal half-widths: $a_0 = 1250, 2500, 5000,$ and $10000$ km in (a)–(d). The vertical-pressure velocity field is shaded and contoured with the same contour specifications as Fig. 4.6. The maximum magnitude of the vertical-pressure velocity is $96.638 \text{ hPa day}^{-1}$ . The same procedure applied in Fig. 4.6 is used for calculating wind anomaly vector magnitudes. . . . .	72
4.11	Mean winds and vorticity in the tropical East Pacific during September 2000–2007. This data was recorded using Quikscat data. From Mora (2008). . . .	75
4.12	The steady-state horizontal structure forced by a wind stress curl on the $p = 1010$ hPa pressure level of the geopotential height anomaly field (m) and the wind anomaly field ( $\text{m s}^{-1}$ ) with the same zonal half-width $a_0 = 1250$ km and different meridional displacements: $y_d = 0, 500, 1000,$ and $1500$ km (top to bottom). The geopotential height field is shaded and contoured with the same contour specifications as Fig. 4.2, at an interval of $0.5$ m. The maximum magnitude of the geopotential height anomaly is $4.49$ m. . . . .	78
4.13	The same as Fig. 4.12, with the corresponding contributions by Rossby waves, inertia-gravity waves, mixed Rossby-gravity waves, and Kelvin waves in the bottom four panels. The maximum magnitude of the geopotential height anomaly is $4.54$ m. . . . .	79

- 4.14 The steady-state vertical-meridional structure forced by a wind stress curl when taking a meridional slice at  $x_s = \pm 278$  km in (a) and (b) of the vertical-pressure velocity field ( $\text{hPa day}^{-1}$ ) and the wind field with the same zonal half-width  $a_0 = 1250$  km and meridional displacement  $y_d = 1100$  km (c). The vertical-pressure velocity field is shaded and contoured with the same contour specifications as Fig. 4.6, at an interval of  $0.5 \text{ hPa day}^{-1}$ . The maximum magnitude of the vertical-pressure velocity is  $3.731 \text{ hPa day}^{-1}$ . The same procedure applied in Fig. 4.6 is used for calculating wind vector magnitudes. . . . . 81
- 4.15 The steady-state vertical-meridional structure forced by a wind stress curl when taking a meridional slice at  $x_s = -278, -333, -388,$  and  $-444$  km of the vertical-pressure velocity field ( $\text{hPa day}^{-1}$ ) at the same meridional displacement:  $y_d = 1500$  km, and the wind field with the different zonal half-widths  $a_0 = 1250, 2500, 5000,$  and  $10000$  km in (a)–(d). The vertical-pressure velocity field is shaded and contoured with the same contour specifications as Fig. 4.2, at an interval of  $1 \text{ hPa day}^{-1}$ . The maximum magnitude of the vertical-pressure velocity is  $7.788 \text{ hPa day}^{-1}$ . The same procedure applied in Fig. 4.6 is used for calculating wind vector magnitudes. . . . . 83
- 4.16 The steady-state vertical-meridional structure forced by a wind stress curl when taking a meridional slice at  $x_s = \pm 1779$  km of the vertical-pressure velocity field ( $\text{hPa day}^{-1}$ ) and the wind field with the same zonal half-width  $a_0 = 10000$  km at  $y_d = \pm 500$  km. The vertical-pressure velocity field is shaded and contoured with the same contour specifications as Fig. 4.2, at an interval of  $0.5 \text{ hPa day}^{-1}$ . The maximum magnitude of the vertical-pressure velocity is  $4.998 \text{ hPa day}^{-1}$ . The same procedure applied in Fig. 4.6 is used for calculating wind vector magnitudes. . . . . 86

## TABLES

2.1	External and the first ten internal gravity wave speeds computed using iterative methods for (2.28) and (2.39). . . . .	32
3.1	Numerical values of variables used in the experiments. . . . .	57
3.2	Numerical values for constants introduced in Chapter 2. . . . .	57

## Chapter 1

### INTRODUCTION

#### 1.1 Relevance of Idealized Models

There is no doubt that the importance of improving the accuracy of future climate change simulations continues to increase due to the decision-making of many industries. Making strides in modeling the Earth's climate system is a huge challenge since it involves chaotic processes that arise from sets of equations that even the world's fastest computers have a difficulty processing. As computers become more efficient, climate models will include more complex processes. It will be nearly impossible to completely understand the results from these complex models without improving our understanding of physical processes in idealized scenarios (Held, 2005). We aim to improve understanding of one specific area of study, large-scale atmospheric circulations in the tropics.

Large-scale tropical circulations are vital to climate because they transport mass, heat, energy, momentum, and moisture within the tropics and between the tropics and the subtropics, helping to drive the general circulation of the atmosphere. One of the main reasons why tropical circulations are not well understood is due to the lack of observational data in the tropics (Zagar, 2004). Therefore, many studies use reanalysis products, data assimilation techniques, and an array of models with different levels of complexity, including General Circulation Models (GCMs), to study phenomena in the tropics. When simpler methods are used we must also consider reasonable approximations. The first approximation to the primitive equations (PEs) used in many tropical models is the equatorial  $\beta$ -plane approximation. The next approximation involves linearizing the equations about a basic

resting state, which seems to be a large assumption, but past studies suggest that nonlinear process are not of first-order importance for large-scale tropical circulations (Gill and Philips 1986; Raupp and Silva Dias 2006). Also, without linearizing the equations, one would not be able to solve them analytically. Being able to solve the equations analytically is quite convenient because numerical complications are reduced and solutions of multiple experiments with varying forcings may be superimposed in order to illustrate their combined effects. The linearized analytical model solutions in this study are made up of multiple experiments with different forcings, involving a superposition of atmospheric equatorial waves.

## 1.2 Atmospheric Equatorial Waves

Atmospheric equatorial waves are characterized by oscillations in a number of atmospheric variables (e.g., winds, pressure, temperature). Atmospheric waves can be either free waves or forced waves. A free wave is one for which there is no forcing present (e.g., a thermal forcing), whereas a forced wave can only persist when there is a forcing present. The main atmospheric forcing in the tropics is diabatic heating produced by latent heat release. Latent heat release occurs as a result of the sun heating the upper ocean and evaporating water in the lower atmosphere, which condenses into liquid in convective clouds. This convection can have many forms; it can be described as having a bimodal structure, shallow or deep in the vertical. Associated with heating in the vertical plane are atmospheric waves. Waves in the atmosphere are anisotropic, i.e., their response is not the same in all directions, producing different types of wave structures. There are four types of equatorially trapped waves: Kelvin waves, inertia-gravity waves, Rossby waves, and mixed Rossby-gravity waves (Fig. 1.1). The first scientific papers to present comprehensive mathematical solutions for all equatorial waves were Matsuno (1966) and Blandford (1966).

Matsuno (1966) derived and solved the linearized shallow-water equations of motion on the equatorial  $\beta$ -plane, often referred to as the PEs model since it does not filter any of

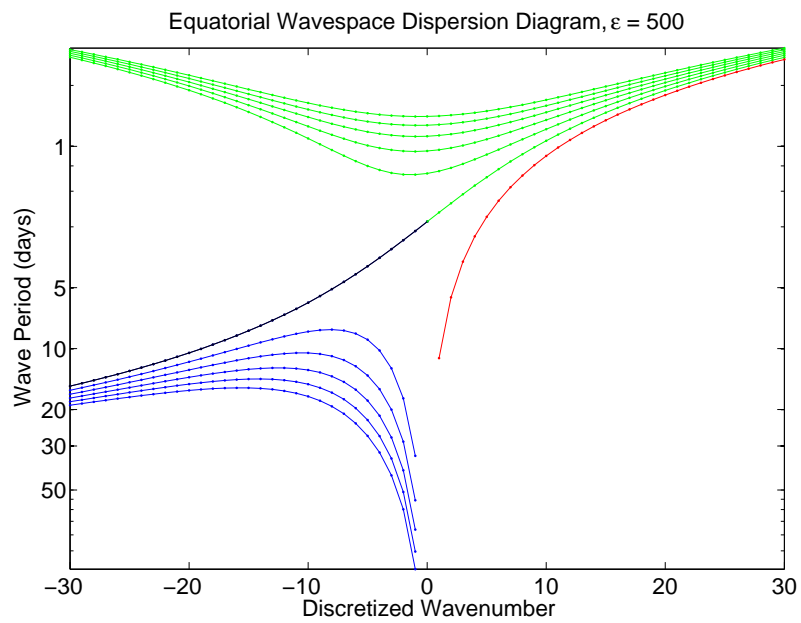


Figure 1.1: The dispersion diagram for all wave types - Rossby waves (blue), Kelvin waves (red), inertia-gravity waves (green), and mixed Rossby-gravity waves (black). The Lamb's parameter is used here,  $\epsilon = 4\Omega^2 a^2 / c^2 = 500$ .

the equatorial waves. The shallow-water approximation assumes that the depth of the fluid in each layer is much smaller than the horizontal length, which is quite appropriate for the Earth. The equatorial  $\beta$ -plane approximation assumes that the Coriolis parameter varies linearly with latitude, which is sufficiently accurate near the equator. Matsuno's solution illustrated free and forced equatorial waves in physical space and in spectral space. The spectral space solutions are displayed in terms of what is often called a dispersion diagram, illustrated in Fig. 1.1. Matsuno's dispersion diagram illustrates the characteristics of waves in terms of wave frequency and zonal wavenumber. From the dispersion diagram, one can calculate many important variables, including wave phase speed and group velocity.

After Matsuno (1966) many other studies, such as Webster (1972) and Gill (1980), used the linearized shallow-water equations on the equatorial  $\beta$ -plane to study atmospheric circulations in the tropics. These models and other simple models demonstrated that simple linearized models can accurately explain the essential dynamics of many types of large-scale tropical circulations. A few examples of these large-scale circulations include monsoon circulations, the deep Walker circulation (DWC), the El Niño Southern Oscillation (ENSO), the Madden-Julian Oscillation (MJO), the Quasi Biennial Oscillation (QBO), and mean meridional circulations (MMCs).

### 1.3 Mean Meridional Circulations

MMCs play a major role in the general circulation of the Earth's climate system. Their role is to transport mass, momentum, moisture and energy between the tropics and subtropics. In the Intertropical Convergence Zone (ITCZ) there is low-level wind convergence with rising air from the surface to the tropical tropopause that is transported poleward, sinking in the subtropics. This overturning circulation is often referred to as the deep Hadley circulation (DHC), and is usually associated with deep convection near the equator. The DHC is vital to the general circulation of the atmosphere because it transports mass, momentum, and energy between the tropics and the subtropics.

One of the simplest models of the DHC solves the zonally-symmetric PEs forced by deep diabatic heating in the ITCZ. The hydrostatic approximation can be made, as well as geostrophic balance of the zonal flow. This zonal flow balance is between the meridional pressure gradient force and the Coriolis force in the meridional momentum equation. The form of this balance on the equatorial  $\beta$ -plane is as follows:

$$\beta y u = -\frac{\partial \phi}{\partial y}, \quad (1.1)$$

where  $\beta = 2\Omega/a$  is the variation of the Coriolis parameter,  $\Omega$  the angular velocity of the Earth,  $a$  the radius of the Earth,  $y$  the meridional position,  $u$  the zonal wind, and  $\phi$  the geopotential. Note that the acceleration of the meridional momentum,  $v$ , following the flow,  $Dv/Dt$  has been neglected even though  $v \neq 0$ . One can combine (1.1) and the hydrostatic equation with a result of the thermal wind equation:

$$\beta y \frac{\partial u}{\partial z} = -\frac{g}{T_0} \frac{\partial T}{\partial y}, \quad (1.2)$$

where  $z = H \ln(p_0/p)$  is the vertical log-pressure coordinate,  $H = RT_0/g$  the constant scale height, and  $p_0$  and  $T_0$  denote the constant reference pressure and temperature,  $g$  is the acceleration of gravity, and  $T$  the temperature. The thermal wind relation (1.2) is vital to understanding the atmospheric general circulation because it implies that the zonal wind becomes more westerly with height where the temperature field decreases with latitude. This means not only does these set of equations help explain the DHC, they also suggest that zonal jet streams exist where meridional temperature gradients are large (i.e., between the tropics and subtropics), due to some diabatic forcing. The main diabatic forcing of this simplified model is deep heating simulating the main properties of deep convection in the ITCZ.

Even though deep convection dominates over other vertical profiles of convection in the ITCZ, there has been increasing interest in shallow convection, and its transition to deep convection since it is also common in and around the ITCZ region. The recent discovery of a shallower MMC, called the Shallow Meridional Circulation (SMC) (Zhang et al., 2004)

is helping bring more attention to this topic. The current theory of the dynamics in the SMC is quite different than the traditional DHC, therefore it has not been referred to a the shallow Hadley circulation. We will discuss the observations and proposed theory behind the dynamics of the SMC in the next two sections.

#### 1.4 Discovery of the Shallow Meridional Circulation

The SMC was discovered in modeling studies long before it was first observed. These modeling studies focused on gaining insight into the DHC, and did not have a comprehensive explanation of why the SMC was produced. One of the first studies to produce a SMC was Schneider and Lindzen (1977).

They examined steady-state solutions of the linearized, hydrostatic, PEs on the sphere with a variety of forcings - diabatic heating, frictional forcings, and surface temperature gradients. Their goal was to produce a deep MMC comparable to the observed DHC using a variety of forcings. They were able to produce the DHC with diabatic heating and cumulus friction forcings. With only surface temperature gradients as a forcing, they were also able to produce a shallower overturning circulation below 800 hPa. They explain that the circulation is confined to a surface layer due to their assumed vertical variation of small-scale vertical mixing (Fig. 1.2). They also mention that the SMC could lead to upper level heating by cumulus convection. Since there were no observations of such a shallow MMC at the time, the implications of the SMC were not discussed in much detail.

Another study that produced a SMC before it was first observed is Trenberth et al. (2000). They performed an Empirical Orthogonal Function (EOF) analysis on the divergent part of the tropical wind field in two global model analysis products, in which EOFs determine the leading modes of variability of the data. The first EOF mode represents deep circulations, such as the DHC and the DWC. The second EOF mode represents shallower circulations confined near the surface (Fig. 1.3). This result was found in many tropical regions, such as the East Pacific Ocean, West Africa, the Atlantic Ocean, and over the

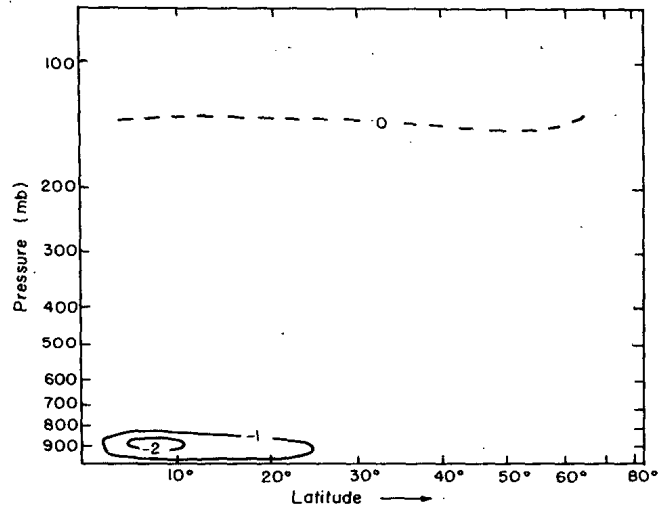


Figure 1.2: The steady-state SMC produced in Schneider and Lindzen (1977) driven by surface temperature gradients. The streamfunction is contoured with a contour interval of  $10^{13} \text{g s}^{-1}$ .

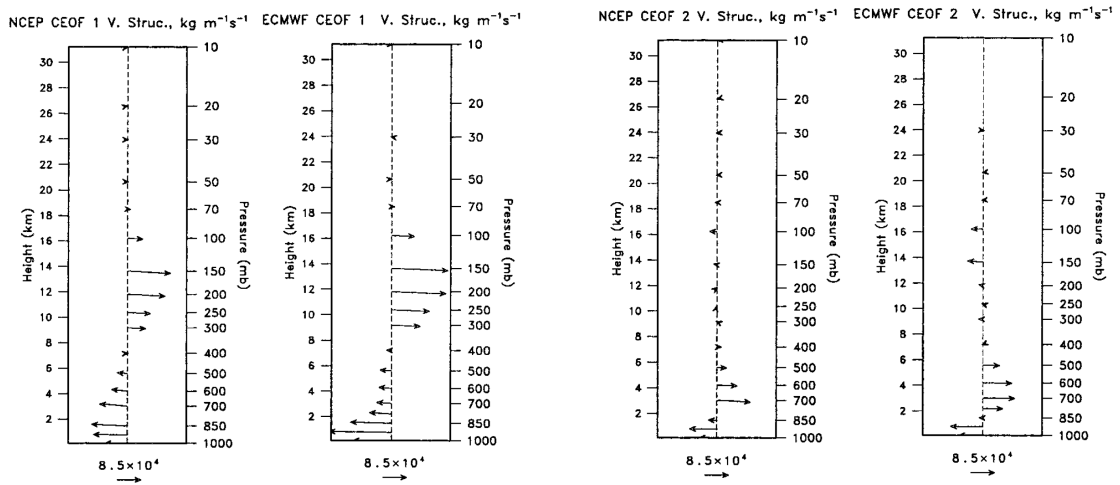


Figure 1.3: The vertical structure functions of the mass weighted divergent velocity field from (left) NCEP and (right) ECMWF reanalyses seasonal mean fields for 1979-1993 for the first two EOFs of Trenberth et al. (2000). The units of the vectors are  $\text{kg m}^{-1} \text{s}^{-1}$ .

Americas. They questioned the result for the second EOF, stating that a shallow tropical circulation has yet to be observed.

It was not until recently that the SMC was seen in observations - in the tropical East Pacific Ocean (Zhang et al., 2004). Zhang et al.(2004) used four independent datasets: the Tropical Atmosphere-Ocean (TAO) ship sounding dataset, the East Pacific Investigation of Climate Processes (EPIC2001) dropsonde dataset, the First Global Atmospheric Research Program (GARP) Global Experiment (FGGE) dropsonde dataset, and the dataset from wind profilers at Christmas Island and San Cristóbal, Galápagos. These datasets illustrate vertical-meridional cross sections of the meridional wind field for individual days, as well as time-averaged meridional wind fields with an emphasis from late boreal summer until early boreal winter. They define the SMC as an overturning circulation consisting of cross equatorial low-level inflow (LLI) at the surface from  $10^{\circ}\text{S}$  until  $10^{\circ}\text{N}$ , where the air rises in the ITCZ, but only reaches the top of the atmospheric boundary layer (BL). Therefore a northerly shallow return flow (SRF) crosses the equator and completes its circulation by sinking around  $10^{\circ}\text{S}$  (Zhang et al., 2004) (Fig. 1.4).

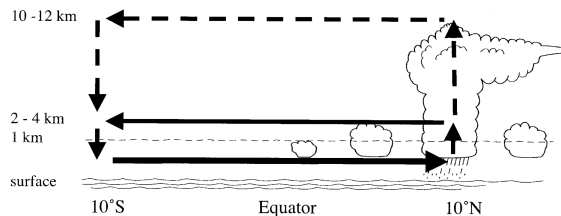


Figure 1.4: A vertical-meridional cross section schematic illustrating the Hadley cell (dashed lines) and the recently observed SMC (solid). From Zhang et al. (2004).

They suggest that the depth of MMCs may be related directly to the depth of convection in the ITCZ, where the DHC is associated with deep convection and the SMC is associated with shallow convection. The time-mean meridional flow shows that the LLI is most dominant when the SRF and ULO are significantly weaker (Fig. 1.5). An interesting feature is the existence of mid-level winds below the ULO, referred to as the mid-level inflow (MLI). They illustrate that the SRF and ULO vary quite a bit on a day-to-day basis, but

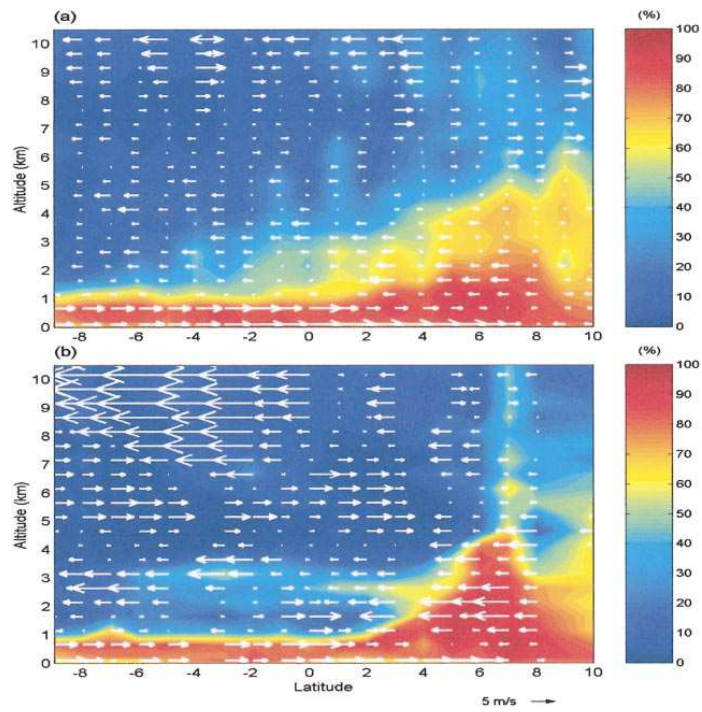


Figure 1.5: vertical-meridional cross sections of the meridional winds (vector) and relative humidity (shaded) from TAO soundings: (a) time mean at  $95^\circ$  and  $110^\circ\text{W}$  from August-December 1995-2002; (b) November 2-11 2000 at  $95^\circ\text{W}$ . From Zhang et al. (2004).

that they can also coexist. This implies that shallow convection and stratified heating may be present at the same time as well. Since global model simulations tend to misrepresent shallow convection, it makes sense that the SRF is being misrepresented.

Nolan et al. (2007) examined the SMC using two simplified models to theorize on the existence of the SMC in the tropical East Pacific Ocean, and to analyze its moisture budget. The first model is an analytical single-hemispheric model where temperature and pressure have a simple logarithmic relationship and there are larger lapse rates in the BL. The theory posed is as follows: in the ITCZ there is enhanced low-level convergence and there are relatively warm surface temperatures, therefore generally low surface pressure. Outside of the ITCZ region temperatures are cooler and surface pressures are higher, further enhancing the low-level convergence in the ITCZ. The warmer air in the atmospheric BL of the ITCZ allows for the thickness between pressure levels to be larger, and the BL to be deeper. Since the BL in the ITCZ is deeper, the pressure gradient reverses near the top of the BL, leading to meridional flow away from the ITCZ. Therefore, the theory deems the SMC as a large-scale sea-breeze-type circulation (Fig. 1.6). The flow balance in this theory of the SMC is fundamentally different than the balance in the DHC. The meridional momentum equation is a balance between the meridional pressure gradient force and the acceleration of the meridional momentum following the flow instead of a balance between the meridional pressure gradient force and the Coriolis force,

$$\frac{Dv}{Dt} = -\frac{\partial\phi}{\partial y}, \quad (1.3)$$

where all variables have the same definitions defined previously. If this theory holds, then the observed SMC cannot be directly related to convection, or in other words be called a shallow Hadley circulation.

The other model is a single-hemispheric version of the Weather Research and Forecasting (WRF) model. It is a three dimensional, compressible atmospheric model that includes a longwave radiation scheme (Rapid Radiative Transfer Model), but no shortwave radiation scheme. For microphysics the WRF single-moment (WSM) five-class microphysics

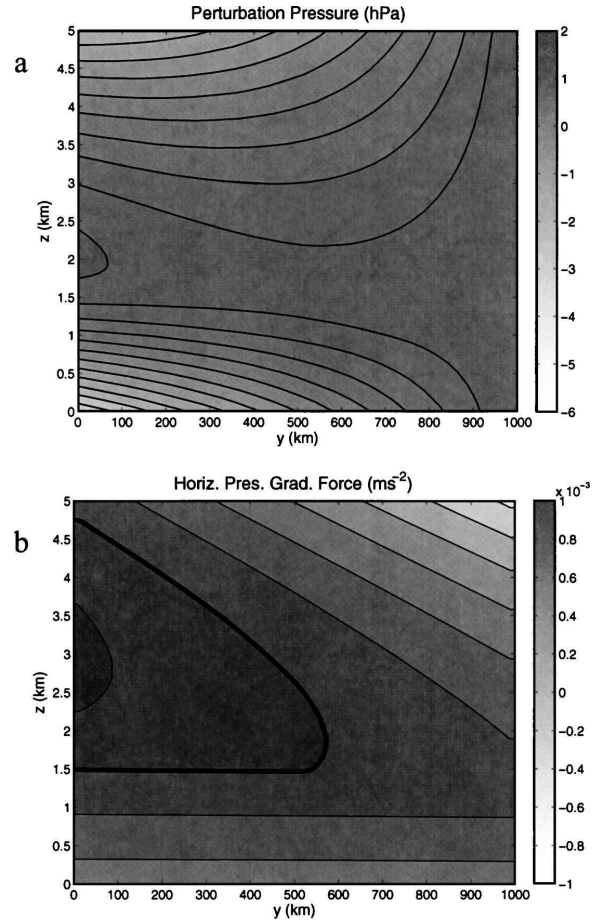


Figure 1.6: A vertical-meridional cross section of the (a) perturbation pressure and (b) horizontal pressure gradient force computed from the analytical sea-breeze model. The contour interval in (a) is 0.25 hPa, and is  $10^{-4} \text{ m s}^{-2}$  in (b). From Nolan et al. (2007) .

scheme was used. The schemes used for the planetary BL were the Yonsei University (YSU) scheme and the Mellor-Yamada-Janjic (MYJ) scheme. Cumulus convection was parameterized using either the Kain-Fritsch scheme or the Grell ensemble scheme. The initial state consists of a mean tropical sounding that contains a large sea surface temperature (SST) gradient. After taking the time and zonal mean the SMC produced from these simulations is quite similar to the one observed in the East Pacific Ocean in Zhang et al. (2004) and the structure of the pressure field compares well with the analytical sea-breeze model. These simulations show four main components/layers of the vertical-meridional cross section: the LLI, the SRF, the MLI, and upper level outflow (ULO) (Fig. 1.7).

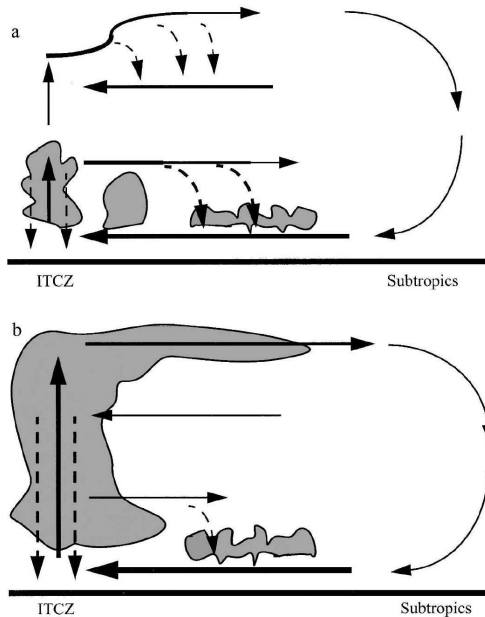


Figure 1.7: A vertical-meridional cross section schematic illustrating the four main layers of the mean meridional circulation: LLI, SRF, MLI, and ULO. From Nolan et al. (2007).

The implications of the SMC are substantial - air lofted in the ITCZ in the SMC has significantly more moisture than air lofted in the DHC; therefore they look closely at the moisture transport. They produce time and zonal mean vertical moisture profiles of cases that have a strong SRF, a weak SRF, and the overall time and zonal mean at three different latitudes:  $4^{\circ}\text{N}$ ,  $6^{\circ}\text{N}$ , and  $8^{\circ}\text{N}$  (Fig. 1.8). In general, the water vapor content of parcels is

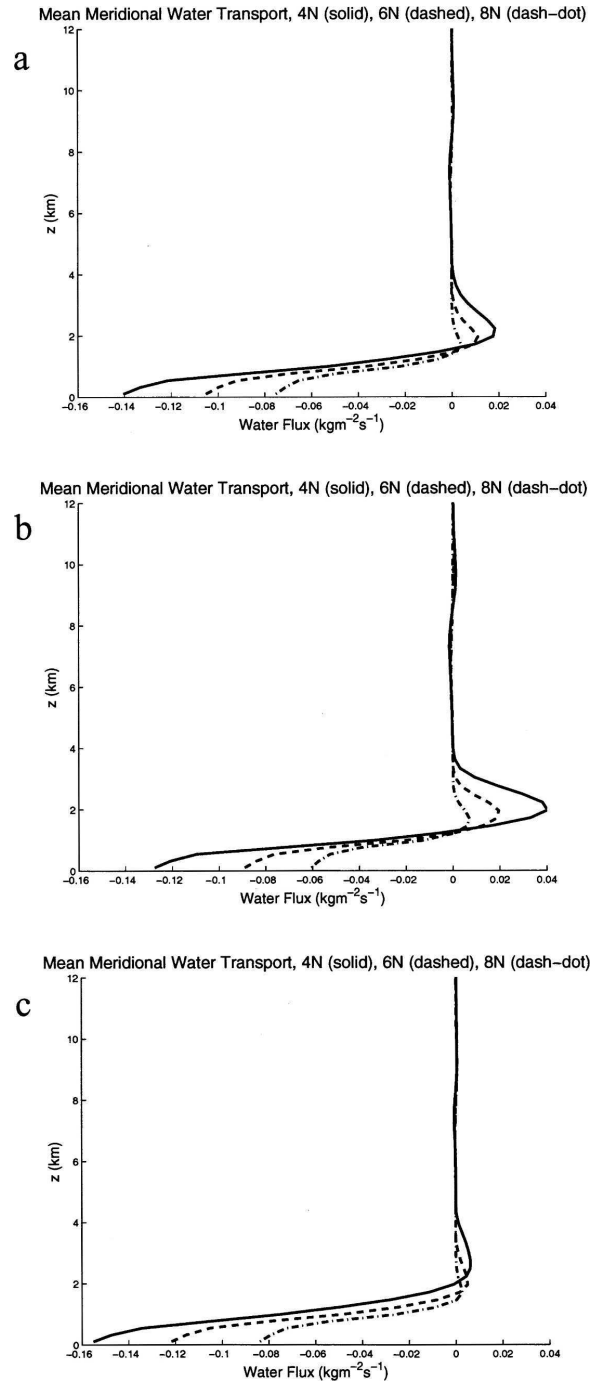


Figure 1.8: Vertical profiles of the mean meridional water transport (water and condensate) at three different latitudes: 4°N, 6°N, and 8°N for (a) time-zonal mean, (b) strong SRF composite, and (c) weak SRF composite. From Nolan et al. (2007).

largest in the BL, with the MLI and ULO having negligible moisture content. The BL inflow decreases in cases where the SRF is strong, while MLI and ULO remain about the same. The amount of moisture advection in the LLI is balanced by moisture transport in the SRF, where it is the largest, and by precipitation by clouds. The strength of this weak moisture source to the ITCZ is comparable to the magnitude of the moisture sink of the outflow in the upper troposphere of the DHC. As the SRF intensifies, the water content transported out of the ITCZ increases. For a more in-depth analysis of the vertical-meridional moisture budget of the ITCZ, refer to Nolan et al. (2010).

A follow up study to Nolan et al. (2007) was published just a year later, by Zhang et al. (2008), where more extensive global reanalysis products producing the SMC were examined (the 40-yr European Centre for Medium-Range Weather Forecasts (ECMWF) Re-Analysis (ERA-40), the National Centers for Environmental Prediction-National Center for Atmospheric Research (NCEP-NCAR) reanalysis 1, and the NCEP-Department of Energy (DOE) Atmospheric Model Intercomparison Project (AMIP II) reanalysis). They used these reanalyses over all of the tropical ocean basins and over some tropical land surfaces. The most prevalent SMCs being over the tropical East Pacific Ocean and West Africa. They note that SMCs have a seasonal cycle, can be located on either side of the ITCZ, and all have distinct structures. The SMC over the tropical east Pacific Ocean is defined as a marine ITCZ type of SMC, while the SMC over West Africa is defined as a monsoon type of SMC (Fig. 1.9).

The marine ITCZ type of SMC is essentially the same as the one described in Zhang et al. (2004) and Nolan et al. (2007). The monsoon type of SMC involves southerly surface flow on either side of the ITCZ with rising motion in the ITCZ and over the heated land surface, or heat low that develops before and during the West African monsoon. At the top of the BL the SRF is northerly, and there is sinking motion south of the equator and north of the heat low. The SMC aids in providing moisture to the relatively dry region just north of the ITCZ over West Africa. This additional moisture allows for the development of deep

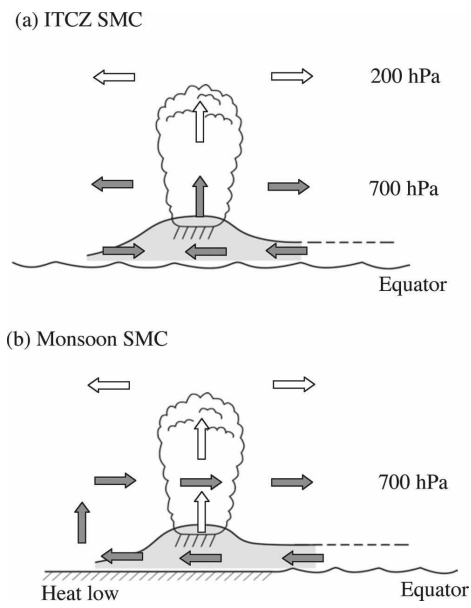


Figure 1.9: A vertical-meridional cross section schematic illustrating the two types of SMCs: (a) marine ITCZ type SMC and (b) monsoon type SMC. From Zhang et al. (2008).

convection from shallow convection (Zhang et al., 2006). The SMC and DHC tend to not be present simultaneously in the time-zonal mean over West Africa, unlike the SMC over the East Pacific Ocean (Fig. 1.10). The SMC over the tropical East Pacific Ocean does not

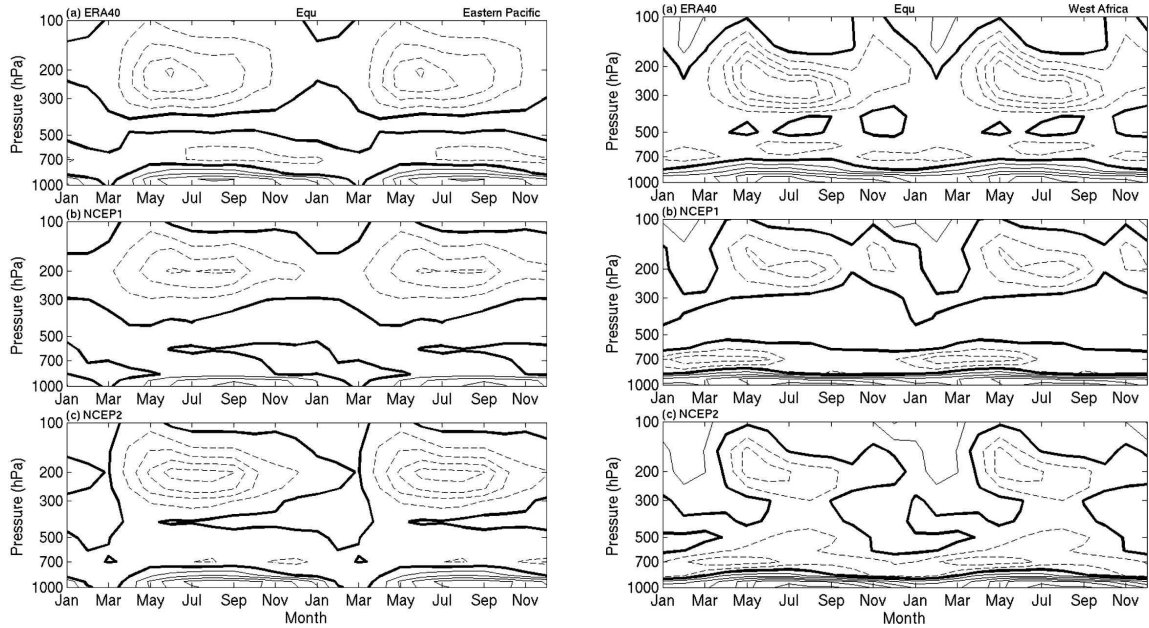


Figure 1.10: The annual march (repeated once for clarity) of the vertical structure of the meridional wind field for the East Pacific Ocean (left) and West Africa (right) in three global reanalyses: (a) 40-yr European Centre for Medium-Range Weather Forecasts (ECMWF) Re-Analysis (ERA40), (b) the National Centers for Environmental Prediction-National Center for Atmospheric Research (NCEP-NCAR) reanalysis 1 (NCEP1), and (c) NCEP-Department of Energy (DOE) Atmospheric Model Intercomparison Project (AMIP II) reanalysis (NCEP2). The contour interval is  $1 \text{ m s}^{-1}$ . From Zhang et al. (2008).

provide as much moisture north of the ITCZ; therefore there is no monsoon that develops after the SMC peaks in strength. The SMC over the tropical East Pacific Ocean is strongest in late boreal summer until early boreal winter when ITCZ is farthest north of the equator (Waliser and Gautier, 1993), with the SRF located around 700-800 hPa. The SMC over West Africa is strongest in boreal winter and spring, and West Africa is relatively deep in the vertical, with its SRF located around 650-750 hPa. It is interesting to note that this is a similar level as the African easterly jet.

## 1.5 Current Theory of Shallow Circulations

The lack of observations in the tropics is part of the reason why shallow MMCs have taken so long to recognize, as well as the lack of theories to why they should occur. A few theories have been proposed by Nolan et al. (2007) and Schubert and McNoldy (2010). Nolan et al. (2007) argue the SMC exists due to strong variations in SSTs in the meridional direction, as discussed in the previous section. The majority of the tropics are observed to have small horizontal temperature gradients, so there are a few regions with relatively large meridional SST gradients. The tropical East Pacific Ocean tends to exhibit a feature that enhances meridional SST gradients known as the cold tongue, which is strongest from July-November, and is weakest during boreal spring (Fig. 1.11).

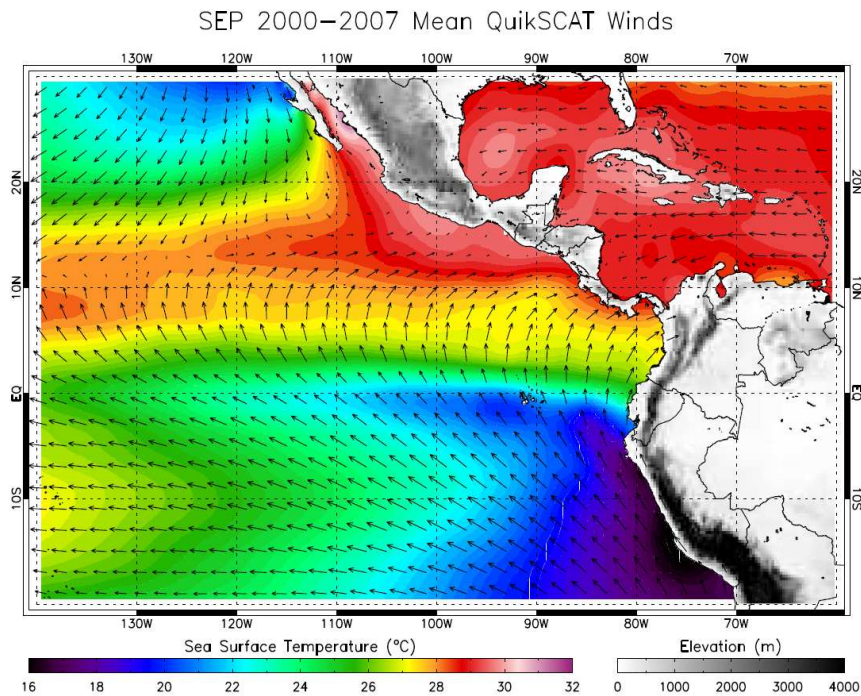


Figure 1.11: Mean winds and SSTs in the tropical East Pacific during September 2000-2007. This data was recorded using Quikscat data. From Mora (2008).

The SMC in this region is observed to peak in strength from late boreal summer until early boreal winter, agreeing well with the Nolan et al. (2007) theory. The cold tongue is due

to ocean upwelling the forms west of South America along the equator as the thermocline in the ocean becomes shallower and may be further enhanced when colder water along the coast of South America is brought equatorward with the easterly trades.

Another theory on shallow MMCs involves the inherently large Rossby length and small Rossby depth in the tropics in the absence of tropical cyclones. In the ITCZ of the tropical East Pacific Ocean and the East Atlantic Ocean there is significantly large Ekman pumping out of the BL. This vertical motion is implied due to the significant zonally-elongated bands of the wind stress curl in the ITCZ of these regions (Fig. 1.12). Since the inertial stability near the equator is small, the Rossby length will be relatively large and the Rossby depth will be relatively small. The Rossby length in Schubert and McNoldy (2010) is defined as

$$L_\ell = \left( \frac{A}{C} \right)^{1/2} \frac{z_T}{\ell\pi}, \quad (1.4)$$

where  $A$  is the static stability,  $C$  the inertial stability,  $z_T$  the height of the top of the troposphere, and  $\ell$  the vertical wavenumber. Parcels in the ITCZ tend to rise to the top of the BL, where they diverge horizontally, producing a shallower MMC. The only way parcels may rise to the top of the troposphere and complete a deep MMC is when there is either small static stability, such as in deep convection, or large inertial stability, such as during a tropical cyclone.

Schubert and McNoldy (2010) demonstrated the importance of these concepts of Rossby length, Rossby depth, and Ekman layer dynamics in relation to hurricane strength. They produced idealized analytical solutions of the transverse circulation equation that arises in the balanced vortex model of tropical cyclones. They solved the transverse circulation three ways:

- (i) performing a vertical transform requiring that a radial structure equation is solved;
- (ii) performing a radial transform requiring that a vertical structure equation is solved;
- (iii) solving the elliptic PDE directly, without regard to boundary conditions, and then enforcing the lower boundary condition using the method of image circulations.

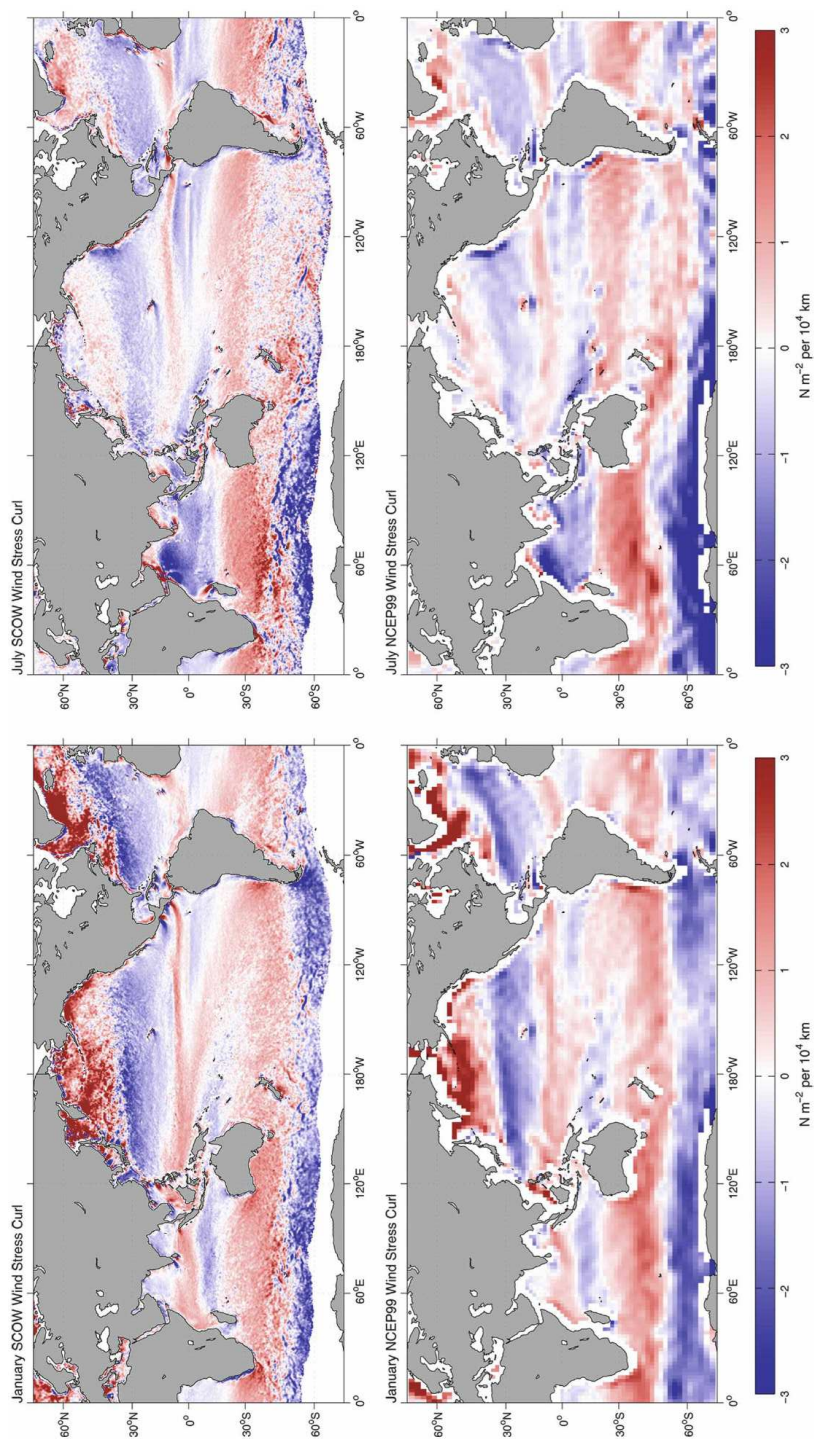


Figure 1.12: Global Scatterometer Climatology of Ocean Winds (SCOW) and (bottom) NCEP99 wind stress curl maps for (left) January and (right) July. The wavelike variations that appear throughout the NCEP99 fields are artifacts of spectral truncation of mountain topography in the spherical harmonic NCEP-NCAR reanalysis model (Milliff and Morzel, 2001). From Risien and Chelton (2008).

The first method allows the concept of Rossby lengths to be introduced while the second method allows the concept of Rossby depth to be introduced. For strong vortices, Rossby lengths are small and Rossby depths are large, therefore the secondary circulation is more vertically elongated and horizontally compressed. For weak vortices, Rossby lengths are large and Rossby depths are small, therefore the secondary circulation is more horizontally-elongated and vertically compressed (Fig. 1.13). These same concepts can be generalized to the zonally-symmetric tropical atmosphere, especially in regions where there is large-scale positive wind stress curl, such as the tropical East Pacific Ocean.

## 1.6 The Tropical East Pacific Ocean

The tropical East Pacific has some unique characteristics in that the magnitude of the curl of the wind stress at the surface is enhanced over zonal-elongated bands in the ITCZ (Risien and Chelton, 2008), the ITCZ stays north of the equator during almost all months of the year (Waliser and Gautier, 1993), and there are relatively large SST gradients. The ITCZ in the tropical East Pacific Ocean can also exhibit features of a double ITCZ (DITCZ) during some years - one just north of the equator and another just south of the equator. This occurs when the cold tongue weakens and narrows, in boreal spring and when El Niño is weak. The ITCZ north of the equator generally has more deep convective clouds than the ITCZ south of the equator, since the warmest SSTs are slightly north of the ITCZ north of the equator (Wallace et al., 1989). The cold tongue reaches its peak intensity in August-September in the East Pacific Ocean warming up until March. These unique characteristics in and around the East Pacific ITCZ will be investigated in more detail using our simplified model in this study.

The theory we look to explore more involves the concepts of Rossby length and Rossby depth. Parcels have the ability to rise to the tropopause in the ITCZ when the atmosphere has a deep heating profile. Without a deep heating forcing, parcels cannot penetrate deep above the BL; parcels will instead diverge in the horizontal. The main reason for this is

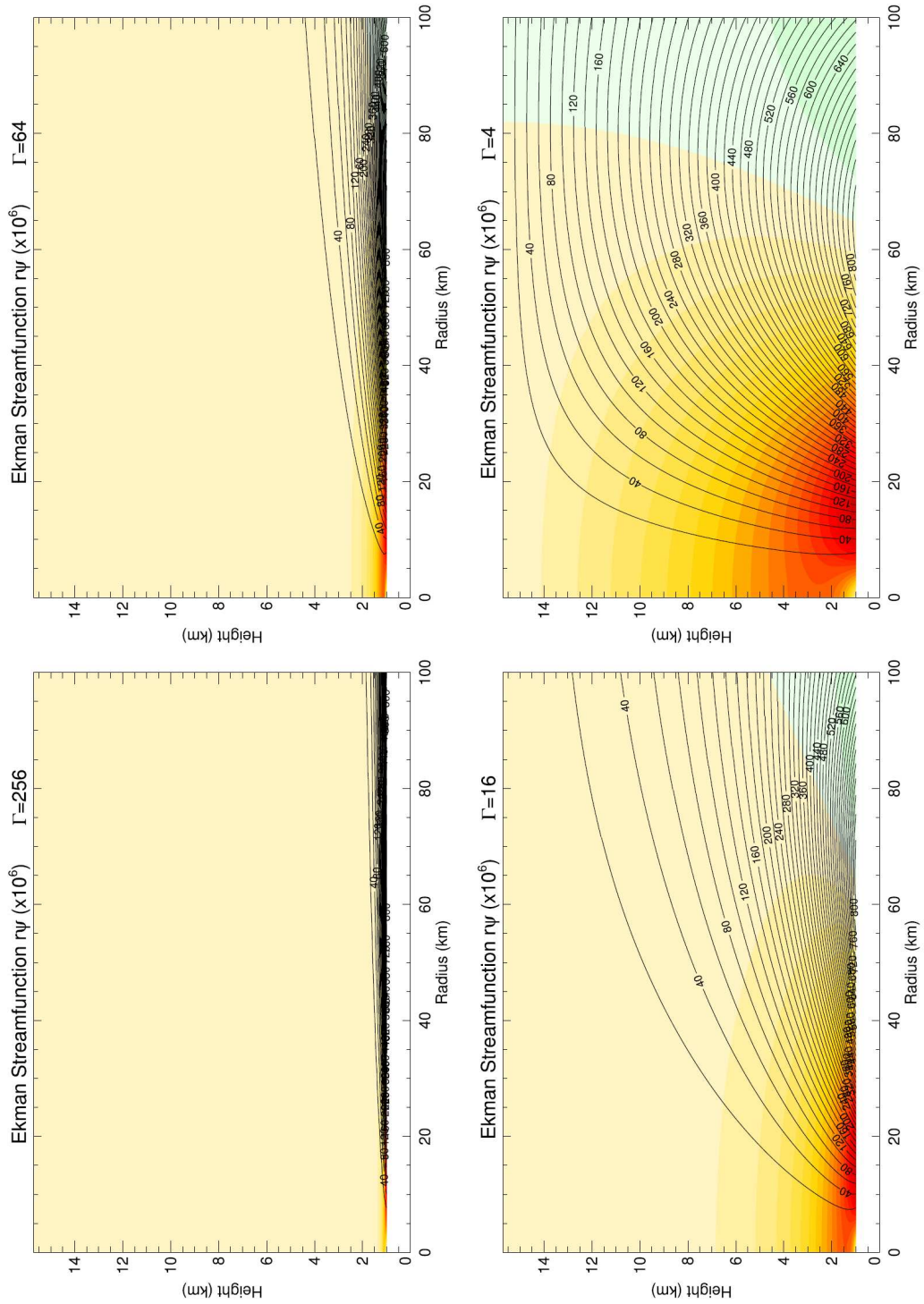


Figure 1.13: Line contours of  $r\psi$  forced solely by Ekman pumping. The sense of the circulation is clockwise. The four panels are created for  $z_B = 1$  km,  $z_T = 5\pi$  km,  $\alpha = 0.0465$   $\text{k m}^{-1}$ ,  $w_0 = 3.75$   $\text{m s}^{-1}$ , and  $\Gamma = 256, 64, 16, 4$ . Colored contours indicate the vertical pressure velocity  $\omega$ . Warm colors are upward, cool colors are downward, and the contour interval is 20  $\text{hPa hr}^{-1}$ . From Schubert and McNoldy (2010).

that the Rossby length in the tropics is always large and the Rossby depth is always small, and Ekman pumping is constantly occurring in the ITCZ. The tropics have small inertial stability, requiring the Rossby length of parcels to be large and the Rossby depth to be small. Therefore, a SMC should be present throughout the all ITCZs in the tropical atmosphere, especially where deep heating is not dominant. Regions where shallower heating profiles exist due to cooler SSTs, such as the East Pacific Ocean, may be more susceptible to the SMC simply because vertical heating profiles are shallower. This would possibly support the notion that the SMC is more like a shallow Hadley circulation than a sea-breeze type circulation.

It is quite possible that both the theory on surface temperature gradients and the theory of Rossby length both help in enhancing the SMC over the East Pacific Ocean and West Africa; in fact they may be very closely related. The strong SST gradients and large Ekman pumping definitely do exist in the SMC regions, and have seasonality, just like the SMC.

These unique features of tropical ocean basins such as the East Pacific have led to a number of simplified modeling studies delving into the relationships between surface winds, SSTs, and vertical motion related to deep convection (e.g., Lindzen and Nigam 1987, Back and Bretherton 2009).

Lindzen and Nigam (1987) devised a simple steady-state one-layer model on the sphere, where they concentrate on the trade cumulus boundary layer (below 700 hPa). The surface temperature field is given, and acts to drive low-level pressure gradients. These pressure gradients, along with a cumulonimbus mass flux, act to enhance horizontal wind convergence near the surface in order to reduce pressure gradients. Overall, they show that low-level winds over the tropical oceans are largely determined by SST distribution.

Back and Bretherton (2009) attempts to generalize the work of Lindzen and Nigam (1987) by using a linear mixed layer model (Stevens et al., 2002) that examines not only the influence of boundary layer processes, but also free-tropospheric processes on the surface

winds in the tropics. They modify their model’s cumulus boundary layer to be shallower (850 hPa), to include both the zonally asymmetric part and the symmetric part (not included in Lindzen and Nigam (1987)), and to a set of equations where surface convergence is not a consequence of deep convection to first-order. They find some interesting results:

- (1) Zonal surface winds are determined by free-tropospheric pressure gradients and downward momentum mixing;
- (2) Horizontal wind convergence is due to boundary layer temperature gradients (including SSTs);
- (3) SST gradients more likely to cause deep convection rather than SSTs being a cause of deep convection.

Overall, we see that SSTs, winds, and convection are related, but getting into causalities is not easy using analytical models.

We will not delve into causalities in this study; we simply aim to study large-scale shallow and deep circulations in and around the East Pacific ITCZ. Therefore we have formulated an analytical linear equatorial  $\beta$ -plane model that includes stratification and prescribed frictional and heat sources. The frictional sources are prescribed to have a large wind stress curl, to show the effects of Ekman pumping in the BL. The heat sources are prescribed to simulate characteristics of either shallow non-precipitating or deep heating profiles. Other heating profiles are discussed as future work.

The paper is organized in the following manner. In Chapter 2, we introduce the stratified model and perform a series of spectral transforms in the three spatial directions in order to solve the equations analytically. Chapter 3 discusses the specific forms of the frictional forcings and heat sources that drive the model solutions. We also give the values for constants and varying parameters, and provide the necessary framework for our experiments. Chapter 4 illustrates the model solutions for relevant experiments and elaborates on their significance to understanding large-scale flows in the ITCZ. Chapter 5 concludes the study by reviewing the model formulation, the current understanding of shallow and

deep circulations in the ITCZ before this paper, and the insight gained by carrying out the various experiments. The last section also explores what future work can be done in order to better understand both shallow and deep circulations.

## Chapter 2

# METHODS - STRATIFIED MODEL OF THREE-DIMENSIONAL TROPICAL CIRCULATIONS

### 2.1 Linearized Primitive Equations on the Equatorial $\beta$ -plane

The diabatically-forced linearized primitive equations on the equatorial  $\beta$ -plane can help describe many aspects in the tropical atmosphere and ocean, e.g., the deep Walker circulation (DWC), El Niño Southern Oscillation (ENSO), the Madden-Julian Oscillation (MJO), and mean meridional circulations (MMCs). The goal of this chapter is to study MMCs in the tropical atmosphere that arise from shallow and deep diabatic heating profiles, as well as planetary boundary layer (BL) frictional forcings. More specifically, we would like to determine which forcings most prominently drive the Shallow Meridional Circulation (SMC). Deriving solutions of the linearized primitive equations involves solving a cubic equation for the equatorial wave frequencies. We superpose the spectral space wave frequencies and use inverse mathematical transforms to compute solutions for anomalies of the physical space winds, geopotential height, and temperature fields.

Consider small amplitude motions about a resting basic state (e.g.,  $\bar{u}, \bar{v} = 0$ ) in a stratified, compressible, quasi-static atmosphere on the equatorial  $\beta$ -plane. For the vertical coordinate we use  $z = H \ln(p_0/p)$ , where  $H = RT_0/g$  is the constant scale height, and  $p_0$  and  $T_0$  denote the constant reference pressure and temperature. We can write the forced linearized primitive equations as

$$\frac{\partial u}{\partial t} - \beta y v + \frac{\partial \phi}{\partial x} = F - \alpha u, \quad (2.1)$$

$$\frac{\partial v}{\partial t} + \beta y u + \frac{\partial \phi}{\partial y} = G - \alpha v, \quad (2.2)$$

$$\frac{\partial \phi}{\partial z} = \frac{g}{T_0} T, \quad (2.3)$$

$$\frac{\partial u}{\partial x} + \frac{\partial v}{\partial y} + \frac{\partial w}{\partial z} - \frac{w}{H} = 0, \quad (2.4)$$

$$\frac{\partial T}{\partial t} + \frac{T_0 N^2}{g} w = \frac{Q}{c_p} - \alpha T, \quad (2.5)$$

where  $x$  is the zonal position,  $y$  the meridional position,  $t$  time,  $u$  the zonal wind anomaly,  $v$  the meridional wind anomaly,  $w = Dz/Dt$  the perturbation “vertical log-pressure velocity”,  $\phi$  the geopotential anomaly,  $T$  the perturbation temperature,  $F$  the prescribed frictional force per unit mass in the zonal direction,  $G$  the prescribed frictional force per unit mass in the meridional direction, and  $Q$  the prescribed diabatic heat source. The independent variables are  $x, y, z, t$  and the dependent variables are  $u, v, w, \phi, T, Q, F$ , and  $G$ . In order to use the equatorial  $\beta$ -plane approximation, since the approximation is only valid sufficiently close to the equator, we assume that all of the fields  $u, v, w, \phi, T, Q, F, G \rightarrow 0$  as  $y \rightarrow \pm\infty$ . The numerical constants in (2.1)–(2.5) are as follows:  $N^2 = (g/T_0) (d\bar{T}/dz + \kappa\bar{T}/H)$  is the basic state static stability computed from the basic state temperature profile  $\bar{T}(z)$ ,  $\beta = 2\Omega/a$  the variation of the Coriolis parameter,  $f = \beta y$ , with respect to meridional displacement from the equator,  $\Omega$  the angular velocity of the Earth,  $a$  the radius of the Earth,  $\alpha$  the coefficient for Rayleigh friction and Newtonian cooling,  $g$  the acceleration of gravity, and  $c_p$  the specific heat capacity at constant pressure. The numerical values for the constants just mentioned are displayed in Chapter 3. The derivation from the nonlinear primitive equations to (2.1)–(2.5) is shown in Appendix A.

The model that we have just introduced is quite idealized, but for the goals expressed it is more than capable of providing us with valuable insight. The equation set (2.1)–(2.5) is quite similar to Schubert and Masarik (2006), except (2.1)–(2.5) incorporates frictional forcings and allows for more complicated vertical structures. The equatorial  $\beta$ -plane approximation is valid since the SMC has been observed to take place sufficiently close to

the equator ( $-15^\circ\text{S}$ ,  $15^\circ\text{N}$ ). The observed horizontal circulation patterns are  $O(10,000 \text{ km})$ , making the quasi-static approximation also acceptable. The lack of a moisture budget may seem like a very crude assumption, but a prescribed diabatic heat source shall be sufficient for investigating the large-scale dynamical features of the shallow and deep overturning circulations.

## 2.2 Vertical Normal Mode Transform

The first step to solving (2.1)–(2.5) is to separate the vertical structure from the horizontal and temporal structure by computing the vertical transform of (2.1)–(2.5). We assume that the solutions of (2.1)–(2.5) have a separable horizontal, vertical, and temporal structure of the form

$$u(x, y, z, t) = X(x)Y(y)Z(z)T(t). \quad (2.6)$$

Basically, we want to replace any vertical derivatives, which cannot be derived analytically, with derivatives of vertical wavenumber  $\ell$  that can be derived analytically. Since (2.1) and (2.2) do not have any vertical derivatives, we can ignore them for now. First we rewrite (2.4) and eliminate  $T$  from (2.3) and (2.5)

$$\frac{\partial u}{\partial x} + \frac{\partial v}{\partial y} + e^{z/H} \frac{\partial}{\partial z} \left( e^{-z/H} w \right) = 0, \quad (2.7)$$

$$- \left( \frac{\partial}{\partial t} + \alpha \right) \frac{\partial \phi}{\partial z} + N^2 w = \frac{g}{T_0} \frac{Q}{c_p}. \quad (2.8)$$

To solve (2.7) and (2.8) we need to consider appropriate boundary conditions in the vertical direction. We require an upper boundary condition that reflects vertically propagating waves so that the phase speed spectrum of the waves is discrete (Fulton, 1980). We choose the so called, “rigid lid” condition that the vertical log-pressure velocity,  $w$ , vanishes at the top boundary  $z = z_T$ . At the lower boundary  $z = 0$  we require that the actual vertical velocity vanishes, i.e.,  $D\phi/Dt = 0$ . If the Earth’s surface is assumed to be flat, this condition should be applied at Earth’s actual surface and not at  $H \ln(p_0/p) = 0$ ; therefore our lower

boundary condition is approximate since  $H \ln(p_0/p) = 0$  is technically not the Earth's surface. The boundary conditions are

$$w = 0 \quad \text{at } z = z_T, \quad (2.9)$$

$$\frac{D\phi}{Dt} = 0 \quad \text{at } z = 0. \quad (2.10)$$

Eliminating  $w$  from (2.7) and (2.8) yields

$$-\left(\frac{\partial}{\partial t} + \alpha\right) e^{z/H} \frac{\partial}{\partial z} \left( \frac{e^{-z/H} \partial (\phi - \tilde{\phi})}{N^2} \right) + \frac{\partial u}{\partial x} + \frac{\partial v}{\partial y} = 0, \quad (2.11)$$

where

$$\left(\frac{\partial}{\partial t} + \alpha\right) \frac{\partial \tilde{\phi}}{\partial z} = \frac{g}{T_0} \frac{Q}{c_p}. \quad (2.12)$$

Using (2.8) and (2.12) to modify the boundary conditions results in

$$\frac{\partial}{\partial z} \left(\frac{\partial}{\partial t} + \alpha\right) (\phi - \tilde{\phi}) = 0 \quad \text{at } z = z_T, \quad (2.13)$$

$$\left(\frac{\partial}{\partial z} - \frac{N^2}{g}\right) \left(\frac{\partial}{\partial t} + \alpha\right) (\phi - \tilde{\phi}) = 0 \quad \text{at } z = 0. \quad (2.14)$$

Equation (2.11) must be solved using the vertical normal mode transform pair given below

$$\begin{pmatrix} u(x, y, z, t) \\ v(x, y, z, t) \\ \phi(x, y, z, t) \end{pmatrix} = \sum_{\ell=0}^{\infty} \begin{pmatrix} u_{\ell}(x, y, t) \\ v_{\ell}(x, y, t) \\ \phi_{\ell}(x, y, t) \end{pmatrix} \mathcal{Z}_{\ell}(z), \quad (2.15)$$

$$\begin{pmatrix} u_{\ell}(x, y, t) \\ v_{\ell}(x, y, t) \\ \phi_{\ell}(x, y, t) \end{pmatrix} = \int_0^{z_T} \begin{pmatrix} u(x, y, z, t) \\ v(x, y, z, t) \\ \phi(x, y, z, t) \end{pmatrix} \mathcal{Z}_{\ell}(z) e^{-z/H} dz, \quad (2.16)$$

where  $\mathcal{Z}_{\ell}(z) = \mathcal{N}_{\ell} \Psi_{\ell}(z) e^{z/2H}$  are the vertical structure functions,  $\mathcal{N}_{\ell}$  is a normalization constant, and  $\Psi_{\ell}(z)$  is the kernel of the integral transform (2.16), and  $e^{-z/2H}$  is the weight of the integral transform. So far,  $\mathcal{N}_{\ell}$  and  $\Psi_{\ell}(z)$  are yet to be determined, but we will solve for them in the next section. We apply the vertical normal mode integral transform (2.16),

which requires us to multiply (2.11) by  $\mathcal{Z}_\ell(z)e^{-z/H}$  and integrate over the entire vertical plane

$$-\left(\frac{\partial}{\partial t} + \alpha\right) \int_0^{z_T} e^{z/H} \frac{\partial}{\partial z} \left( \frac{e^{-z/H} \partial(\phi - \tilde{\phi})}{N^2} \right) \mathcal{Z}_\ell(z) e^{-z/H} dz + \frac{\partial u_\ell}{\partial x} + \frac{\partial v_\ell}{\partial y} = 0. \quad (2.17)$$

The integral of the first term on the left hand side of (2.17) must be solved by integrating by parts twice

$$\begin{aligned} & \left(\frac{\partial}{\partial t} + \alpha\right) \int_0^{z_T} e^{z/H} \frac{\partial}{\partial z} \left( \frac{e^{-z/H} \partial(\phi - \tilde{\phi})}{N^2} \right) \mathcal{Z}_\ell(z) e^{-z/H} dz \\ &= \left\{ \frac{e^{-z/H}}{N^2} \mathcal{Z}_\ell(z) \frac{\partial}{\partial z} \left[ \left(\frac{\partial}{\partial t} + \alpha\right) (\phi - \tilde{\phi}) - \frac{e^{-z/H}}{N^2} \frac{d\mathcal{Z}_\ell(z)}{dz} \left(\frac{\partial}{\partial t} + \alpha\right) (\phi - \tilde{\phi}) \right] \right\}_0^{z_T} \\ &+ \int_0^{z_T} \left(\frac{\partial}{\partial t} + \alpha\right) (\phi - \tilde{\phi}) \frac{d}{dz} \left[ \frac{e^{-z/H}}{N^2} \frac{d\mathcal{Z}_\ell(z)}{dz} \right] dz. \end{aligned} \quad (2.18)$$

Using (2.13) and (2.14), we can easily show that the boundary term in (2.18) vanishes.

Now we focus our attention on simplifying the integral in (2.18). In order to expand any vertical structure, we need to solve the Sturm-Liouville eigenproblem with the boundary conditions (2.13) and (2.14). We begin with a second order ordinary differential equation (ODE) for the vertical structure  $\mathcal{Z}_\ell(z) = \mathcal{N}_\ell \Psi_\ell(z) e^{z/2H}$

$$e^{z/H} \frac{d}{dz} \left[ \frac{e^{-z/H}}{N^2} \frac{d\mathcal{Z}_\ell}{dz} \right] + \frac{1}{c_\ell^2} \mathcal{Z}_\ell = 0, \quad (2.19)$$

$$\frac{d\mathcal{Z}_\ell}{dz} = 0 \quad \text{at } z = z_T, \quad (2.20)$$

$$\frac{d\mathcal{Z}_\ell}{dz} - \frac{N^2}{g} \mathcal{Z}_\ell = 0 \quad \text{at } z = 0. \quad (2.21)$$

The inverse transform may be obtained by considering the properties of the solutions of (2.19)–(2.21). It can be shown (e.g., Morse and Feshback 1953) that if  $N^2(z)$  is strictly positive and continuously differentiable for  $0 \leq z \leq z_T$  then (2.19)–(2.21) have a countably indefinite set of solutions (eigenvalues and eigenvectors) with the following three properties

(Fulton, 1980):

(i) The eigenvalues  $c_\ell$  are real and may be ordered such that  $c_0 > c_1 > \dots > c_\ell > 0$  with  $c_\ell \rightarrow 0$  as  $\ell \rightarrow \infty$ .

(ii) The eigenfunctions  $\Psi_\ell(z)$  are orthogonal and may be chosen to be real.

(iii) The eigenfunctions  $\Psi_\ell(z)$  form a complete set. We assume that  $N^2$  is constant with respect to  $z$  and therefore we are able to solve the differential equation analytically. We split up the solution into three separate cases.

Case 1 involves evanescent solutions, where (2.19) becomes

$$\left(\frac{d}{dz} - \frac{1}{H}\right) \frac{d\mathcal{Z}_\ell}{dz} + \frac{N^2}{c_\ell^2} \mathcal{Z}_\ell = 0. \quad (2.22)$$

The general solution of this ODE using the characteristic equation is

$$\mathcal{Z}_\ell(z) = [C \cosh(\mu_\ell z) + D \sinh(\mu_\ell z)] e^{z/2H}, \quad (2.23)$$

where  $\mu_\ell^2 \geq 0$ , and

$$\mu_\ell^2 = \frac{1}{4H^2} - \frac{N^2}{c_\ell^2}. \quad (2.24)$$

The boundary conditions become

$$\gamma C + \mu_\ell D = 0 \quad (2.25)$$

at  $z = 0$ , where  $\gamma = 1/2H - N^2/g$ , and

$$C \left( \mu_\ell \tanh(\mu_\ell z_T) + \frac{1}{2H} \right) + D \left( \mu_\ell + \frac{1}{2H} \tanh(\mu_\ell z_T) \right) = 0 \quad (2.26)$$

at  $z = z_T$  when the general solution is substituted. In order for a nontrivial solution to be obtained from this homogeneous linear system of equations one must solve for  $\mu_\ell$  when the determinant of the matrix  $\mathcal{A}$  equals zero, where

$$\mathcal{A} = \begin{pmatrix} \mu_\ell \tanh(\mu_\ell z_T) + \frac{1}{2H} & \mu_\ell + \frac{1}{2H} \tanh(\mu_\ell z_T) \\ \gamma & \mu_\ell \end{pmatrix}. \quad (2.27)$$

There is only one solution when the determinant of  $\mathcal{A}$  equals zero, therefore we set the subscript to  $\ell = 0$ . We shall refer to this mode as the external mode, where

$$\tanh(\mu_0 z_T) - \frac{\mu_0 z_T}{\frac{g}{N^2} \left( \frac{z_T}{4H^2} - \frac{(\mu_0 z_T)^2}{z_T} \right) - \frac{z_T}{2H}} = 0 \quad (2.28)$$

is an equation for  $\mu_0 z_T$  that must be solved using iteration techniques. We choose to use Newton's iteration since the derivative of this equation is sufficiently large. Newton's iterative method uses the equation

$$x_{k+1} = x_k + \frac{f(x_k)}{f'(x_k)}, \quad (2.29)$$

where  $k$  is the iteration number and  $f(x)$  is a function that must equal zero, e.g., (2.28).

The resulting gravity wave speed for the external mode is  $c_0 = 271.2708 \text{ ms}^{-1}$ , shown in Table 2.1. Using the  $z = 0$  boundary condition,  $\gamma C + \mu_0 D = 0$ , and (2.28) we can rewrite (2.23) as

$$\mathcal{Z}_0(z) = C \left[ \cosh(\mu_0 z) - \frac{\gamma}{\mu_0} \sinh(\mu_0 z) \right] e^{z/2H}. \quad (2.30)$$

In order to solve for  $C$ , we must return to properties (ii) and (iii) of our solution. We normalize  $\Psi_0(z)$  so that we use the orthonormality relation

$$\int_0^{z_T} \mathcal{Z}_{\ell'}(z) \mathcal{Z}_\ell(z) e^{-z/H} dz = \begin{cases} 1 & \ell' = \ell, \\ 0 & \ell' \neq \ell. \end{cases} \quad (2.31)$$

We find that the normalization constant,  $C^2$ , is

$$C^2 = \mathcal{N}_0^2 = \frac{2\mu_0^3}{\sinh(\mu_0 z_T) \cosh(\mu_0 z_T) (\mu_0^2 + \gamma^2) + \mu_0 z_T (\mu_0^2 - \gamma^2) - 2\mu_0 \gamma \sinh^2(\mu_0 z_T)}. \quad (2.32)$$

Therefore, our solution is

$$\mathcal{Z}_0(z) = \mathcal{N}_0 \left[ \cosh(\mu_0 z) - \frac{\gamma}{\mu_0} \sinh(\mu_0 z) \right] e^{z/2H}. \quad (2.33)$$

Case 2 involves sinusoidal solutions, where  $\lambda_\ell^2 \geq 0$  and

$$\lambda_\ell^2 = \frac{N^2}{c_\ell^2} - \frac{1}{4H^2}. \quad (2.34)$$

The general solution of (2.22) when incorporating the new variable  $\lambda_\ell$  is

$$\mathcal{Z}_\ell(z) = [E \cos(\lambda_\ell z) + F \sin(\lambda_\ell z)] e^{z/2H}. \quad (2.35)$$

The boundary conditions become

$$\gamma E + \lambda_\ell F = 0 \quad (2.36)$$

at  $z = 0$  and

$$E \left( \frac{1}{2H} - \lambda_\ell \tan(\lambda_\ell z_T) \right) + F \left( \lambda_\ell + \frac{1}{2H} \tan(\lambda_\ell z_T) \right) = 0 \quad (2.37)$$

at  $z = z_T$  when the general solution is substituted. In order for a nontrivial solution to be obtained from this homogeneous linear system of equations one must solve for  $\lambda_\ell$  when the determinant of the matrix  $\mathcal{B}$  equals zero, where

$$\mathcal{B} = \begin{pmatrix} \frac{1}{2H} - \lambda_\ell \tan(\lambda_\ell z_T) & \lambda_\ell + \frac{1}{2H} \tan(\lambda_\ell z_T) \\ \gamma & \lambda_\ell \end{pmatrix}. \quad (2.38)$$

There are infinite solutions ( $\lambda_\ell = \lambda_1, \lambda_2, \dots, \lambda_\infty$ ) when the determinant of  $\mathcal{B}$  equals zero; we shall refer to these modes as the internal modes, where

$$\tan(\lambda_\ell z_T) - \frac{\lambda_\ell z_T}{\frac{g}{N^2} \left( \frac{z_T}{4H^2} + \frac{(\lambda_\ell z_T)^2}{z_T} \right) - \frac{z_T}{2H}} = 0 \quad (2.39)$$

is an equation for  $\lambda_\ell z_T$  that must be solved using iteration techniques. Since the derivative

Table 2.1: External and the first ten internal gravity wave speeds computed using iterative methods for (2.28) and (2.39).

$\ell$	$c_\ell$ [ms <sup>-1</sup> ]
0	271.2708
1	51.6651
2	26.8124
3	18.0068
4	13.5404
5	10.8454
6	9.0439
7	7.7550
8	6.7874
9	6.0343
10	5.4315

of (2.39) is quite small, Newton's iterative method cannot be used. Therefore we use the Bisection method, which converges more slowly than Newton's method, but can be used for almost any function. The first ten internal modes are displayed in Table 2.1. Using the  $z = 0$  boundary condition,  $\gamma E + \lambda_\ell F = 0$ , and (2.28) we can rewrite (2.35) as

$$\mathcal{Z}_\ell(z) = E \left[ \cos(\lambda_\ell z) - \frac{\gamma}{\lambda_\ell} \sin(\lambda_\ell z) \right] e^{z/2H}. \quad (2.40)$$

In order to solve for  $E$ , we must satisfy (2.31), and we solve for the normalization constant,  $E^2$ ,

$$E^2 = \mathcal{N}_\ell^2 = \frac{2\lambda_\ell^3}{\sin(\lambda_\ell z_T) \cos(\lambda_\ell z_T) (\lambda_\ell^2 - \gamma^2) + \lambda_\ell z_T (\lambda_\ell^2 + \gamma^2) - 2\lambda_\ell \gamma \sin^2(\lambda_\ell z_T)}. \quad (2.41)$$

Therefore,

$$\mathcal{Z}_\ell(z) = \mathcal{N}_\ell \left[ \cos(\lambda_\ell z) - \frac{\gamma}{\lambda_\ell} \sin(\lambda_\ell z) \right] e^{z/2H}. \quad (2.42)$$

Case 3 occurs when  $1/4H^2 = N^2/c^2$ , e.g.,  $\lambda = \mu = 0$ , involving linear solutions. This case is only included when  $z_T = z_{\text{crit}}$  and is described in more detail in Appendix B.

The vertical structure functions  $\mathcal{Z}_\ell(z)$  for the external and first four internal modes are plotted in Fig. 2.1. After applying the vertical normal mode transform to the governing

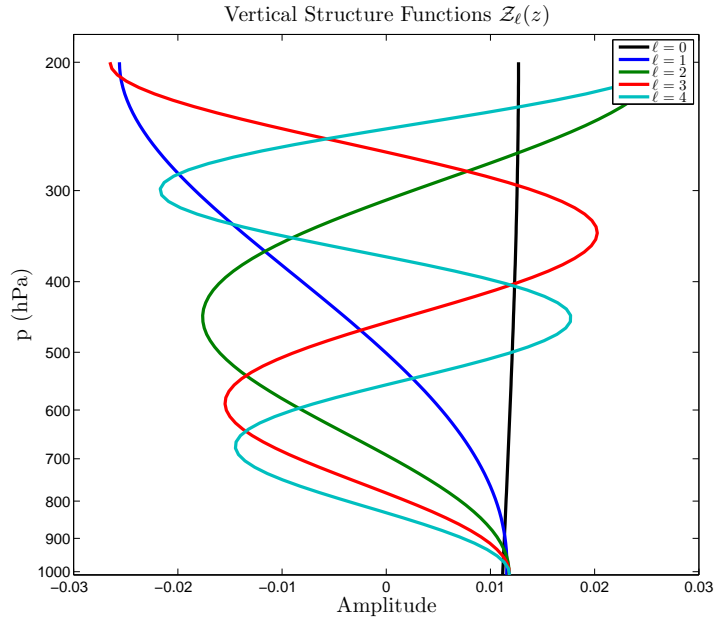


Figure 2.1:  $\mathcal{Z}_\ell(z)$  for  $\ell = 0, 1, 2, 3, 4$ . These functions were computed using (2.33) and (2.42).

equations (2.1), (2.2), and (2.11) we arrive at a set of shallow-water equations (linearized divergent barotropic model) for each vertical wavenumber  $\ell$

$$\left( \frac{\partial}{\partial t} + \alpha \right) u_\ell - \beta y v_\ell + \frac{\partial \phi_\ell}{\partial x} = F_\ell, \quad (2.43)$$

$$\left(\frac{\partial}{\partial t} + \alpha\right)v_\ell + \beta y u_\ell + \frac{\partial \phi_\ell}{\partial y} = G_\ell, \quad (2.44)$$

$$\left(\frac{\partial}{\partial t} + \alpha\right)\phi_\ell + c_\ell^2 \left(\frac{\partial u_\ell}{\partial x} + \frac{\partial v_\ell}{\partial y}\right) = \left(\frac{\partial}{\partial t} + \alpha\right)\tilde{\phi}_\ell. \quad (2.45)$$

### 2.3 Zonal Fourier Transform

Another simplifying procedure of (2.43)–(2.45) is to take the Fourier transform of each equation in the zonal direction. The zonal Fourier transform allows one to decompose our equations into their constituent zonal wavenumbers, converting derivatives with respect to  $x$  into algebraic factors involving the zonal wavenumber. The form of the Fourier transform pair is

$$u_{\ell m}(y, t) = \frac{1}{2\pi a} \int_{-\pi a}^{\pi a} u_\ell(x, y, t) e^{-imx/a} dx, \quad (2.46)$$

$$u_\ell(x, y, t) = \sum_{m=-\infty}^{\infty} u_{\ell m}(y, t) e^{imx/a}, \quad (2.47)$$

where the integer  $m$  denotes the integer zonal wavenumber. Similar Fourier transform pairs exist for  $v_{\ell m}$  and  $\phi_{\ell m}$ . Note that (2.46) and (2.47) incorporate the concept of Earth's periodicity in the zonal direction, which is a more accurate approximation of the Fourier transform than a Fourier transform in an infinite domain, since wavenumbers can only have integer values in the more realistic spherical coordinates. In this way the system of equations (2.43)–(2.45) reduces to

$$\left(\frac{\partial}{\partial t} + \alpha\right)u_{\ell m} - \beta y v_{\ell m} + \frac{im}{a}\phi_{\ell m} = F_{\ell m}, \quad (2.48)$$

$$\left(\frac{\partial}{\partial t} + \alpha\right)v_{\ell m} + \beta y u_{\ell m} + \frac{\partial \phi_{\ell m}}{\partial y} = G_{\ell m}, \quad (2.49)$$

$$\left(\frac{\partial}{\partial t} + \alpha\right)\phi_{\ell m} + c_\ell^2 \left(\frac{im}{a}u_{\ell m} + \frac{\partial v_{\ell m}}{\partial y}\right) = \left(\frac{\partial}{\partial t} + \alpha\right)\tilde{\phi}_{\ell m}. \quad (2.50)$$

## 2.4 Meridional Hermite Transform

We simplify (2.48)–(2.50) even further to arrive at an ordinary differential equation in time by using a normal mode transform in the meridional direction. First, it is most convenient to write (2.48)–(2.50) in a matrix/vector form for reasons discussed below. The matrix/vector form is

$$\left(\frac{\partial}{\partial t} + \alpha\right) \boldsymbol{\eta}_{\ell m} + \mathcal{L}\boldsymbol{\eta}_{\ell m} = \boldsymbol{\mathcal{E}}_{\ell m}, \quad (2.51)$$

where  $\mathcal{L}$  is the matrix operator

$$\mathcal{L} = \begin{pmatrix} 0 & -\beta y & im/a \\ \beta y & 0 & \partial/\partial y \\ c_\ell^2 im/a & c_\ell^2 \partial/\partial y & 0 \end{pmatrix}, \quad (2.52)$$

$\boldsymbol{\eta}_{\ell m}(y, t)$  is a vector that includes the horizontal wind and geopotential fields

$$\boldsymbol{\eta}_{\ell m}(y, t) = \begin{pmatrix} u_{\ell m}(y, t) \\ v_{\ell m}(y, t) \\ \phi_{\ell m}(y, t) \end{pmatrix}, \quad (2.53)$$

and  $\boldsymbol{\mathcal{E}}_{\ell m}(y, t)$  is a vector that represents the forcing fields

$$\boldsymbol{\mathcal{E}}_{\ell m}(y, t) = \begin{pmatrix} F_{\ell m}(y, t) \\ G_{\ell m}(y, t) \\ \left(\frac{\partial}{\partial t} + \alpha\right) \tilde{\phi}_{\ell m}(y, t) \end{pmatrix}. \quad (2.54)$$

The derivation of the meridional normal mode transform involves taking the inner product of (2.51). Therefore, we define the inner product as

$$\langle \mathbf{f}, \mathbf{g} \rangle = \int_{-\infty}^{\infty} (f_1 g_1^* + f_2 g_2^* + \frac{1}{c_\ell^2} f_3 g_3^*) d\hat{y}_\ell, \quad (2.55)$$

where  $\mathbf{f}(\hat{y}_\ell, t)$  and  $\mathbf{g}(\hat{y}_\ell, t)$  are complex three component vector functions of the dimensionless meridional coordinate  $\hat{y}_\ell = (\beta/c_\ell)^{1/2} y = \epsilon_\ell^{1/4} (y/a)$ . The \* symbol in (2.55) denotes the complex conjugate and  $\epsilon_\ell = 4\Omega^2 a^2 / c_\ell^2$  is Lamb's parameter for each vertical wavenumber  $\ell$ . The inner product (2.55) is suggested by the total energy principle associated with (2.51),

explained in more detail in Schubert and Masarik (2006). The adjoint of  $\mathcal{L}$ , denoted by  $\mathcal{L}^\dagger$  and defined by  $(\mathcal{L}\mathbf{f}, \mathbf{g}) = (\mathbf{f}, \mathcal{L}^\dagger\mathbf{g})$ , is related to  $\mathcal{L}$  by  $\mathcal{L}^\dagger = -\mathcal{L}$ . In other words, the linear operator  $\mathcal{L}$  is skew-Hermitian with respect to the inner product (2.55) (discussed in more detail in the Appendix C). The skew-Hermitian property dictates that the eigenvalues of  $\mathcal{L}$  are pure imaginary and that the eigenvalues form a complete (Wu and Moore, 2004), orthogonal set, as long as degeneracy does not occur. Degeneracy occurs when two distinct eigenfunctions (wave types) have the same eigenvalue (frequency). We define an eigenvalue by  $i\nu_{\ell mn r}$  and a corresponding eigenfunction by  $\mathbf{K}_{\ell mn r}(\hat{y}_\ell)$ . These definitions help introduce the eigenproblem

$$\mathcal{L}\mathbf{K}_{\ell mn r} = i\nu_{\ell mn r}\mathbf{K}_{\ell mn r}, \quad (2.56)$$

where

$$\mathbf{K}_{\ell mn r}(\hat{y}_\ell) = \begin{pmatrix} U_{\ell mn r}(\hat{y}_\ell) \\ V_{\ell mn r}(\hat{y}_\ell) \\ \Phi_{\ell mn r}(\hat{y}_\ell) \end{pmatrix} \quad (2.57)$$

are the eigenfunctions for the horizontal wind and geopotential fields. The eigenvalues of  $\mathcal{L}$  yield the dispersion relation for equatorially-trapped waves satisfying the cubic equation (Matsuno, 1966)

$$\epsilon_\ell \hat{\nu}_{\ell mn r}^2 - m^2 - \frac{m}{\hat{\nu}_{\ell mn r}} = \epsilon_\ell^{1/2} (2n + 1), \quad (2.58)$$

where  $n = 0, 1, 2, \dots$  is the index for the meridional mode and  $\hat{\nu}_{\ell mn r} = \nu_{\ell mn r}/2\Omega$  is the dimensionless wave frequency. This dispersion relation can be found by solving the unforced ( $F, G,$  and  $Q = 0$ ), non-dissipative ( $\alpha = 0$ ) version of (2.51). We also define  $r = 0, 1, 2$  as the three roots of the dispersion relation (2.58), so that the eigenfunctions and eigenvalues are characterized by the indices  $\ell mn r$ . Special care is required for the case  $n = 0$ , where (2.58) can be factored into  $(\epsilon_\ell^{1/2}\hat{\nu}_{\ell mn r} + m)(\epsilon_\ell^{1/2}\hat{\nu}_{\ell mn r}^2 - m\hat{\nu}_{\ell mn r} - 1) = 0$ . The root  $\hat{\nu}_{\ell mn r} = -\epsilon_\ell^{-1/2}m$  must be discarded because the corresponding eigenfunction is unbounded in  $\hat{y}_\ell$ , which violates our assumption that all fields  $\rightarrow 0$  as  $\hat{y}_\ell \rightarrow \pm\infty$ . Thus, when  $n = 0$ ,

only the two solutions of  $\epsilon_\ell^{1/2}\hat{\nu}_{\ell mnr}^2 - m\hat{\nu}_{\ell mnr} - 1 = 0$  are retained and are indexed by  $r = 0$  and  $r = 2$ . The index  $r = 0$  corresponds to the mixed Rossby-gravity wave, and  $r = 2$  corresponds to an eastward inertia-gravity wave. The eigenfunctions for Kelvin waves can be found separately by setting  $V_{\ell mnr}$  to zero in (2.57). The Kelvin wave eigenvalues  $\hat{\nu}_{\ell mnr} = \epsilon_\ell^{-1/2}m$  can be formally considered as solutions to (2.58) when  $n = -1$ . The root of this solution is indexed as  $r = 2$ .

For a given value of  $n$ ,  $\mathbf{K}_{\ell mnr}(\hat{y}_\ell)$  is the eigenfunction corresponding to the eigenvalue  $\nu_{\ell mnr}$ . The form of  $\mathbf{K}_{\ell mnr}(\hat{y}_\ell)$  for all waves, except Kelvin waves, is given by

$$\mathbf{K}_{\ell mnr}(\hat{y}_\ell) = A_{\ell mnr} \begin{pmatrix} \epsilon_\ell^{\frac{1}{4}} \left[ \left(\frac{n+1}{2}\right)^{\frac{1}{2}} (\epsilon_\ell^{\frac{1}{2}}\hat{\nu}_{\ell mnr} + m)\mathcal{H}_{n+1}(\hat{y}_\ell) + \left(\frac{n}{2}\right)^{\frac{1}{2}} (\epsilon_\ell^{\frac{1}{2}}\hat{\nu}_{\ell mnr} - m)\mathcal{H}_{n-1}(\hat{y}_\ell) \right] \\ -i(\epsilon_\ell\hat{\nu}_{\ell mnr}^2 - m^2)\mathcal{H}_n(\hat{y}_\ell) \\ c_\ell\epsilon_\ell^{\frac{1}{4}} \left[ \left(\frac{n+1}{2}\right)^{\frac{1}{2}} (\epsilon_\ell^{\frac{1}{2}}\hat{\nu}_{\ell mnr} + m)\mathcal{H}_{n+1}(\hat{y}_\ell) - \left(\frac{n}{2}\right)^{\frac{1}{2}} (\epsilon_\ell^{\frac{1}{2}}\hat{\nu}_{\ell mnr} - m)\mathcal{H}_{n-1}(\hat{y}_\ell) \right] \end{pmatrix}, \quad (2.59)$$

and the form of  $\mathbf{K}_{\ell m-12}(\hat{y}_\ell)$  for Kelvin waves is

$$\mathbf{K}_{\ell m-12}(\hat{y}_\ell) = A_{\ell m-12} e^{-\frac{1}{2}\hat{y}_\ell^2} \begin{pmatrix} 1 \\ 0 \\ c_\ell \end{pmatrix}, \quad (2.60)$$

where

$$A_{\ell mnr} = \begin{cases} \left[ \epsilon_\ell^{\frac{1}{2}} (n+1) \left( \epsilon_\ell^{\frac{1}{2}}\nu_{\ell mnr} + m \right)^2 + \epsilon_\ell^{\frac{1}{2}} n \left( \epsilon_\ell^{\frac{1}{2}}\nu_{\ell mnr} - m \right)^2 + (\epsilon_\ell\nu_{\ell mnr}^2 - m^2)^2 \right]^{-\frac{1}{2}}, & n \geq 0 \\ 2^{-\frac{1}{2}}\pi^{-\frac{1}{4}}, & n = -1, \end{cases} \quad (2.61)$$

is the normalization factor of the orthonormality property

$$(\mathbf{K}_{\ell mnr}(\hat{y}_\ell), \mathbf{K}_{\ell, m, n', r'}(\hat{y}_\ell)) = \begin{cases} 1 & (n', r') = (n, r), \\ 0 & (n', r') \neq (n, r). \end{cases} \quad (2.62)$$

The normalization factor and its orthonormality property make the mathematical derivation more convenient. The normality part of (2.62) is confirmed by substituting (2.59) into the left hand side of (2.51) and then using

$$\int_{-\infty}^{\infty} \mathcal{H}_n(\hat{y}_\ell) \mathcal{H}_{n'}(\hat{y}_\ell) d\hat{y}_\ell = \begin{cases} 1 & n' = n, \\ 0 & n' \neq n, \end{cases} \quad (2.63)$$

in order to evaluate the three resulting integrals. The Hermite functions  $\mathcal{H}_n(\hat{y}_\ell)$  are related to the Hermite polynomials  $H_n(\hat{y}_\ell)$  by

$$\mathcal{H}_n(\hat{y}_\ell) = (\pi^{\frac{1}{2}} 2^n n!)^{-\frac{1}{2}} H_n(\hat{y}_\ell) e^{-\frac{1}{2}\hat{y}_\ell^2}. \quad (2.64)$$

The Hermite functions  $\mathcal{H}_n(\hat{y}_\ell)$  satisfy the recurrence relation

$$\hat{y}_\ell \mathcal{H}_n(\hat{y}_\ell) = \left(\frac{n+1}{2}\right)^{\frac{1}{2}} \mathcal{H}_{n+1}(\hat{y}_\ell) + \left(\frac{n}{2}\right)^{\frac{1}{2}} \mathcal{H}_{n-1}(\hat{y}_\ell), \quad (2.65)$$

and the derivative relation

$$\frac{d\mathcal{H}_n(\hat{y}_\ell)}{d\hat{y}_\ell} = -\left(\frac{n+1}{2}\right)^{\frac{1}{2}} \mathcal{H}_{n+1}(\hat{y}_\ell) + \left(\frac{n}{2}\right)^{\frac{1}{2}} \mathcal{H}_{n-1}(\hat{y}_\ell). \quad (2.66)$$

The first two Hermite functions are  $\mathcal{H}_0(\hat{y}_\ell) = \pi^{-\frac{1}{4}} e^{-\frac{1}{2}\hat{y}_\ell^2}$  and  $\mathcal{H}_1(\hat{y}_\ell) = 2^{\frac{1}{2}} \pi^{-\frac{1}{4}} \hat{y}_\ell e^{-\frac{1}{2}\hat{y}_\ell^2}$ , from which all succeeding structure functions can be computed using the recurrence relation (2.23). Computing  $\mathcal{H}_n(\hat{y}_\ell)$  via its recurrence relation is much preferable to computing  $H_n(\hat{y}_\ell)$  via its recurrence relation and then computing  $\mathcal{H}_n(\hat{y}_\ell)$  by evaluation of the right hand side of 2.64, because the former method avoids explicit calculation of the factor  $2^n n!$  for large  $n$ . Plots of  $\mathcal{H}_n(\hat{y}_1)$  for  $n = 0, 1, 2, 3$ , and 4 are shown in Fig. 2.2.

One should also note that there is a degeneracy in the zonally symmetric Rossby modes when  $m = 0, n > 0, r = 0$ , and for zonally symmetric Kelvin waves when  $m = 0, n = -1, r = 2$  in which case (2.59) is indeterminate because both  $m$  and  $\hat{\nu}_{\ell 0 n 0}$  vanish. However, orthonormal eigenfunctions are easily constructed in this case

$$\mathbf{K}_{\ell 0 n 0}(\hat{y}_\ell) = (2n+1)^{-\frac{1}{2}} \begin{pmatrix} \left[ \left(\frac{n}{2}\right)^{\frac{1}{2}} \mathcal{H}_{n+1}(\hat{y}_\ell) - \left(\frac{n+1}{2}\right)^{\frac{1}{2}} \mathcal{H}_{n-1}(\hat{y}_\ell) \right] \\ 0 \\ c_\ell \left[ \left(\frac{n}{2}\right)^{\frac{1}{2}} \mathcal{H}_{n+1}(\hat{y}_\ell) + \left(\frac{n+1}{2}\right)^{\frac{1}{2}} \mathcal{H}_{n-1}(\hat{y}_\ell) \right] \end{pmatrix}. \quad (2.67)$$

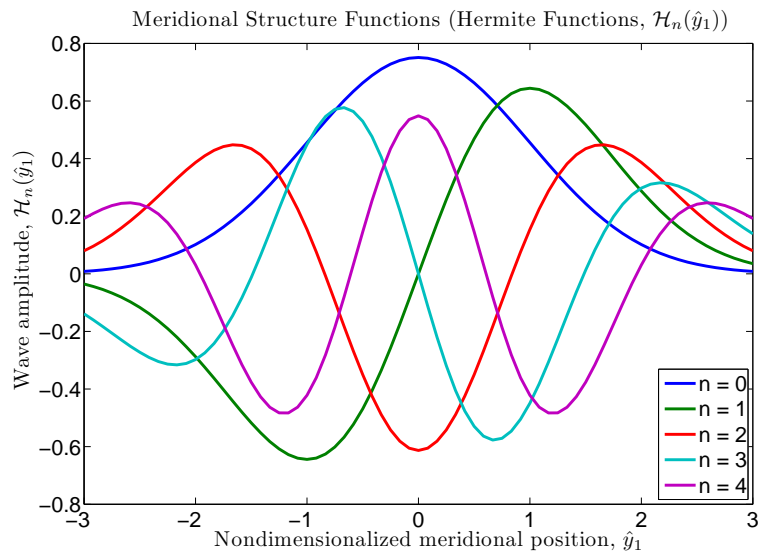


Figure 2.2:  $\mathcal{H}_n(\hat{y}_\ell)$  for  $\ell = 1$  ( $\epsilon_1 = 323.42$ , equivalent depth = 272.23 m) and  $n = 0, 1, 2, 3, 4$  over the equatorial band (35°S, 35°N). These satisfy the orthonormality condition (2.63). Note that  $\hat{y}_\ell$  gets larger as  $\ell$  increases.

Due to the orthonormality and completeness of the eigenfunctions  $\mathbf{K}_{\ell mnr}(\hat{y}_\ell)$  we can set up the transform pair (Silva Dias et al. 1983; DeMaria 1985)

$$\eta_{\ell mnr}(t) = (\eta_{\ell m}(\hat{y}_\ell, t), \mathbf{K}_{\ell mnr}(\hat{y}_\ell)), \quad (2.68)$$

$$\eta_{\ell m}(\hat{y}_\ell, t) = \sum_{n=-1}^{\infty} \sum_r \eta_{\ell mnr}(t) \mathbf{K}_{\ell mnr}(\hat{y}_\ell), \quad (2.69)$$

where  $\eta_{\ell mnr}$  are the scalar coefficients in the normal mode expansion of the vector  $\eta_{\ell m}(\hat{y}_\ell)$ . Note that (2.68) can be computed by taking the inner product of (2.69) with  $\mathbf{K}_{\ell mn'r'}(\hat{y}_\ell)$  using the orthonormality property (2.62).

Now we have the tools needed in order to solve (2.51). Begin by taking the inner product of (2.51) with the eigenfunction  $\mathbf{K}_{\ell mnr}(\hat{y}_\ell)$ ,

$$\left( \left( \frac{\partial}{\partial t} + \alpha \right) \boldsymbol{\eta}_{\ell m}(\hat{y}_\ell), \mathbf{K}_{\ell mnr}(\hat{y}_\ell) \right) + (\mathcal{L} \boldsymbol{\eta}_{\ell m}(\hat{y}_\ell), \mathbf{K}_{\ell mnr}(\hat{y}_\ell)) = (\boldsymbol{\mathcal{E}}_{\ell m}(\hat{y}_\ell), \mathbf{K}_{\ell mnr}(\hat{y}_\ell)),$$

next use the Skew-Hermitian property of  $\mathcal{L}$  and take the constants outside of the inner products,

$$\left( \frac{\partial}{\partial t} + \alpha \right) (\boldsymbol{\eta}_{\ell m}(\hat{y}_\ell), \mathbf{K}_{\ell mnr}(\hat{y}_\ell)) + (\boldsymbol{\eta}_{\ell m}(\hat{y}_\ell), -\mathcal{L} \mathbf{K}_{\ell mnr}(\hat{y}_\ell)) = (\boldsymbol{\mathcal{E}}_{\ell m}(\hat{y}_\ell), \mathbf{K}_{\ell mnr}(\hat{y}_\ell)).$$

Now we can use the relations (2.56), (2.68) and the inner product relation

$\mathcal{E}_{\ell mnr} = (\boldsymbol{\mathcal{E}}_{\ell m}(\hat{y}_\ell), \mathbf{K}_{\ell mnr}(\hat{y}_\ell))$  and obtain

$$\frac{\partial \eta_{\ell mnr}}{\partial t} + (\alpha + i\nu_{\ell mnr}) \eta_{\ell mnr} = \mathcal{E}_{\ell mnr}(t). \quad (2.70)$$

This first order differential equation in time must be solved for the unknown scalar field  $\eta_{\ell mnr}(t)$  using the integrating factor method, which yields

$$\eta_{\ell mnr}(t) = \int_0^t e^{-(\alpha + i\nu_{\ell mnr})(t-t')} \mathcal{E}_{\ell mnr}(t') dt'. \quad (2.71)$$

## 2.5 Final Solution of the Prognostic Fields

We have reduced the set of vector form partial differential equations for fluid motion (2.51) to one ordinary differential equation in time (2.70), which can be easily solved.

The solutions correspond to the time evolution of  $\eta_{\ell mnr}$ ; initially  $\eta_{\ell mnr} = 0$  and then exponentially decays as  $t$  evolves according to  $\alpha + i\nu_{\ell mnr}$ . The physical space fields now can be computed using the inverse vertical normal mode, Fourier, and Hermite transforms: (2.15), (2.47), and (2.69) of the spectral space fields, i.e.,

$$\begin{pmatrix} u(x, y, z, t) \\ v(x, y, z, t) \\ \phi(x, y, z, t) \end{pmatrix} = \sum_{\ell=0}^{\infty} \sum_{m=-\infty}^{\infty} \sum_{n=-1}^{\infty} \sum_r \mathcal{Z}_{\ell}(z) e^{imx/a} \begin{pmatrix} U_{\ell mnr}(\hat{y}_{\ell}) \\ V_{\ell mnr}(\hat{y}_{\ell}) \\ \Phi_{\ell mnr}(\hat{y}_{\ell}) \end{pmatrix} \eta_{\ell mnr}(t). \quad (2.72)$$

We can use (2.7) to compute the physical space “vertical log-pressure velocity” field and (2.3) to recover the temperature field. We can also calculate the vertical pressure-velocity (hPa day<sup>-1</sup>) using the relationship  $\omega = -\frac{p_0}{H} e^{-z/H} w$ .

In the next section we will explain the different experiments that will be analyzed and the motivation behind the model formulation. Numerical values for constant variables will be given, as well as the exact forms of the diabatic heating and BL frictional forces.

## Chapter 3

### METHODS - EXPERIMENT LAYOUT AND MODEL FORCINGS

In this chapter we specify the exact form of the forcings and the numerical values of all variables and constants. The setup for each model run will be described as well as the model solutions of the primitive equations that were given in Chapter 2.

We begin by introducing the form of the horizontal and vertical structure of the prescribed diabatic forcings  $Q(x, y, z)$ . The diabatic forcing is of the form of a localized heat source. The heat source may have two forms, one for deep heating profiles and the other for shallow heating profiles.

#### 3.1 Deep Heating Profile

The prescribed deep heating profile has a spatial structure of the form

$$Q(x, y, z) = Q_0 X(x) Y(y) Z(z), \quad (3.1)$$

where  $Q_0$  is the peak heating,

$$Z(z) = \sin\left(\frac{\pi z}{z_T}\right), \quad (3.2)$$

$z_T$  is the height of the top of the troposphere, and  $X(x)$  and  $Y(y)$  are the zonal and meridional structure of the deep heating which will be described later. The vertical structure of the deep heating that we have assumed is strictly positive and normalized for convenience. We shall assume  $Q_0 = 3.75$  or  $7.5 \text{ K day}^{-1}$  (explained in next chapter) and  $z_T = H \ln(p_T/p_0)$ , where  $p_T = 200 \text{ hPa}$ . The maximum heating rate and the pressure level of the top of the troposphere are based on their respective values observed in Yanai et al. (1973). The

vertical profile for our prescribed deep heating  $Q$  and the deep heating profiles observed in Yanai et al. (1973) are illustrated in Fig. 3.1. The vertical structure projects mostly

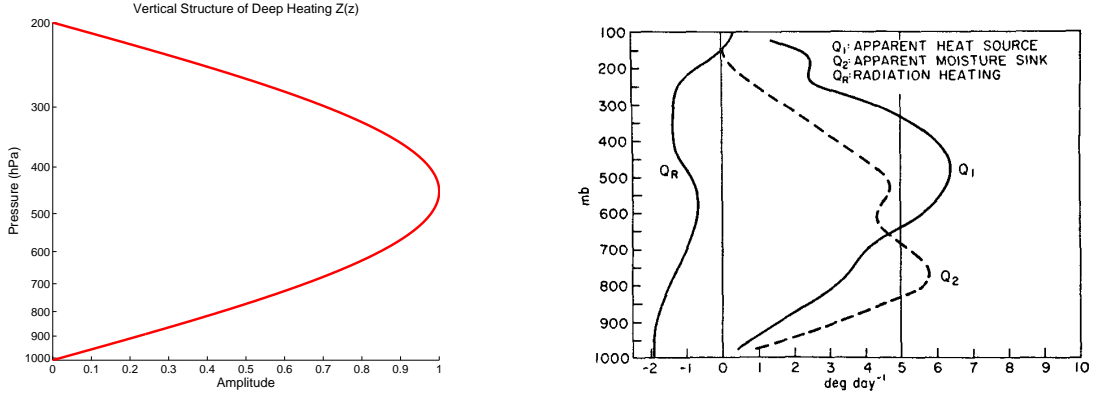


Figure 3.1: The vertical structure of the normalized prescribed deep heating profile,  $Z(z)$ , (left) and the deep heating observed in Yanai et al. (1973),  $Q_1(z)$ , (right). The maximum heating for both profiles is in the mid-troposphere and the tropopause is around 100-200 hPa. Note that  $Q_R$  stays relatively constant with height.

on the external  $\ell = 0$  mode and the first three internal modes ( $\ell = 1 - 3$ ). This agrees well with the findings of Fulton and Schubert (1985), where  $Q_1$  profiles from the Global Atmospheric Research Project (GARP) Atlantic Tropical Experiment (GATE) for “undisturbed” and “disturbed” periods were compared. Deep heating profiles consist of positive heating throughout most of the troposphere with a peak amplitude in the mid-troposphere. Yanai et al. (1973) suggest that this peak occurs in the 400-550 hPa layer near a secondary maximum in entrainment.

The prescribed zonal structure of the deep heating profile is of the form

$$X(x) = \frac{1}{2} \begin{cases} 1 + \cos\left(\frac{\pi x}{a_0}\right) & |x| \leq a_0, \\ 0 & |x| \geq a_0, \end{cases} \quad (3.3)$$

where  $a_0$  is the zonal half width. The zonal structure is a strictly positive half cosine wave with a maximum value at  $x = 0$  km, and has been normalized for convenience.

The meridional structure of the deep heating profile is of the form

$$Y(y) = \exp\left[-\left(\frac{y - y_d}{b}\right)^2\right], \quad (3.4)$$

where  $y_d$  is the center of the heat source and  $b$  the meridional e-folding width. We have assumed that (3.4) is also strictly positive and normalized for convenience. The meridional structure is Gaussian with a maximum value at  $y = 0$  km and  $Y(y) \rightarrow 0$  as  $y \rightarrow \infty$  as required by the equatorial  $\beta$ -plane approximation. The horizontal structure  $X(x)Y(y)$  is in the shape of an ellipse, acting to simulate the Intertropical Convergence Zone (ITCZ). This horizontal structure of this forcing is simple, but has been shown to represent the atmosphere well in many other theoretical studies.

### 3.2 Shallow Non-Precipitating Heating Profile

The prescribed shallow heating profile has a spatial structure of the form

$$Q(x, y, z) = Q_0 X(x) Y(y) Z(z), \quad (3.5)$$

where  $Q_0$  is the peak heating,

$$Z(z) = \begin{cases} \sin\left(\frac{2\pi z}{z_I}\right) & 0 \leq z \leq z_I, \\ 0 & z_I \leq z \leq z_T, \end{cases} \quad (3.6)$$

where  $z_I$  is the value of  $z$  at the trade-wind inversion, and  $X(x)$  and  $Y(y)$  are the same as in (3.3) and (3.4). The horizontal structure  $X(x)Y(y)$  is illustrated in Fig. 3.2. We shall assume  $Q_0 = 2.5 \text{ K day}^{-1}$  and  $z_I = H \ln(p_I/p_0)$ , where  $p_I = 700 \text{ hPa}$ . The maximum heating rate and pressure level of the trade-wind inversion are based on the respective values observed in Nitta and Esbensen (1974). The heating profile for our prescribed shallow heating  $Q$  and the “undisturbed” shallow heating observed in Nitta and Esbensen (1974) are illustrated in Fig. 3.3. The vertical structure of the shallow heating is based on numerous studies suggesting that shallow non-precipitating heating is defined with a trade-wind inversion near or just above the top of the boundary layer (BL). Nitta and Esbensen (1974) suggest that just below the trade-wind inversion there is significant cooling and moistening associated with detrainment of clouds during the “undisturbed” (shallow heating) period. Below this cooling and moistening is heating and drying associated with the buildup of

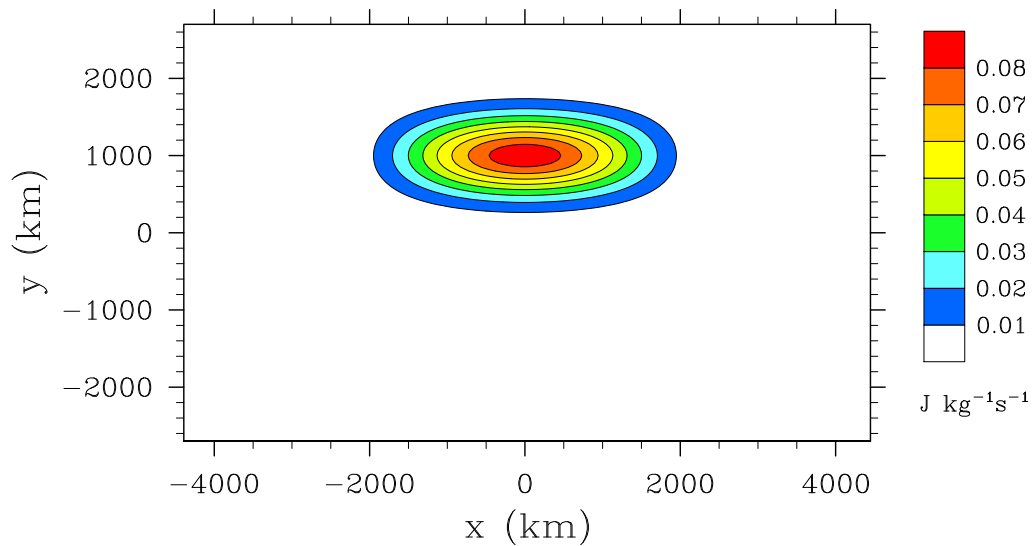


Figure 3.2: The horizontal structure  $Q_0 X(x) Y(y)$  used in the prescribed deep and shallow heating profiles. The constants are  $Q_0 = 7.5 \text{ K day}^{-1}$ ,  $a_0 = 2500 \text{ km}$ ,  $b = 500 \text{ km}$ , and  $y_d = 1000 \text{ km}$ . The contour interval is  $0.01 \text{ J kg}^{-1} \text{ s}^{-1}$ .

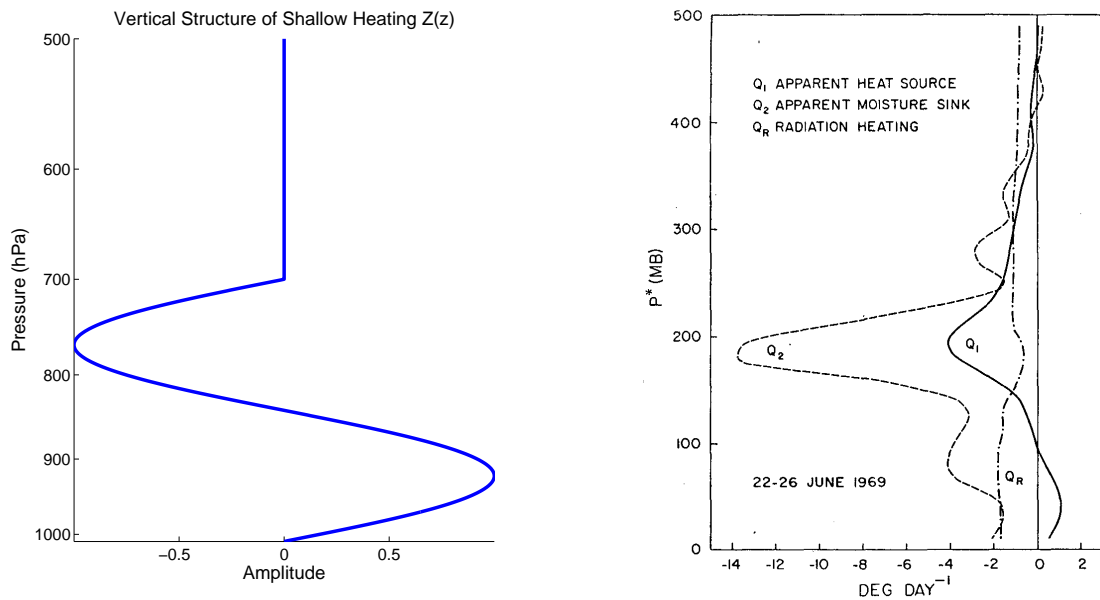


Figure 3.3: The vertical structure of the prescribed shallow heating profile,  $Z(z)$ , (left) and the deep heating observed in Nitta and Esbensen (1974),  $Q_1$ , (right). The maximum heating for both profiles is within the first 100 hPa of the surface and the trade inversion is in the vicinity of 150-400 hPa above the surface. Note that the vertical axis in the figure on the left is  $p$  and the right figure is  $p^* = p_s - p$ , where  $p_s$  is the surface pressure and that  $Q_R$  stays relatively constant with height.

non-precipitating shallow cumulus clouds. Vertical eddy transport of total heat decreases rapidly just above the inversion while the moisture sink and heat source terms go to zero.

According to Nitta and Esbensen (1974) the differences between “disturbed” versus “undisturbed” convective days depends greatly on BL processes. If convection can break through the trade-wind inversion, then heating profiles can transition from shallow non-precipitating to either shallow precipitating, stratiform, and/or deep, emphasizing the importance of representing planetary BL forcings accurately. More complicated heating profiles are to be looked at in future studies. Since we have already introduced the spatial structure of the diabatic heating forcings, we will now introduce the PBL frictional forcings.

### 3.3 Planetary Boundary Layer Frictional Profile

The prescribed PBL frictional forcings have a spatial structure of the form

$$F(x, y, z) = F_0 X(x) Y(y) Z(z), \quad (3.7)$$

$$G(x, y, z) = G_0 X(x) Y(y) Z(z), \quad (3.8)$$

where  $X(x)$  is the same as (3.3),  $F_0$  and  $G_0$  are the peak amplitudes of the zonal and meridional BL frictional forcings, respectively. The vertical structure  $Z(z)$  is

$$Z(z) = \frac{1}{2} \begin{cases} 1 + \cos\left(\frac{\pi z}{z_B}\right) & 0 \leq z \leq z_B, \\ 0 & z_B \leq z \leq z_T, \end{cases} \quad (3.9)$$

where  $z_B = H \ln(p_B/p_0)$  is the value of  $z$  at the top of the BL, and  $p_B = 800$  hPa. The vertical structure of  $F$  and  $G$  is shown in Fig. 3.4. The meridional structure  $Y(y)$  of the frictional forcings is slightly different than the meridional structure of the diabatic heating forcings, since we prescribe its derivative to be an ellipse, corresponding to a localized curl of the frictional forcings, or a curl of the wind stress. The zonal winds tend to have a large easterly component just north of the ITCZ and a small westerly component just south of

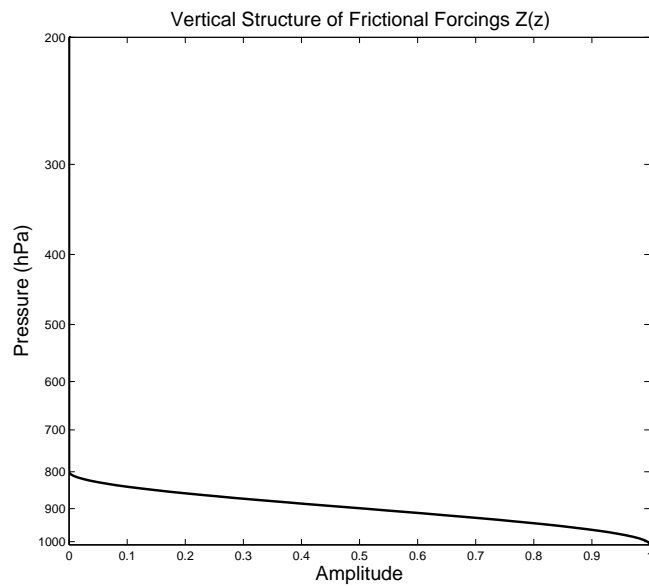


Figure 3.4: The normalized vertical structure  $Z(z)$  used in the prescribed BL frictional profiles, where  $p_B = 800$  hPa.

the ITCZ (Fig. 1.11), therefore we define the meridional structure of  $F$  to be

$$Y(y) = -2^{1/2} e^{1/2} \left( \frac{y - y_d}{b} \right) \exp \left[ - \left( \frac{y - y_d}{b} \right)^2 \right]. \quad (3.10)$$

It turns out that the meridional winds tend to be much more variable around the ITCZ, but in general they have some component of convergence (Fig. 3.5). Therefore, the

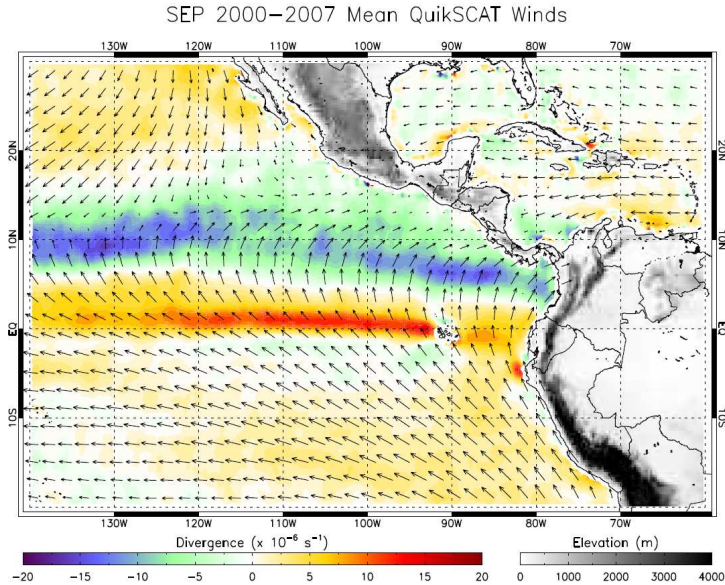


Figure 3.5: Mean winds and divergence in the tropical East Pacific during September 2000-2007. This data was recorded using Quikscat data. From Mora (2008).

meridional structure of  $G$  may be the same as  $F$ . It turns out that this form of meridional structure for  $G$  alone has no effect on the wind stress curl, since the wind stress curl involves  $\partial G / \partial x$ , depending rather on the zonal structure of  $G$ . It does affect the wind stress divergence though, because the wind stress divergence involves  $\partial G / \partial y$ . Overall, the contribution of  $G$  is more complicated, and because of this we will only concentrate on the effect of a zonal frictional forcing,  $F$ .

The form of the meridional structure we have prescribed happens to produce positive wind stress curl and Ekman pumping in the simulated “ITCZ” region, but has a byproduct of two areas of weaker Ekman suction to the north and south (Fig. 3.6). This byproduct is inevitable with the simple analytical meridional structure we have prescribed. However,

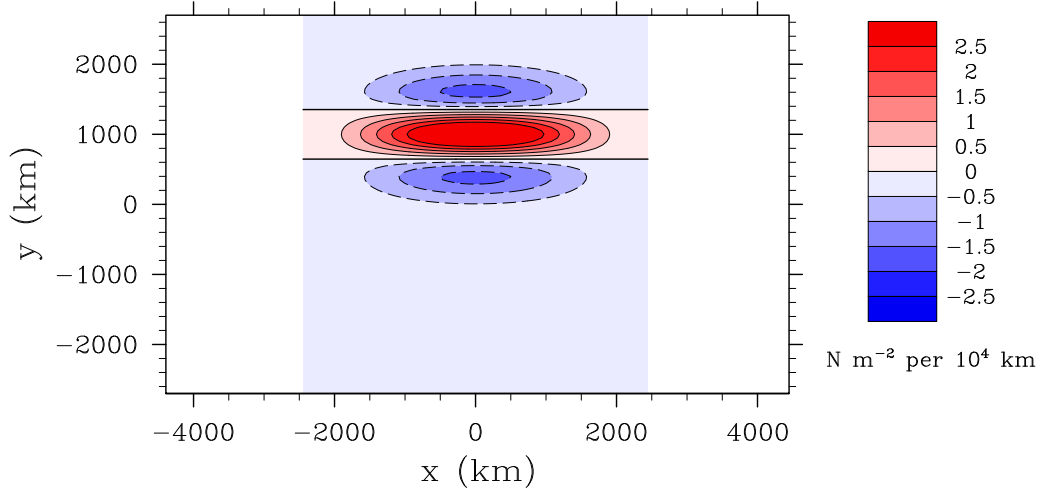


Figure 3.6: The horizontal structure of the prescribed wind stress curl of  $F$ , where  $a_0 = 2500$  km,  $b = 500$  km,  $y_d = 1000$  km,  $p_B = 800$  hPa,  $F_0 = -6.5 \times 10^{-5}$  m s $^{-2}$ , and  $\rho = 1.2$  kg m $^{-3}$ . The contour interval is  $1$  N m $^{-2}$  per  $10^4$  km.

the prescribed horizontal structure of the wind stress curl does look similar to observations from Risien and Chelton (2008) that were plotted in Fig. 1.12.

The vertical structure of the BL frictional forces have a simple form that excludes mixing properties, but are sufficient for this type of theoretical study. In order to get a better visual picture of what the frictional forcing represents, we derive the vertical profile of the zonal and meridional wind stress. First we integrate the equation of the zonal frictional forcing

$$\int_0^z F(x, y, z) dz = \int_0^z \frac{1}{\rho} \frac{\partial \tau_x(x, y, z)}{\partial z} dz. \quad (3.11)$$

We have prescribed  $Z(z)$ , so the left hand side of (3.11) can be solved. If we assume that  $\rho = 1.2$  kg m $^{-3}$  is constant, the zonal wind stress vanishes at the top of the BL  $\tau_x(z = z_B) = 0$ , and that we know  $\tau_x(z = 0)$  from typical or observed values, then we can compute  $F_0$ ,  $G_0$ , and  $\tau_x(z)$ . We follow the same procedure for computing  $\tau_y(z)$ . Typical values of  $\tau_x(0)$  and  $\tau_y(0)$  can be taken from observations and/or approximated by the bulk aerodynamic formula, as done below

$$|\tau_x(0)| = \rho c_d |\mathbf{V}| |\bar{u}|, \quad (3.12)$$

$$|\tau_y(0)| = \rho c_d |\mathbf{V}| |\bar{v}|. \quad (3.13)$$

If  $c_d = 0.0015$ ,  $|\mathbf{V}| = 7.25 \text{ m s}^{-1}$ ,  $u = 6.5 \text{ m s}^{-1}$ ,  $v = 3.25 \text{ m s}^{-1}$ , then  $|\tau_x(0)| \approx 0.08 \text{ N m}^{-2}$ ,  $|\tau_y(0)| \approx 0.04 \text{ N m}^{-2}$ . The vertical structure of the zonal wind stress  $\tau_x(z)$  is

$$\tau_x(z) = \frac{F_0 \rho}{2} \left( z + \frac{z_B}{\pi} \sin \left( \frac{\pi z}{z_B} \right) \right) + \tau_x(0), \quad (3.14)$$

where  $F_0 = -6.5 \times 10^{-5} \text{ m s}^{-2}$ ,  $z_B = H \ln(p_0/p_B)$ ,  $p_B = 800 \text{ hPa}$ , and the vertical structure of the meridional wind stress is

$$\tau_y(z) = \frac{G_0 \rho}{2} \left( z + \frac{z_B}{\pi} \sin \left( \frac{\pi z}{z_B} \right) \right) + \tau_y(0), \quad (3.15)$$

where  $G_0 = -3.25 \times 10^{-5} \text{ m s}^{-2}$ . The vertical structure of the zonal wind stress  $\tau_x(z)$  is shown in Fig. 3.7.

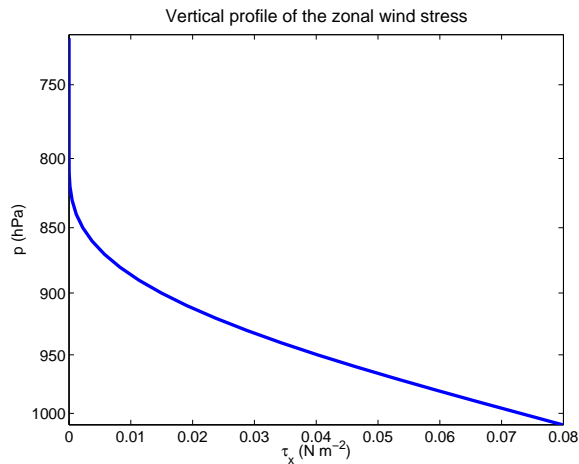


Figure 3.7: The vertical structure of the zonal wind stress  $\tau_x(z)$  used for the BL frictional forcing  $F$ . The constants used are  $p_B = 800 \text{ hPa}$ ,  $F_0 = -6.5 \times 10^{-5} \text{ m s}^{-2}$ , and  $\rho = 1.2 \text{ kg m}^{-3}$ .

### 3.4 Accuracy of Forcings in Spectral Space

The horizontal and vertical structure of our prescribed forcings may have many forms, but with our simple model formulation these forms must be accurately represented in spectral space. Therefore we must validate that the zonal, meridional, and vertical structure of all of the forcings can be properly represented. The way we shall do this is by comparing the form of the forcings before taking any spectral transforms to the form of the forcings after

computing a spectral transform and their associated inverse transform. The errors that are presented are computed as the magnitude of the difference between the two spatial profiles at each point divided by the maximum amplitude of the original prescribed forcing. Since the maximum amplitude of the spatial structure for all of the forcings equals one (except for the vertical structure of the deep and shallow heating), the error can also be interpreted as the difference between the two spatial profiles.

First we shall view the spectral transforms of the zonal structure. Remember, the zonal structure  $X(x)$  is the same for all of the prescribed forcings. After computing a Fourier transform we obtain

$$\mathcal{X}_m = \frac{1}{2\pi a} \int_{-\pi a}^{\pi a} X(x) e^{-imx/a} dx = \frac{\pi}{2} \frac{\sin(ma_0/a)}{m(\pi^2 - m^2 a_0^2/a^2)}, \quad (3.16)$$

and after computing the inverse Fourier transform we come to

$$X(x) = \sum_{m=-M}^M \mathcal{X}_m e^{imx/a}. \quad (3.17)$$

We find that using  $M = 40$  is sufficient to represent the zonal structure of the forcings. The maximum error associated with  $M = 40$  is  $\approx 0.36\%$  (Fig. 3.8).

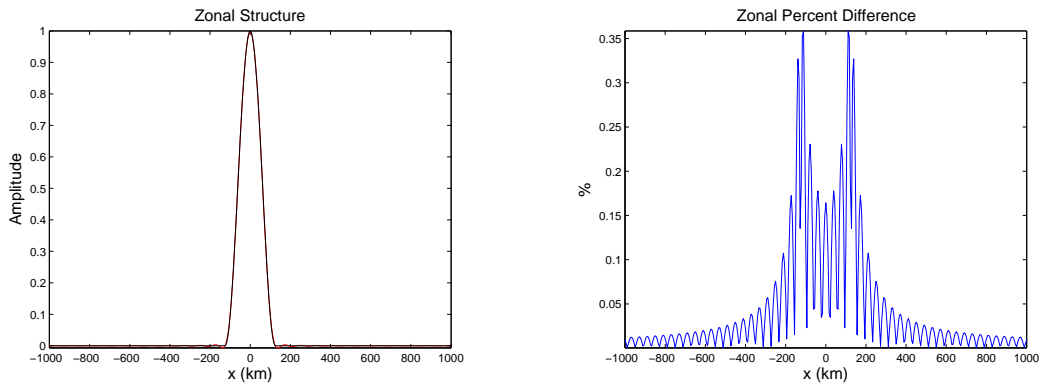


Figure 3.8: The zonal structure of all of the forcings before taking the Fourier transform (black) and after taking the Fourier transform (red). The percent error (or difference) between the zonal structure before and after taking the Fourier transforms (blue).

Now we shall view the spectral transforms of the meridional structure. The compu-

tation of the Hermite transform for the deep and shallow heating profiles yields

$$\mathcal{Y}_{\ell n} = \int_{-\infty}^{\infty} Y_{\ell}(\hat{y}) \mathcal{H}_n(\hat{y}) d\hat{y} = \left( \frac{2\pi \hat{b}_{\ell}^2}{2 + \hat{b}_{\ell}^2} \right)^{\frac{1}{2}} \exp\left( \frac{\hat{b}_{\ell}^2 \hat{y}_0^2}{4 - \hat{b}_{\ell}^4} \right) \left( \frac{2 + \hat{b}_{\ell}^2}{2 - \hat{b}_{\ell}^2} \right)^{\frac{n}{2}} \mathcal{H}_n \left( \frac{2\hat{y}_0}{(4 - \hat{b}_{\ell}^4)^{\frac{1}{2}}} \right),$$

$$0 \leq \hat{b}_{\ell} < 2^{\frac{1}{2}},$$
(3.18)

and taking an inverse Hermite transform gives the result below

$$Y_{\ell}(y) = \sum_{n=0}^N \mathcal{Y}_{\ell n} \mathcal{H}_n(\hat{y}).$$
(3.19)

We find that using  $N = 250$  is sufficient to represent the meridional structure of the deep and shallow heating forcings. The maximum error associated with  $N = 250$  is  $\approx 2.5 \times 10^{-6}\%$  (when  $\ell = 1$ ) (Fig. 3.9). Note that the errors decrease as vertical wavenumber  $\ell$  increases

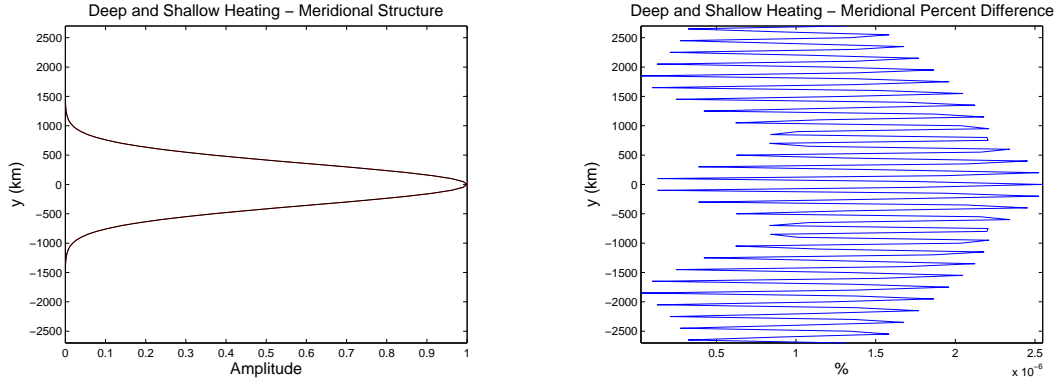


Figure 3.9: The meridional structure of the deep and shallow heating forcings before taking the Hermite transform (black) and after taking the Hermite transform (red). The percent error (or difference) between the meridional structure before and after taking the Hermite transforms (blue).

for the internal modes. Despite the exceptional accuracy for internal modes, the accuracy of the external mode ( $\ell = 0$ ) isn't nearly as good, with a maximum error of  $\approx 2\%$ . One would need to use  $N = 400$  to attain a maximum error  $< 1\%$ , which is too expensive for such a simple model. This owes to the fact that the equatorial  $\beta$ -plane model breaks down for the external (barotropic) mode, where the gravity wave speed is very large ( $c_0 = 271.2708 \text{ m s}^{-1}$ ).

Now after we compute a Hermite transform for the frictional forcing profiles we arrive at

$$\mathcal{Y}_{\ell n} = \int_{-\infty}^{\infty} Y_{\ell}(\hat{y}) \mathcal{H}_n(\hat{y}) d\hat{y}, \quad (3.20)$$

$$\begin{aligned} \mathcal{Y}_{\ell n} = & -2e^{1/2} \left( \frac{\pi}{2 + \hat{b}_{\ell}^2} \right)^{\frac{1}{2}} \exp \left( \frac{\hat{b}_{\ell}^2 \hat{y}_0^2}{4 - \hat{b}_{\ell}^4} \right) \left\{ \left( \frac{n+1}{2} \right)^{1/2} \left( \frac{2 + \hat{b}_{\ell}^2}{2 - \hat{b}_{\ell}^2} \right)^{\frac{n+1}{2}} \mathcal{H}_{n+1} \left( \frac{2\hat{y}_0}{(4 - \hat{b}_{\ell}^4)^{\frac{1}{2}}} \right) \right. \\ & \left. - \hat{y}_0 \left( \frac{2 + \hat{b}_{\ell}^2}{2 - \hat{b}_{\ell}^2} \right)^{\frac{n}{2}} \mathcal{H}_n \left( \frac{2\hat{y}_0}{(4 - \hat{b}_{\ell}^4)^{\frac{1}{2}}} \right) + \left( \frac{n}{2} \right)^{1/2} \left( \frac{2 + \hat{b}_{\ell}^2}{2 - \hat{b}_{\ell}^2} \right)^{\frac{n-1}{2}} \mathcal{H}_{n-1} \left( \frac{2\hat{y}_0}{(4 - \hat{b}_{\ell}^4)^{\frac{1}{2}}} \right) \right\} \\ & 0 \leq \hat{b}_{\ell} < 2^{\frac{1}{2}}, \end{aligned} \quad (3.21)$$

and after taking an inverse Hermite transform we are able compute

$$Y_{\ell}(y) = \sum_{n=0}^N \mathcal{Y}_{\ell n} \mathcal{H}_n(\hat{y}). \quad (3.22)$$

We find that using  $N = 350$  is sufficient to represent the meridional structure of the BL frictional forcings. The maximum error associated with  $N = 350$  is about  $1.8 \times 10^{-6}$  %, when  $\ell = 1$  (Fig. 3.10). Once again, the errors decrease as vertical wavenumber  $\ell$  increases

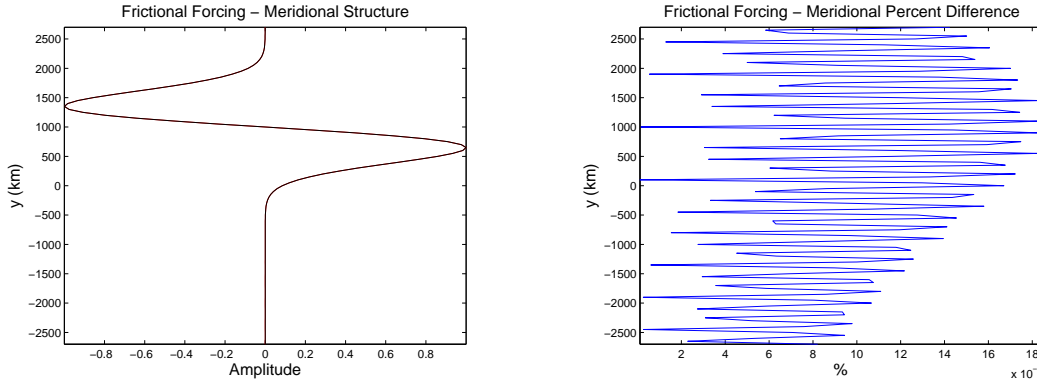


Figure 3.10: The meridional structure of the frictional forcings before taking the Hermite transform (black) and after taking the Hermite transform (red). The percent error (or difference) between the meridional structure before and after taking the Hermite transforms (blue). Note that  $y_d = 1000$  km in both plots.

for internal modes, and the maximum error for the external mode is  $\approx 3\%$ .

Now we shall view the vertical structure and its spectral transforms. The deep heating profile is composed mostly using the external mode and the first three internal modes ( $\ell = 1 - 3$ ), as mentioned before. The normal mode transform of the deep heating forcing is

$$\begin{aligned} \mathcal{V}_\ell = \int_0^{z^*} \mathcal{V}(z) \mathcal{Z}_\ell(z) e^{-z/H} dz = \frac{\mathcal{N}_0}{2} \left[ -I_1 - I_2 + I_3 + I_4 - \frac{\gamma}{\mu_0} (-I_1 + I_2 + I_3 - I_4) \right] \\ + \frac{\mathcal{N}_\ell}{2} \left[ -I_5 - I_6 + I_7 - \frac{\gamma}{\lambda_\ell} (-I_8 + I_9 + I_{10}) \right], \end{aligned} \quad (3.23)$$

where we have defined  $\mathcal{V}(z)$  as

$$\mathcal{V}(z) = \left( \frac{\partial}{\partial t} + \alpha \right) \tilde{\phi}(z), \quad (3.24)$$

$$\begin{aligned} I_1 &= \frac{(\mu_0 - 1/2H)}{(\pi/z^*)^2 + (\mu_0 - 1/2H)^2} \left( e^{(\mu_0 - 1/2H)z^*} + 1 \right), \\ I_2 &= -\frac{(\mu_0 + 1/2H)}{(\pi/z^*)^2 + (\mu_0 + 1/2H)^2} \left( e^{-(\mu_0 + 1/2H)z^*} + 1 \right), \\ I_3 &= \frac{1}{(\mu_0 - 1/2H)} \left( e^{(\mu_0 - 1/2H)z^*} - 1 \right), \\ I_4 &= -\frac{1}{(\mu_0 + 1/2H)} \left( e^{-(\mu_0 + 1/2H)z^*} - 1 \right), \\ I_5 &= \frac{1}{(\pi/z^* - \lambda_\ell)^2 + 1/4H^2} \left\{ e^{-z^*/2H} \left[ \left( \frac{\pi}{z^*} - \lambda_\ell \right) \sin(\lambda_\ell z^*) + \frac{1}{2H} \cos(\lambda_\ell z^*) \right] \right\}, \\ I_6 &= -\frac{1}{(\pi/z^* + \lambda_\ell)^2 + 1/4H^2} \left\{ e^{-z^*/2H} \left[ \left( \frac{\pi}{z^*} + \lambda_\ell \right) \sin(\lambda_\ell z^*) - \frac{1}{2H} \cos(\lambda_\ell z^*) \right] \right\}, \\ I_7 &= \frac{2}{\lambda_\ell^2 + 1/4H^2} \left\{ e^{-z^*/2H} \left[ \lambda_\ell \sin(\lambda_\ell z^*) - \frac{1}{2H} (\cos(\lambda_\ell z^*) + 1) \right] \right\}, \\ I_8 &= \frac{1}{(\pi/z^* + \lambda_\ell)^2 + 1/4H^2} \left\{ e^{-z^*/2H} \left[ \frac{1}{2H} \sin(\lambda_\ell z^*) + \left( \frac{\pi}{z^*} + \lambda_\ell \right) (\cos(\lambda_\ell z^*) + 1) \right] \right\}, \\ I_9 &= -\frac{1}{(\pi/z^* - \lambda_\ell)^2 + 1/4H^2} \left\{ e^{-z^*/2H} \left[ \frac{1}{2H} \sin(\lambda_\ell z^*) - \left( \frac{\pi}{z^*} - \lambda_\ell \right) (\cos(\lambda_\ell z^*) - 1) \right] \right\}, \\ I_{10} &= -\frac{2}{\lambda_\ell^2 + 1/4H^2} \left\{ e^{-z^*/2H} \left[ \frac{1}{2H} \sin(\lambda_\ell z^*) + \lambda_\ell (\cos(\lambda_\ell z^*) - 1) \right] \right\}, \end{aligned}$$

and  $z^* = z_T$ . The inverse normal mode transform for the deep heating forcing is

$$\mathcal{V}(z) = \sum_{\ell=0}^{\mathcal{L}} \mathcal{V}_\ell \mathcal{Z}_\ell(z). \quad (3.25)$$

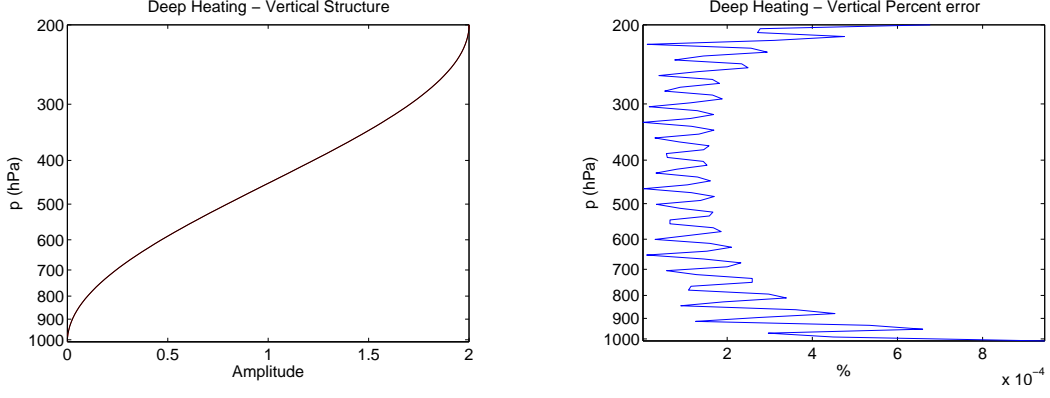


Figure 3.11: The vertical structure of the deep heating forcing before taking the normal mode transform (black) and after taking the normal mode transform (red). The percent error (or difference) between the vertical structure of the frictional forcings before and after taking the normal mode transforms (blue).

Since  $0 \leq \hat{b}_\ell < 2^{1/2}$ ,  $\mathcal{L} = 18$  is the highest vertical wavenumber we can compute. The maximum error associated with  $\mathcal{L} = 18$  is  $\approx 1 \times 10^{-3}\%$  (Fig. 3.11).

After computing a normal mode transform for the shallow heating forcing we have

$$\begin{aligned} \mathcal{V}_\ell = \int_0^{z^*} \mathcal{V}(z) \mathcal{Z}_\ell(z) e^{-z/H} dz = & \frac{\mathcal{N}_0}{2} \left[ -I_1 - I_2 + I_3 + I_4 - \frac{\gamma}{\mu_0} (-I_1 + I_2 + I_3 - I_4) \right] \\ & + \frac{\mathcal{N}_\ell}{2} \left[ -I_5 - I_6 + I_7 - \frac{\gamma}{\lambda_\ell} (-I_8 + I_9 + I_{10}) \right], \end{aligned} \quad (3.26)$$

where  $z^* = z_I/2$ ,

$$\mathcal{V}(z) = \left( \frac{\partial}{\partial t} + \alpha \right) \tilde{\phi}(z), \quad (3.27)$$

and the inverse normal mode transform is

$$\mathcal{V}(z) = \sum_{\ell=0}^{\mathcal{L}} \mathcal{V}_\ell \mathcal{Z}_\ell(z). \quad (3.28)$$

Since  $0 \leq \hat{b}_\ell < 2^{1/2}$ , from (3.18),  $\mathcal{L} = 18$  is the highest vertical wavenumber we can compute.

The maximum error associated with  $\mathcal{L} = 18$  is  $\approx 1.8\%$  (Fig. 3.12). Computation of the normal mode transform for the frictional forcings yields

$$\begin{aligned} \mathcal{V}_\ell = \int_0^{z^*} \mathcal{V}(z) \mathcal{Z}_\ell(z) e^{-z/H} dz = & \frac{\mathcal{N}_0}{2} \left[ I_1 + I_2 + I_3 + I_4 - \frac{\gamma}{\mu_0} (I_1 - I_2 + I_3 - I_4) \right] \\ & + \frac{\mathcal{N}_\ell}{2} \left[ I_5 + I_6 + I_7 - \frac{\gamma}{\lambda_\ell} (-I_8 - I_9 + I_{10}) \right], \end{aligned} \quad (3.29)$$

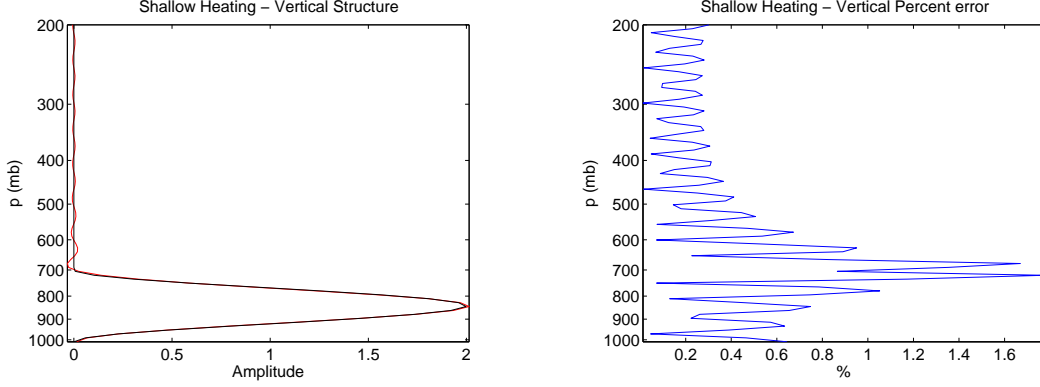


Figure 3.12: The vertical structure of the shallow heating forcing before taking the normal mode transform (black) and after taking the normal mode transform (red). The percent error (or difference) between the vertical structure of the shallow heating forcing before and after taking the normal mode transforms (blue).

where  $z^* = z_B$ , and  $\mathcal{V}(z)$  is now defined as

$$\mathcal{V}(z) = \frac{1}{2} \begin{cases} 1 + \cos\left(\frac{\pi z}{z_B}\right) & 0 \leq z \leq z_B, \\ 0 & z_B \leq z \leq z_T, \end{cases} \quad (3.30)$$

After taking an inverse normal mode transform

$$\mathcal{V}(z) = \sum_{\ell=0}^{\mathcal{L}} \mathcal{V}_\ell \mathcal{Z}_\ell(z). \quad (3.31)$$

Since  $0 \geq \hat{b}_\ell < 2^{1/2}$ , from (3.21),  $\mathcal{L} = 18$  is once again the largest vertical wavenumber we can compute. The maximum error associated with  $\mathcal{L} = 18$  is  $\approx 0.9\%$  (Fig. 3.13).

We shall run a variety of experiments which include four different shapes of each forcing, and four different displacements. Each experiment will have a different individual forcing and we will analyze the effects of that particular individual forcing only. Then the relative importance of each forcing can be assessed. Since the set of equations we are solving are linearized, the corresponding solutions for each experiment can be superimposed in order to analyze the combined effects of multiple experiments. The numerical values used for the variables used in the experiments are given in Table 3.1 and the numerical values for constants are shown in Table 3.2.

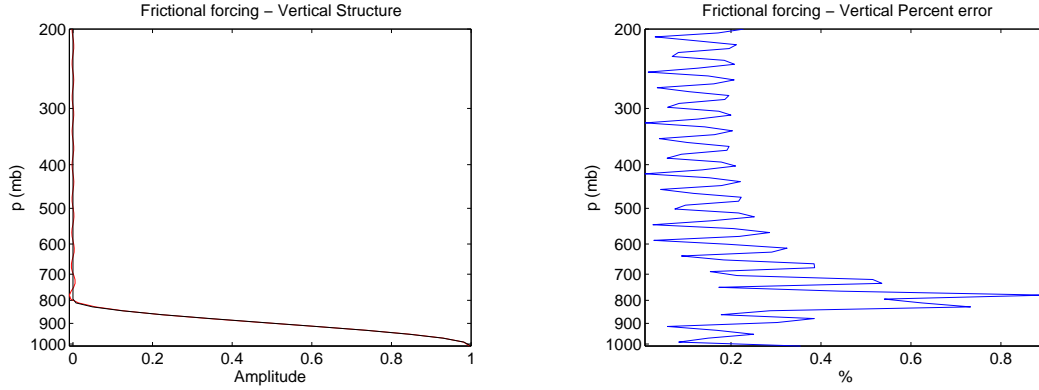


Figure 3.13: The vertical structure of the frictional forcings before taking the normal mode transform (black) and after taking the normal mode transform (red). The percent error between the vertical structure of the frictional forcings before and after taking the normal mode transforms (blue).

Table 3.1: Numerical values of variables used in the experiments.

$F_0$ [ $10^{-5} \text{m s}^{-2}$ ]	$Q_0$ [ $\text{K day}^{-1}$ ]	$a_0$ [km]	$b$ [km]	$y_d$ [km]
-3.25 or -6.5	3.75 or 7.5	1250	500	$\pm 500$
-3.25 or -6.5	3.75 or 7.5	2500	500	500
-3.25 or -6.5	3.75 or 7.5	5000	500	1000
-3.25 or -6.5	3.75 or 7.5	10000	500	1500

Table 3.2: Numerical values for constants introduced in Chapter 2.

Variable	Value [Units]	Variable	Value [Units]
$p_0$	1010 [hPa]	$a$	6371 [km]
$p_T$	200 [hPa]	$\alpha$	0.25 [ $\text{day}^{-1}$ ]
$R$	287 [ $\text{J kg}^{-1} \text{K}^{-1}$ ]	$g$	9.8 [ $\text{m s}^{-2}$ ]
$N$	$1.2 \times 10^{-2}$ [ $\text{s}^{-1}$ ]	$c_p$	1004 [ $\text{J kg}^{-1} \text{K}^{-1}$ ]
$\Omega$	$7.292 \times 10^{-5}$ [ $\text{s}^{-1}$ ]	$T_0$	300 [K]

## Chapter 4

### RESULTS

In this chapter, we take a look at the experiments outlined in Chapter 3. These experiments are insightful for understanding the dynamics near the Intertropical Convergence Zone (ITCZ). We discern why deep and shallow mean meridional circulations (MMCs) exist, why they can coexist in the ITCZ, and how the surface wind field near the ITCZ can affect the subsequent Ekman upwelling or wind stress curl. We also address the formation of the double ITCZ (DITCZ) in the East Pacific. Note that only half of the zonal domain is shown in these figures.

#### 4.1 The Annual March of the Intertropical Convergence Zone

The first set of experiments involves moving the forcing of deep diabatic heating away from the equator, in the northward direction. This acts to simulate the annual march of the ITCZ in the East Pacific Waliser and Gautier (1993), shown in Fig. 4.1. The East Pacific ITCZ tends to stay north of the equator for the entire year, with the exception of the formation of a DITCZ during March and/or April. The DITCZ period is usually characterized by relatively warmer SSTs, or a weaker “cold tongue” in between the two ITCZs, where one ITCZ is north of the equator and a second ITCZ is south of the equator. Recall that the “cold tongue” is a region of relatively cool equatorial SSTs; it intensifies as the ITCZ travels north of the equator during the year.

In Fig. 4.2 we illustrate the horizontal structure of the steady-state wind and geopotential height anomalies at the surface when the ITCZ is displaced at  $y_d = \pm 500, 500$ ,

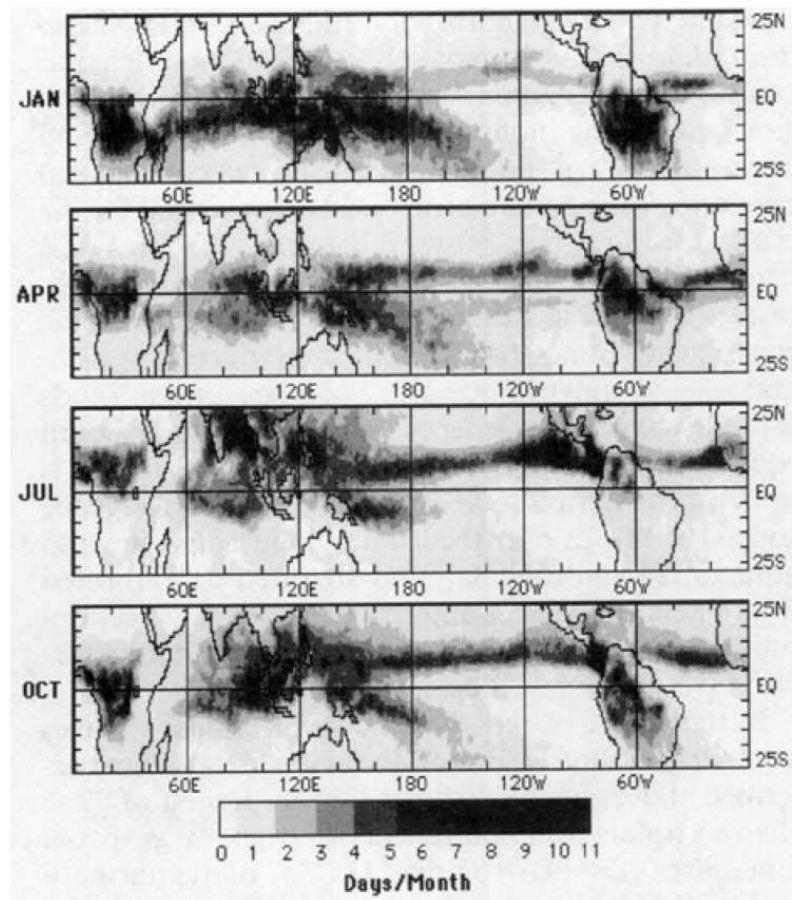


Figure 4.1: The annual march of the ITCZ over the tropical atmosphere (25°S, 25°N). The values represent the number of days per month the given grid point was “covered” by deep convection (subjectively determined) using 17 years of monthly highly reflective cloud (HRC) data. From Waliser and Gautier (1993).

1000, and 1500 km, without changing the shape of the deep heating ( $a_0 = 1250$  km and  $b = 500$  km are both constant). The most striking feature from this figure is that there are relatively weak symmetric Rossby gyres when the heating is on the equator, but as the heating is displaced north of the equator, the Rossby gyre north of the equator strengthens, dominating the horizontal wind and geopotential height anomaly fields. Since the ITCZ in the East Pacific stays north of the equator throughout the entire year, one would think that these regions will never have Rossby gyres that are symmetric about the equator, but this may not be true. It is interesting to note that the steady-state surface fields when  $y_d = \pm 500$  km, look very similar to the steady-state results when a prescribed diabatic heating is centered on the equator,  $y_d = 0$  km, shown in Fig. 4.3. When  $y_d = \pm 500$  we aim to simulate the DITCZ, prescribing a diabatic heating just to the north and south of the equator, with each heat source containing  $Q_0 = 3.75$  K day<sup>-1</sup>.

The results suggest that even though the ITCZ is never centered on the equator in the East Pacific, there still may be symmetric Rossby gyres. That is, when symmetric ITCZs are north and south of the equator. Of course, in the real world, it is rare to have both ITCZs be displaced at the same distance away from the equator and have the same diabatic heating (magnitude and shape).

The take home message from Fig. 4.2 is that the wind and geopotential height anomaly fields that are forced by a deep diabatic heating in the East Pacific are generally asymmetric in both the zonal and meridional plane, with a clear bias to the Northern Hemisphere during most of the year. The general surface features of the wind anomaly field involve cross-equatorial flow near the heating due to inertia-gravity and mixed Rossby-gravity waves, strong westerly winds west of the heating due to Rossby waves, and weaker, more homogeneous easterlies that spread far east of the heating due to Kelvin waves, and significant horizontal convergence from the inertia-gravity and Kelvin waves. The results agree very well with previous studies using linearized equatorial  $\beta$ -plane models, such as Matsuno (1966), Gill (1980), and Schubert and Masarik (2006).

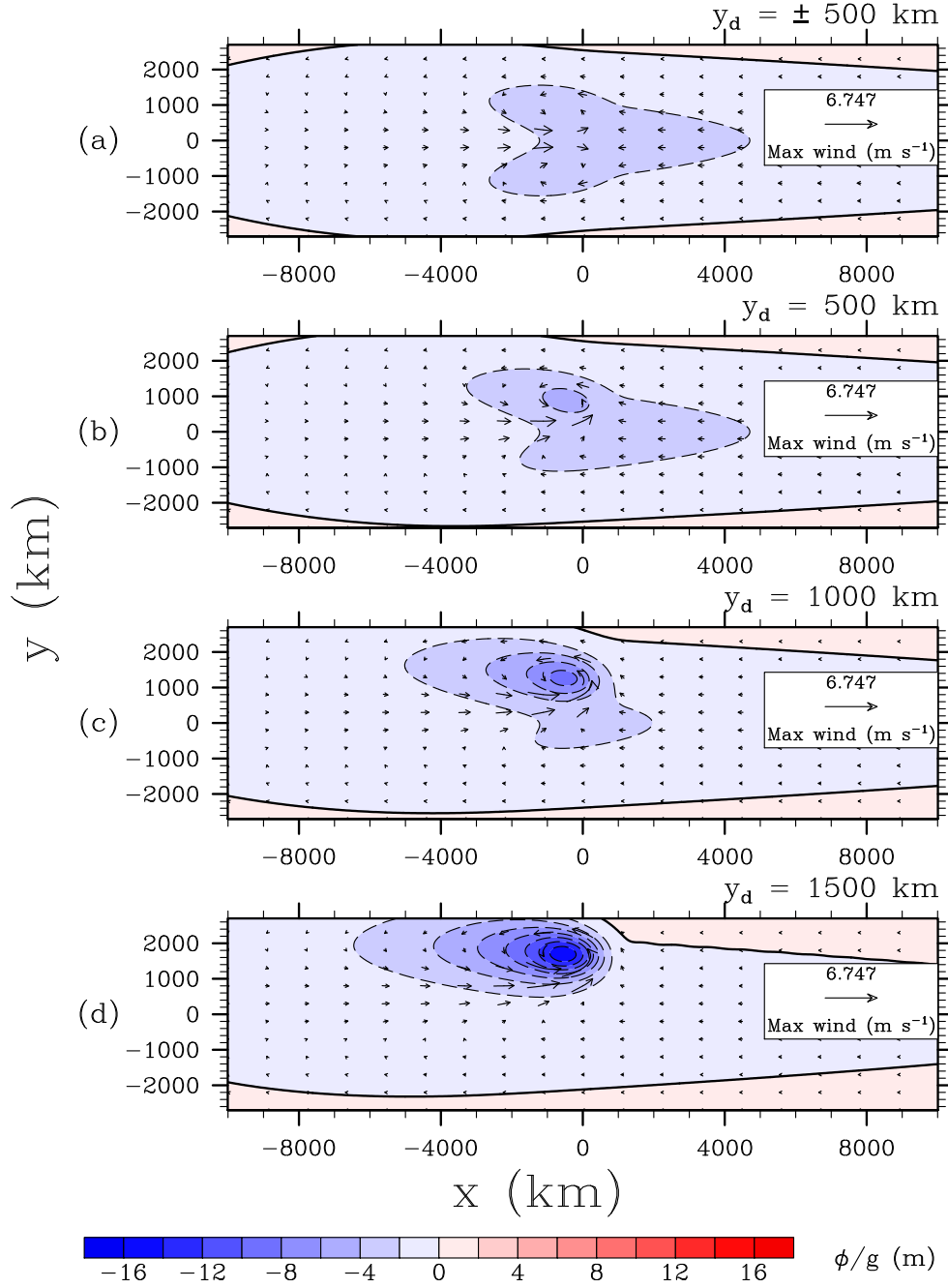


Figure 4.2: The steady-state horizontal structure forced by a deep heating profile on the  $p = 1010$  hPa pressure level of the geopotential height anomaly field (m) and the wind anomaly field ( $\text{m s}^{-1}$ ) with the same zonal half-width  $a_0 = 1250$  km and different meridional displacements:  $y_d = \pm 500, 500, 1000,$  and  $1500$  km in (a)–(d). The geopotential height field is shaded and contoured at an interval of 2 m. The solid contours represent positive values while the dashed contours represent negative values. The zero contour line is in bold. The maximum magnitude of the geopotential height is 15.457 m. The wind field is illustrated using vectors, with a maximum wind speed of  $6.747 \text{ m s}^{-1}$  (used as a reference vector).

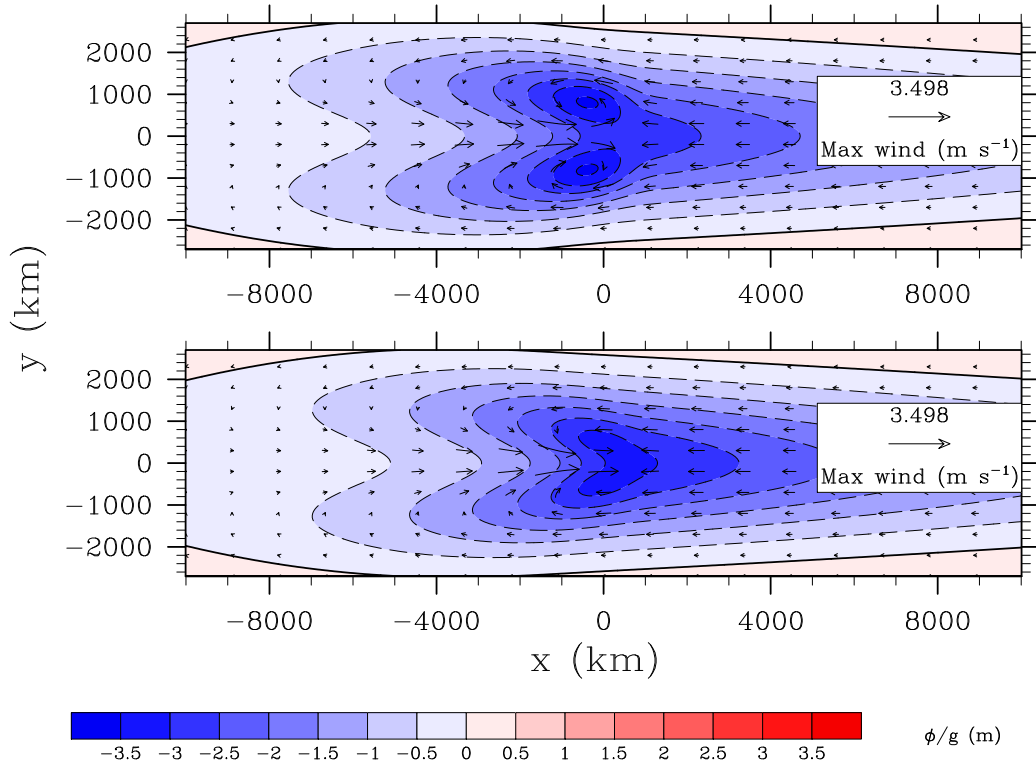


Figure 4.3: The steady-state horizontal structure forced by a deep heating profile on the  $p = 1010 \text{ hPa}$  pressure level of the geopotential height anomaly field (m) and the wind anomaly field ( $\text{m s}^{-1}$ ) with the same zonal half-width  $a_0 = 1250 \text{ km}$ , but different meridional displacements ( $y_d = \pm 500 \text{ km}$  - top,  $y_d = 0 \text{ km}$  - bottom), and different diabatic heating rates ( $Q_0 = 3.75 \text{ K day}^{-1}$  - top,  $Q_0 = 7.5 \text{ K day}^{-1}$  - bottom). The geopotential height field is shaded and contoured at an interval of  $0.5 \text{ m}$ . The solid contours represent positive values while the dashed contours represent negative values. The zero contour line is in bold. The maximum magnitude of the geopotential height anomaly is  $3.585 \text{ m}$ .

As the heating is displaced north of the equator, the westerlies west of the heating shift northward and increase in magnitude, while the easterlies east of the heating experience very minimal change, as shown in Fig. 4.4, where we have contoured the magnitude of the difference in the zonal wind anomaly. The Rossby gyre vortex strengthens due to the increase in westerlies south of the vortex center and an increase in easterlies north of the vortex center. The strong westerlies help increase the zonal wind stress and the strengthening of the Rossby gyre vortex helps increase the zonal wind stress curl.

Also, southerlies form in the heated region, and increase as the heating is displaced farther from the equator. These southerlies are located on the south and southeast side of the Rossby gyre, aiding in intensifying the vortex. These southerlies continue to shift northward as the heating is displaced northward (Fig. 4.5). In Fig. 4.5 we have contoured the magnitude of the difference in the meridional wind anomaly. The increase in southerly flow near the heating is due to the asymmetric Rossby and inertia-gravity waves and the added contribution of mixed Rossby gravity waves when the heating is displaced off the equator, both helping to enhance the cross-equatorial flow (Gill 1980; Schubert and Masarik 2006). The mixed Rossby-gravity waves have zero contribution to any of the computed fields when the atmosphere is forced solely by diabatic heating centered on the equator; their contribution increases as the heating is displaced farther away from the equator.

The Rossby gyre to the north intensifies as the diabatic heating is displaced northward given the lower geopotential heights as well as larger geopotential height gradients associated with it. This implies that the surface pressure gradients will increase, agreeing with the larger surface pressure (and SST) gradients observed in the East Pacific. The surface wind stress and wind stress curl fields also change quite a bit as the heating is shifted northward. The ITCZ naturally induces Ekman pumping due to the wind stress curl in the Rossby gyres that form, but as the heating is shifted northward, the increased vorticity from the dominant Rossby gyre also forces greater Ekman pumping out of the BL. This Ekman pumping is due mostly to the meridional gradient of the zonal wind stress, and is located

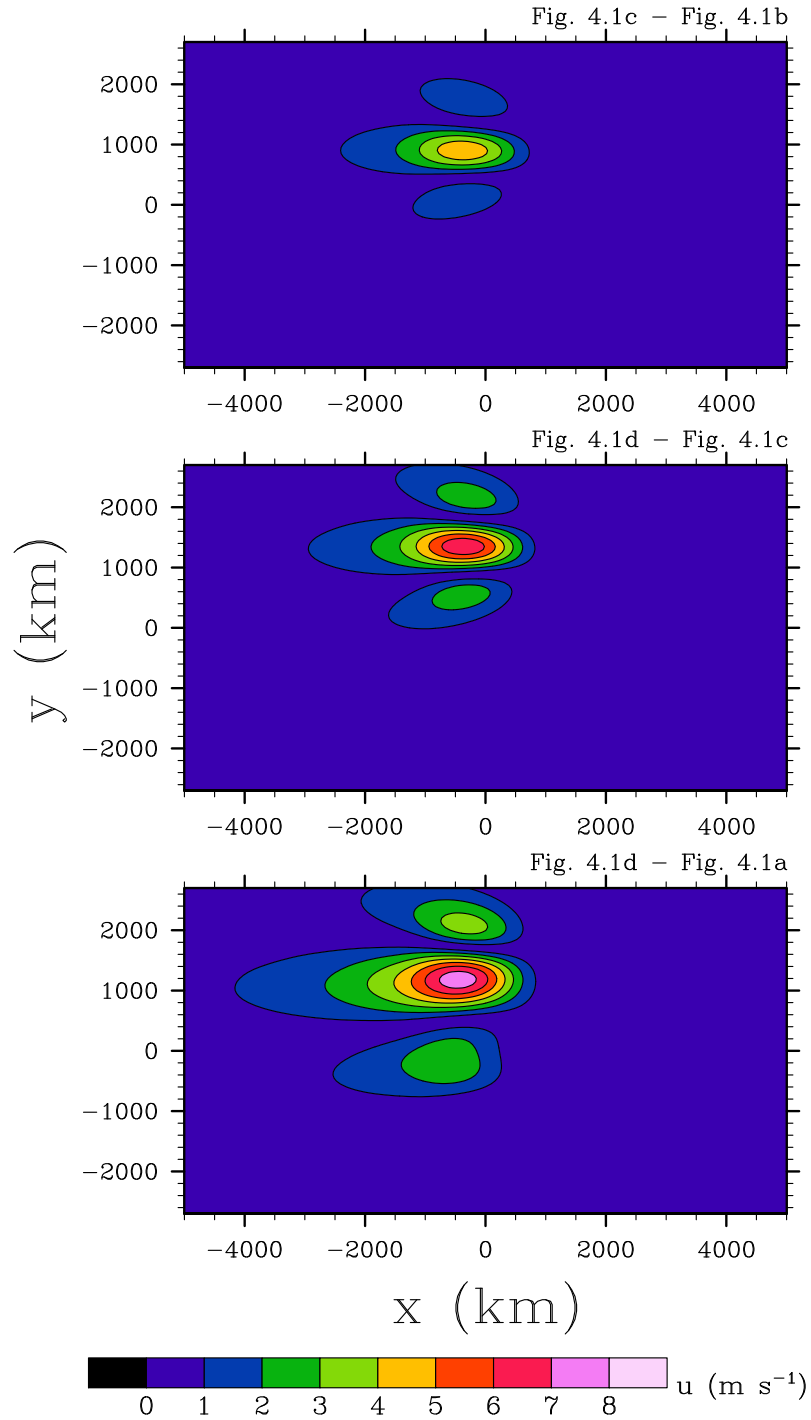


Figure 4.4: The magnitude of the difference in steady-state horizontal structure on the  $p = 1010$  hPa pressure level of the zonal wind anomaly field ( $\text{m s}^{-1}$ ) with the same zonal half-width  $a_0 = 1250$  km between different meridional displacements: Fig. 4.2c - Fig. 4.2b, Fig. 4.2d - Fig. 4.2c, and Fig. 4.2d - Fig. 4.2a (top to bottom). The zonal wind anomaly field difference is shaded and contoured at an interval of  $1 \text{ m s}^{-1}$ . The maximum difference in zonal wind is  $7.368 \text{ m s}^{-1}$ .

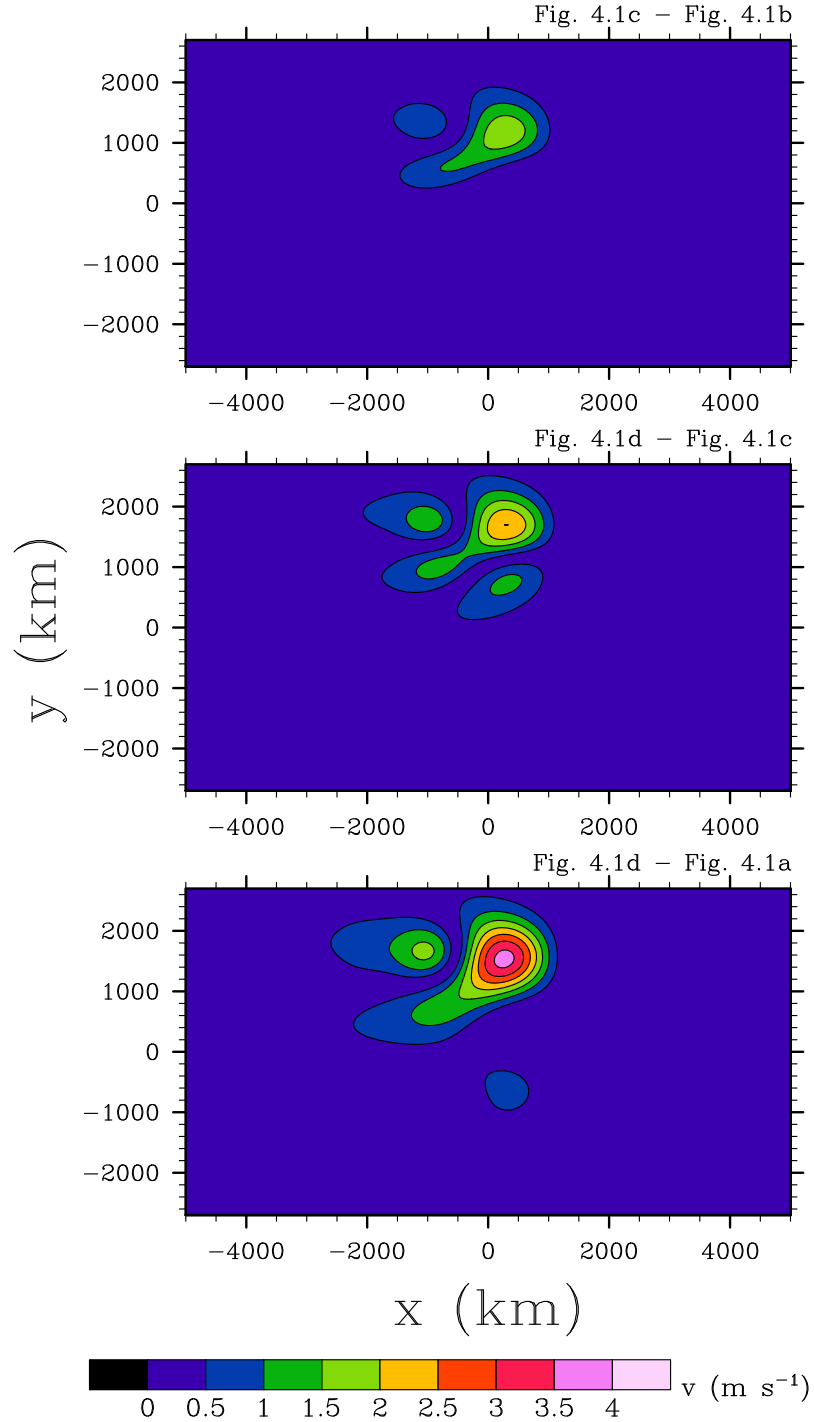


Figure 4.5: The magnitude of the difference in steady-state horizontal structure on the  $p = 1010$  hPa pressure level of the meridional wind field ( $\text{m s}^{-1}$ ) with the same zonal half-width  $a_0 = 1250$  km between different meridional displacements: Fig. 4.2c - Fig. 4.2b, Fig. 4.2d - Fig. 4.2c, and Fig. 4.2d - Fig. 4.2a (top to bottom). The meridional wind field difference is shaded and contoured at an interval of  $0.5 \text{ m s}^{-1}$ . The maximum difference in meridional wind is  $3.798 \text{ m s}^{-1}$ .

slightly north of the deep diabatic heating center. This topic will be discussed in more detail in Section 4.3.

## 4.2 The Deep Hadley and Walker Circulations

We now take a look at the steady-state solutions of the vertical-meridional and vertical-zonal cross sections when the atmosphere is forced by a deep diabatic heating. The meridional and zonal velocity anomaly and vertical-pressure velocity fields show both a deep Hadley Circulation (DHC) and a deep Walker Circulation (DWC) when the horizontal structure is least zonally-elongated ( $a_0 = 1250$  km), illustrated in Fig. 4.6 and Fig. 4.7.

There is large rising motion confined near the isolated heat source and weak and more homogeneous sinking motion away from the heating for both the DHC and DWC.

In Fig. 4.6, when the heating is centered on the equator, there are two cells both west ( $x_s = -778$  km) and east ( $x_s = +778$  km) of the heating: one of the two cells is north of the equator and the other cell is south of the equator, for both the west and east sides. Even though vertical-meridional circulation cells exist on both the west and east sides of the heating, there is significant zonal asymmetry. The west side of the heating contains strong meridional surface convergence near the center of the heating and meridional divergence aloft while the east side of the heating contains weaker meridional surface divergence and meridional convergence aloft near the center of the heating. The meridional surface convergence on the west side of the heating is due mainly to the inertia-gravity waves since the Rossby waves have a small change in meridional velocity in the meridional plane near the heating (and mixed Rossby-gravity waves have zero contribution when  $y_d = 0$  km). The meridional surface divergence on the east side of the heating is due mainly to the meridional surface divergence from the Rossby gyres that intrude eastward of the center of the diabatic heating, exceeding the surface convergence associated with the inertia-gravity waves. Recall that there are also Kelvin waves on the east side of the heating, but their component of the meridional velocity anomaly is zero in the equatorial  $\beta$ -plane, therefore they do not

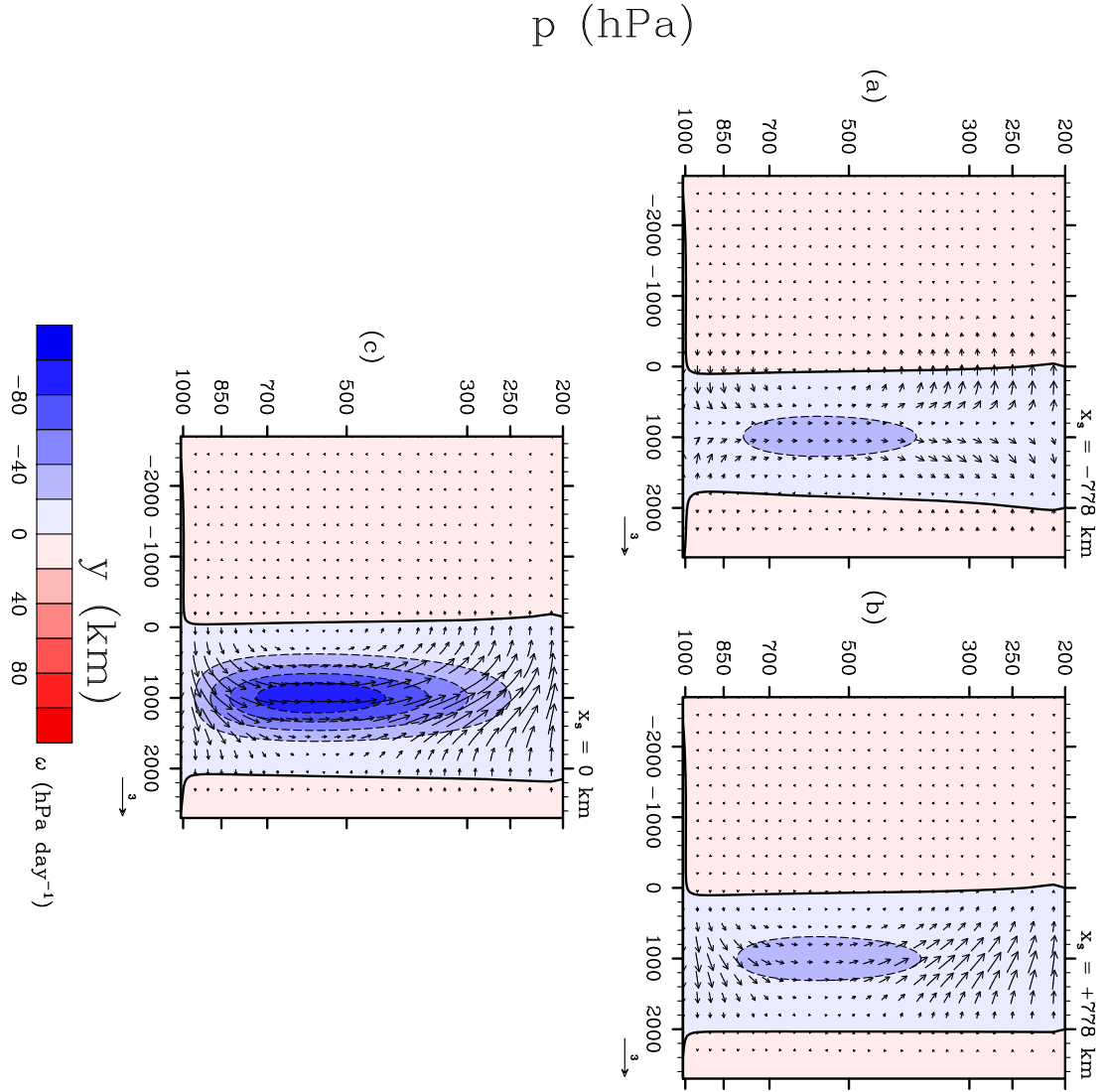


Figure 4.6: The steady-state vertical-meridional structure forced by deep diabatic heating at  $x_s = -778$  km in (a),  $x_s = +778$  km in (b), and  $x_s = 0$  km in (c) of the vertical-pressure velocity field ( $\text{hPa day}^{-1}$ ) and the wind field with the same zonal half-width  $a_0 = 1250$  km and meridional displacement  $y_d = 1000$  km. The vertical-pressure velocity field is shaded and contoured with the same contour specifications as Fig. 4.2, at an interval of  $20 \text{ hPa day}^{-1}$ . The maximum magnitude of the vertical-pressure velocity is  $97.632 \text{ hPa day}^{-1}$ . Note that in order to draw vectors of the meridional velocity anomalies and the vertical-pressure velocity we have kept the meridional velocity in  $\text{m s}^{-1}$  and converted the vertical-pressure velocity into  $\text{Pa s}^{-1}$ , multiplying by 10. Therefore the wind vector units are meaningless.

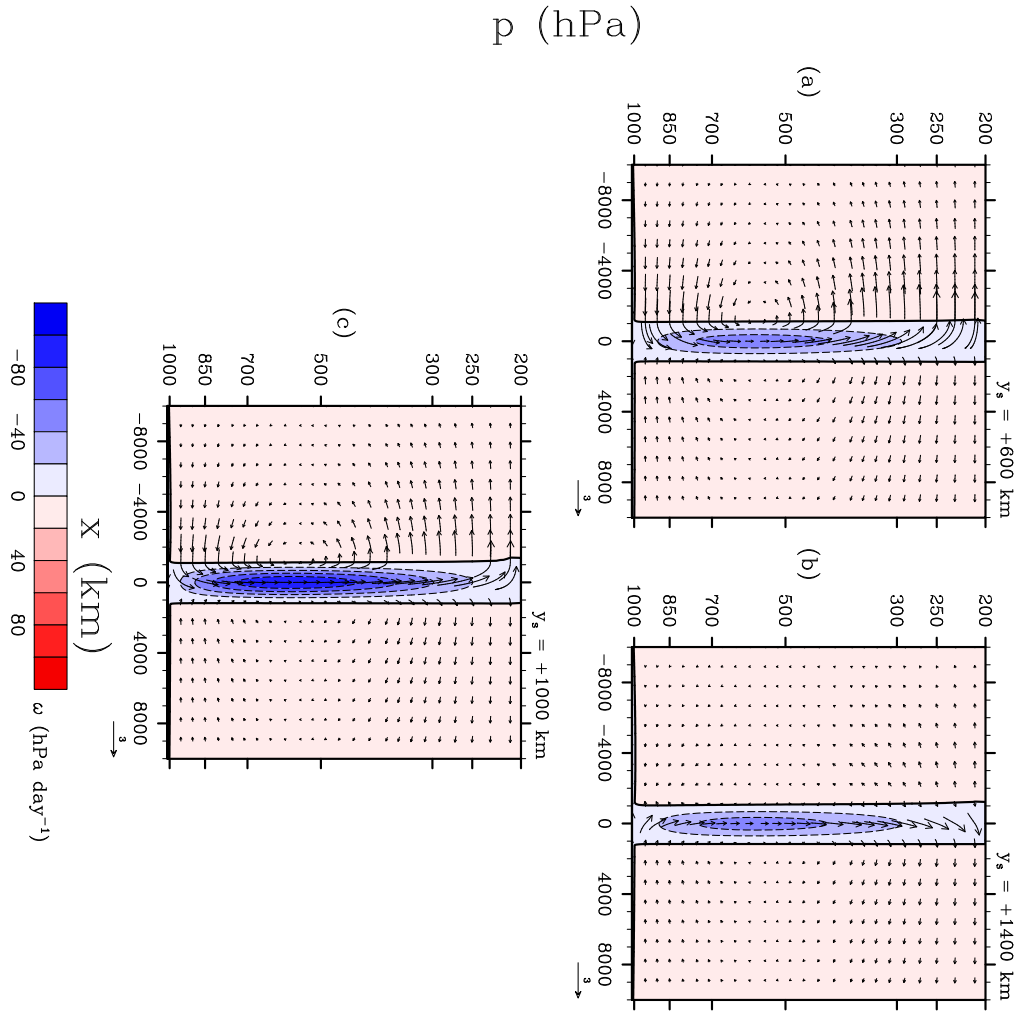


Figure 4.7: The steady-state vertical-zonal structure forced by deep diabatic heating at  $y_s = 600$  in (a),  $y_s = 1400$  km in (b,) and  $y_s = 1000$  km in (c) of the vertical-pressure velocity field ( $\text{hPa day}^{-1}$ ) and the wind field with the same zonal half-width  $a_0 = 1250$  km and meridional displacement  $y_d = 1000$  km. The vertical-pressure velocity field is shaded and contoured with the same contour specifications as Fig. 4.6. The maximum magnitude of the vertical-pressure velocity is  $97.632 \text{ hPa day}^{-1}$ . The same procedure applied in Fig. 4.6 is used for calculating wind vector magnitudes.

contribute to the meridional convergence in the DHC in our steady-state model.

The DWC is also shown to be quite asymmetric in its corresponding horizontal (zonal) plane, with larger gradients west of the heating (Fig. 4.7). The strong response on the west side of the heating is due mainly to the strong westerlies that the Rossby waves produce, as well as the zonal surface convergence of the inertia-gravity waves. The east side of the heating also has a DWC, with significant contributions from both the surface zonal flow and convergence of Kelvin and inertia-gravity waves.

As the deep heating is displaced farther north from the equator, the DHC cell that crosses the equator becomes more dominant in the meridional wind anomaly field (Fig. 4.8). The reason behind the increase in meridional wind anomalies can be explained by the asymmetric Rossby and inertia-gravity waves and the added contribution of mixed Rossby gravity waves as mentioned before. This means that the strength of the cross-equatorial deep MMC increases as the ITCZ progresses north of the equator in the East Pacific. The months of late boreal summer and early boreal fall are when the ITCZ has been observed to be the farthest away from the equator Fig. 4.2, coincidentally when the meridional surface wind component is largest.

There is negligible change to the DWC as the heating is displaced north of the equator, therefore their resulting figures will not be shown. As the zonal half width  $a_0$  increases, there is a minimal strengthening to the DHC (Fig. 4.9), but the DWC becomes zonally-confined near the heating (Fig. 4.10).

When there is a zonally symmetric heating, the Hadley circulation cell that crosses the equator dominates, which agrees with zonally-symmetric models, such as Hack et al. (1989) and Hack and Schubert (1990). Essentially, the more zonally symmetric the ITCZ region is, the more that the DHC prevails as the vertical-horizontal circulation. This does not mean that the DWC is not present, though. In fact, the zonal winds increase substantially when the heating is elongated, but the region where this occurs becomes more confined. When the heating is zonally-elongated the magnitude of the meridional winds and convergence only

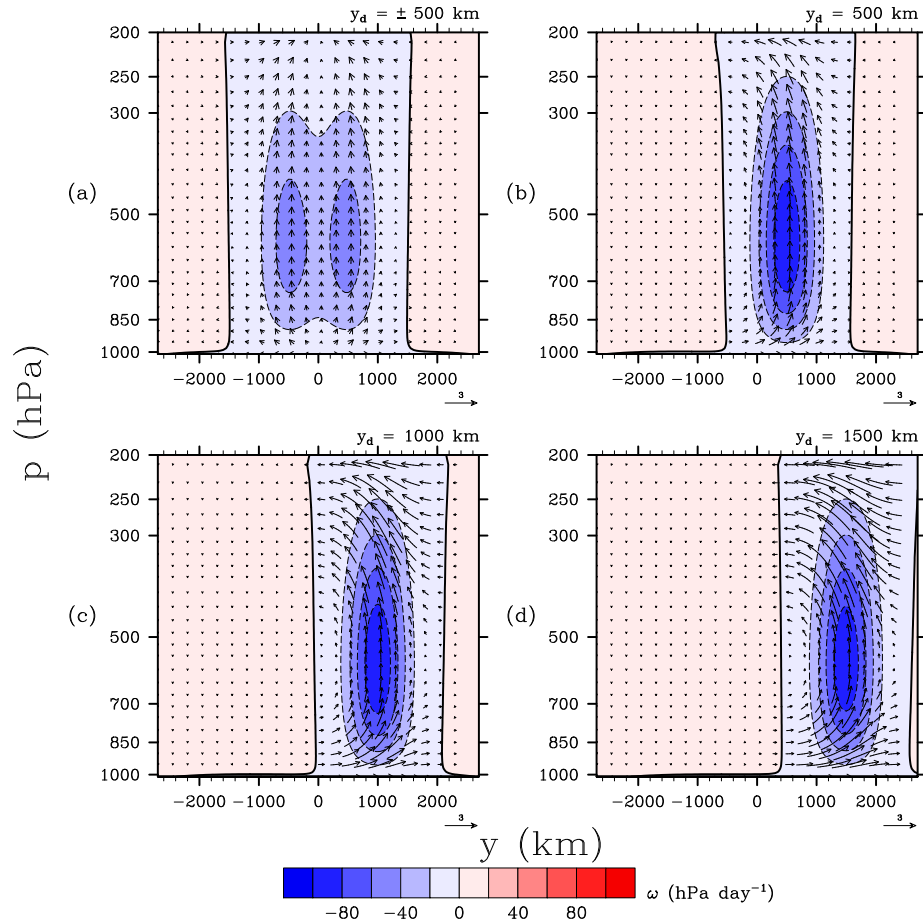


Figure 4.8: The steady-state vertical-meridional structure forced by a deep heating profile at  $x_s = 0$  km of the vertical-pressure velocity field (hPa day $^{-1}$ ) and the wind field with the same zonal half-width  $a_0 = 1250$  km at different meridional displacements:  $y_d = \pm 500$ , 500, 1000, and 1500 km in (a)–(d). The vertical-pressure velocity field is shaded and contoured with the same contour specifications as Fig. 4.6. The maximum magnitude of the vertical-pressure velocity is 97.402 hPa day $^{-1}$ . The same procedure applied in Fig. 4.6 is used for calculating wind vector magnitudes.

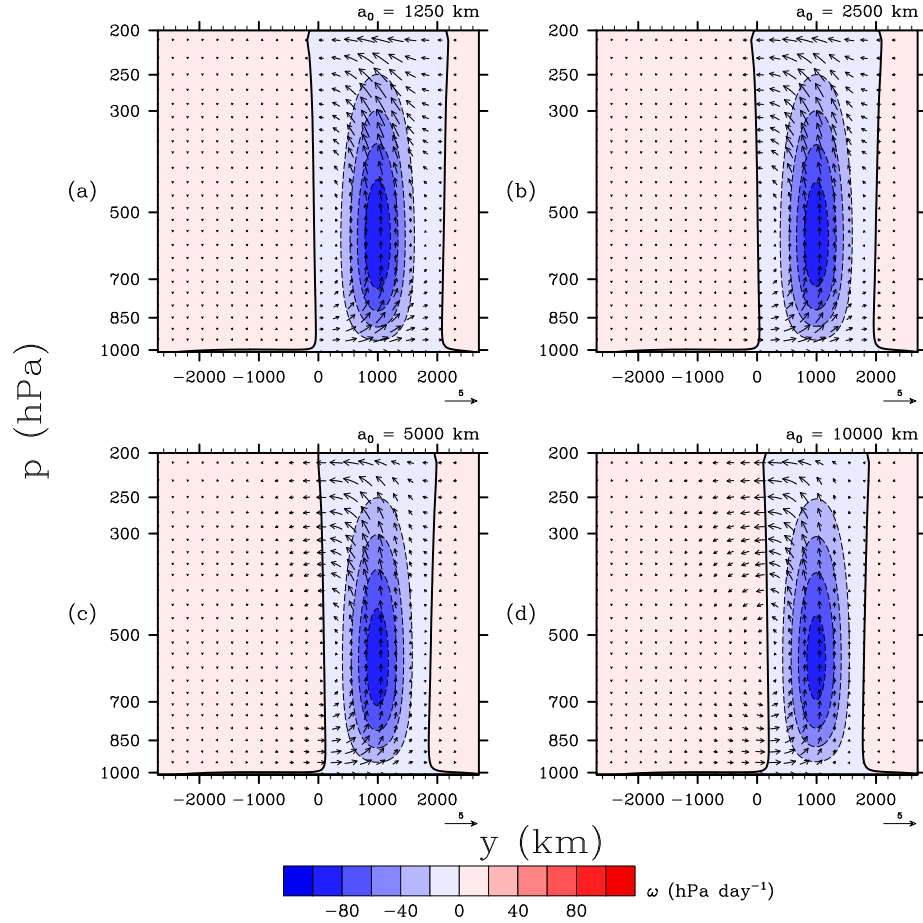


Figure 4.9: The steady-state vertical-meridional structure at  $x_s = 0$  km of the vertical-pressure velocity field ( $\text{hPa day}^{-1}$ ) and the wind anomaly field at the same meridional displacement  $y_d = 1000$  km with different zonal half-widths:  $a_0 = 1250, 2500, 5000,$  and  $10000$  km in (a)–(d). The vertical-pressure velocity field is shaded and contoured with the same contour specifications as Fig. 4.6. The maximum magnitude of the vertical-pressure velocity is  $96.638 \text{ hPa day}^{-1}$ . The same procedure applied in Fig. 4.6 is used for calculating wind anomaly vector magnitudes.

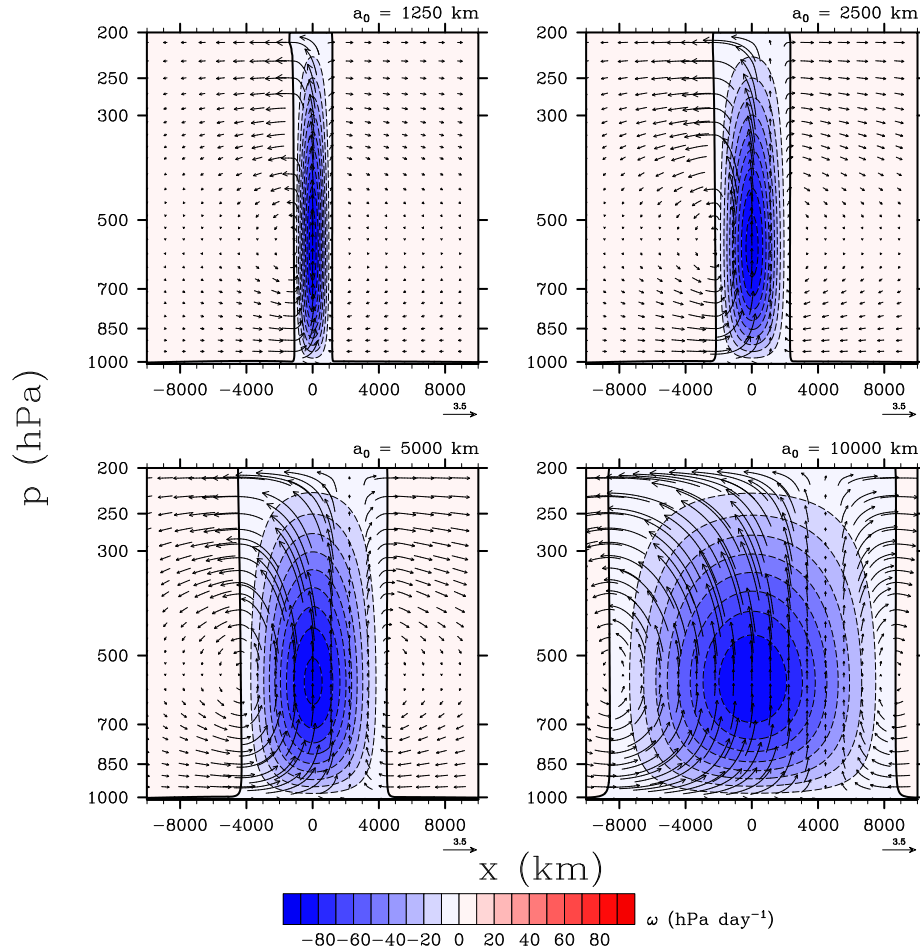


Figure 4.10: The steady-state vertical-zonal structure at  $y_s = 1000$  km of the vertical-pressure velocity field (hPa day $^{-1}$ ) and the wind anomaly field at the same meridional displacement  $y_d = 1000$  km with different zonal half-widths:  $a_0 = 1250, 2500, 5000,$  and  $10000$  km in (a)–(d). The vertical-pressure velocity field is shaded and contoured with the same contour specifications as Fig. 4.6. The maximum magnitude of the vertical-pressure velocity is  $96.638$  hPa day $^{-1}$ . The same procedure applied in Fig. 4.6 is used for calculating wind anomaly vector magnitudes.

increase slightly. The ITCZ in the East Pacific has been observed to be zonally-elongated, especially during the months when the ITCZ is located farthest from the equator (Fig. 4.1). The case where the deep heating is most zonally-elongated and farthest from the equator would then have not only the most dominant DHC, but it would have the largest values of the horizontal wind anomalies.

### 4.3 Surface Wind Stress and Ekman Layer Dynamics

When the meteorological fields are forced by a boundary layer (BL) wind stress, the horizontal structure of the wind and geopotential height fields oppose the original forcing. This result can be derived by starting with the Boussinesq form of the continuity equation

$$\frac{\partial u}{\partial x} + \frac{\partial v}{\partial y} + \frac{\partial w}{\partial z} = 0, \quad (4.1)$$

where the independent variables  $x$ ,  $y$ , and  $z$  represent the zonal, meridional, and vertical position and the dependent variables  $u$ ,  $v$ , and  $w$  represent the zonal, meridional, and vertical velocity. Integrating (4.1) from the surface  $z = 0$  to the top of the atmospheric BL  $z = H_{atm}$ , with the requirement that  $w = 0$  at  $z = 0$ , we obtain

$$\begin{aligned} w(H_{atm}) &= - \int_0^{H_{atm}} \left( \frac{\partial u_{ag}}{\partial x} + \frac{\partial v_{ag}}{\partial y} \right) dz, \\ &= - \frac{1}{\rho f} \int_0^{H_{atm}} \frac{\partial}{\partial z} \left( \frac{\partial \tau_y}{\partial x} - \frac{\partial \tau_x}{\partial y} \right) dz, \\ &= \frac{1}{\rho f} \left( \frac{\partial \tau_{y0}}{\partial x} - \frac{\partial \tau_{x0}}{\partial y} \right). \end{aligned} \quad (4.2)$$

We have used the non-divergence property of the geostrophic wind on the  $f$ -plane, the steady-state simplified version  $f$ -plane derivation of the wind stress curl, and the assumption that stress vanishes at the top of the atmospheric BL,  $H_{atm}$ . We know that the ageostrophic mass flux  $\rho_{atm} \mathbf{U}_{atm}$  is to the left of the surface wind stress in the Northern Hemisphere, according to the vector equation

$$\rho_{atm} \mathbf{U}_{atm} = \frac{1}{f} \mathbf{k} \times \boldsymbol{\tau}_0, \quad (4.3)$$

where  $\mathbf{U}_{atm} = (U_{atm}, V_{atm})$  and  $\boldsymbol{\tau}_0 = (\tau_{x0}, \tau_{y0})$ . The ITCZ region is generally a region of high positive relative vorticity, especially in the zonal direction (Fig. 4.11). Therefore, the winds just to its north are generally easterly and the winds to its south are generally westerly when the ITCZ is positioned north of the equator. This wind stress is the basic result of the Rossby wave vortex in the steady-state solutions shown earlier when the ITCZ is displaced north of the equator, therefore we prescribe this form as our wind stress frictional forcing  $F$ .

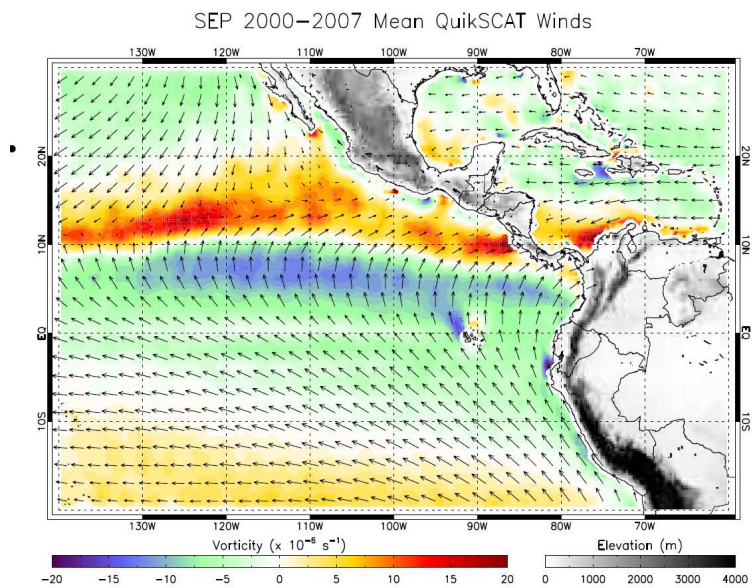


Figure 4.11: Mean winds and vorticity in the tropical East Pacific during September 2000-2007. This data was recorded using Quikscat data. From Mora (2008).

The horizontal structure of this wind stress contains a large positive wind stress curl at its center, leading to Ekman layer convergence in the atmospheric BL, and by mass continuity, an Ekman pumping out of the atmospheric BL. The Ekman pumping has important effects in and above the atmospheric BL. Ekman pumping compresses the fluid columns above the BL, in turn generating anticyclonic vorticity, higher pressure (geopotential heights), and lower temperatures in a presently cyclonic, low pressure, and high temperature region. The dynamical characteristics associated with this are often referred to as spin down. Regions of Ekman suction also experience spin down effects since Ekman suction produces a stretching of fluid columns above the BL, generating cyclonic vorticity in a presently anticyclonic region.

Recall that the exact form of the frictional forcing,  $F$ , is defined by a strong positive wind stress curl at the center of the forcing, with weaker areas of negative wind stress curl to its north and south at the surface due to the decay of the zonal wind stress fields. This setup has another important consideration when the frictional forcing is centered on or near the equator. When the frictional forcing is centered on the equator, there is a region of counterclockwise motion centered on the equator. This vortex is not only a cyclonic region; it is cyclonic north of the equator, and anticyclonic south of the equator. A region where the wind stress is easterly north of the equator and westerly south of the equator that decays in the meridional direction leads to cyclonic wind stress curl south of the equator and anticyclonic wind stress curl north of the equator (i.e., when  $y_d = 0$  km,  $a_0 = 1250$  km). This result is not shown or discussed in much detail since the ITCZ has not been observed on the equator in the East Pacific, but the ITCZ can be centered on the equator in other ocean basins.

Instead, we show the case where the wind stress forcing is due to a diabatic heating north and south of the equator; the time of the year when a DITCZ is observed in the East Pacific. When there is diabatic heating north and south of the equator there is one region of high positive wind stress curl to the north of the equator and one to the south of the equator,

(i.e., we must take the sum of the cases where  $y_d = -500$  km and  $y_d = +500$  km). When  $a_0 = 1250$  km, the surface wind field responds with positive vorticity near the equator, with a local minimum on the equator. There is also weaker negative vorticity poleward of the regions of positive vorticity at the surface (Fig. 4.12, top panel). The geopotential height field anomaly responds to the frictional forcing with positive geopotential height anomalies where there is negative vorticity, and negative geopotential height anomalies where there is positive vorticity. This confirms that a wind stress curl acts against the mean wind and geopotential height fields, which should lead to spin down in both the Ekman pumping and Ekman suction regions. These are spin down effects. The fact that the atmospheric response opposes this wind stress forcing makes sense since the wind stress is related to surface friction, which opposes the original flow field.

It is interesting to note that most of the atmospheric response is on the west side of the forcing and that the response is symmetric, but opposite in magnitude in the meridional direction when  $y_d = \pm 500$  km. We can show that the response on the west side is due mostly to the Rossby waves by illustrating the contributions from each equatorial wave type, shown in Fig. 4.13. In this figure we display the steady-state solution when the atmosphere is forced by the frictional forcing  $F$  when  $y_d = 1500$  km and  $a_0 = 1250$  km for all of the waves, and for each individual wave component - Rossby, inertia-gravity, mixed Rossby-gravity, and Kelvin waves. We confirm that the contribution of the Rossby waves dominates the horizontal surface fields, mostly because the prescribed frictional forcing consists of high vorticity wind stress.

When the frictional forcing is displaced slightly north of the equator ( $y_d = 500$  km,  $a_0 = 1250$  km), we notice that positive geopotential height anomalies form just south of the equator on the west side of the forcing, making the response more asymmetric in the meridional direction than when  $y_d = \pm 500$  km. This is due to the fact that the frictional forcing imposes a cyclonic wind stress curl south of the equator as the zonal wind stress changes sign. The east side of the forcing contains a larger region of weak positive

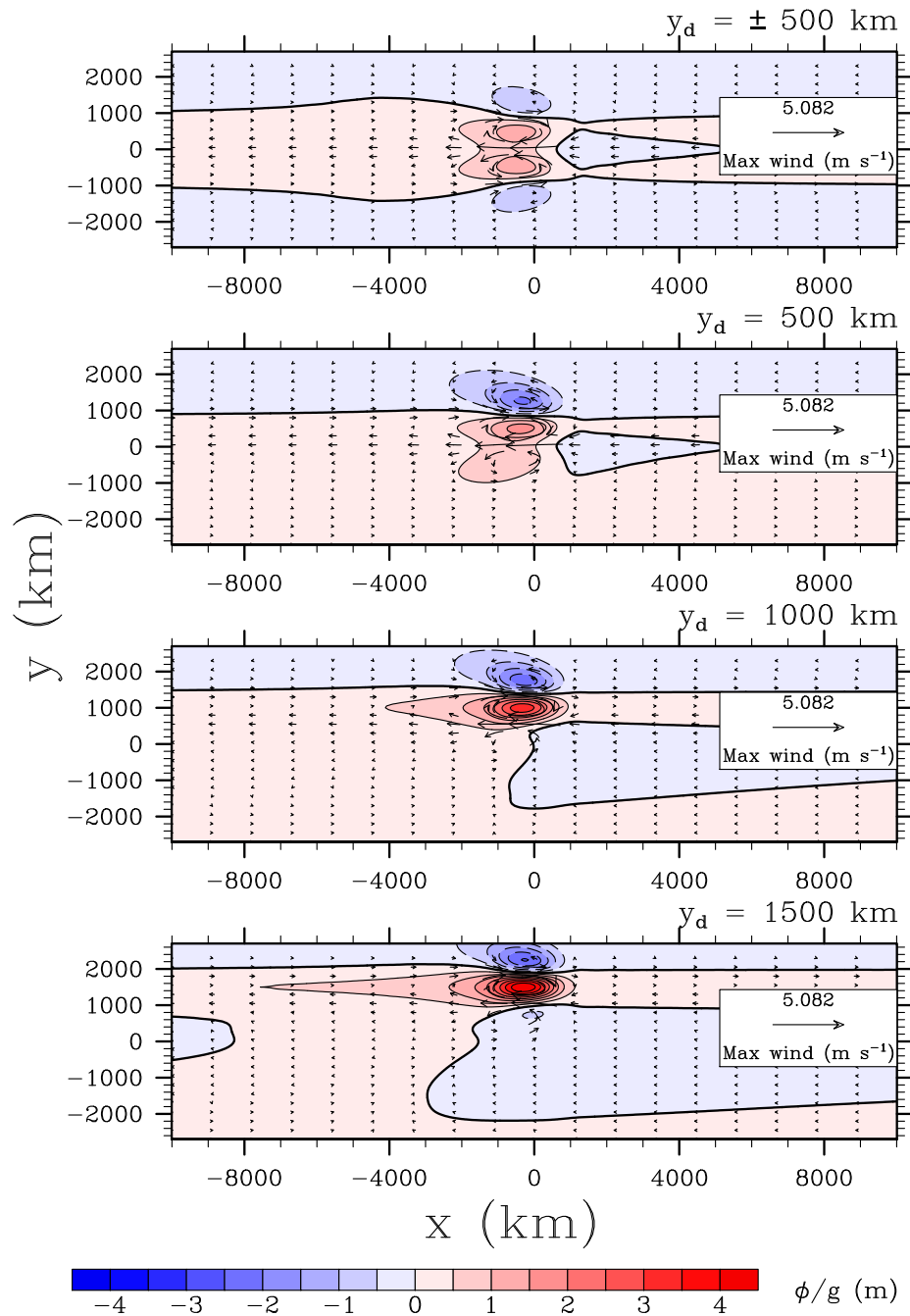


Figure 4.12: The steady-state horizontal structure forced by a wind stress curl on the  $p = 1010$  hPa pressure level of the geopotential height anomaly field (m) and the wind anomaly field ( $\text{m s}^{-1}$ ) with the same zonal half-width  $a_0 = 1250$  km and different meridional displacements:  $y_d = 0, 500, 1000,$  and  $1500$  km (top to bottom). The geopotential height field is shaded and contoured with the same contour specifications as Fig. 4.2, at an interval of  $0.5$  m. The maximum magnitude of the geopotential height anomaly is  $4.49$  m.

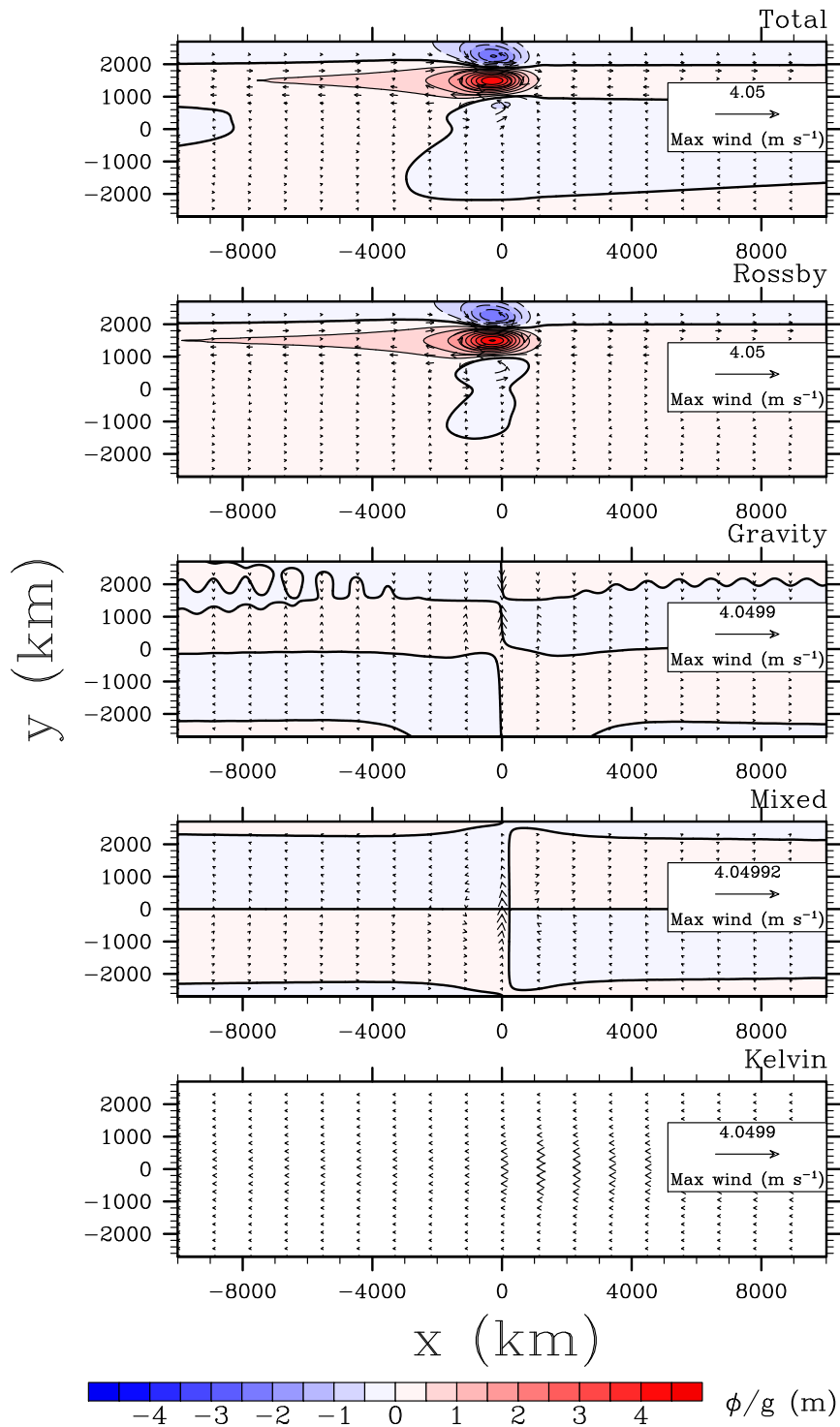


Figure 4.13: The same as Fig. 4.12, with the corresponding contributions by Rossby waves, inertia-gravity waves, mixed Rossby-gravity waves, and Kelvin waves in the bottom four panels. The maximum magnitude of the geopotential height anomaly is 4.54 m.

geopotential height anomalies, mostly south of the equator.

For the cases when the frictional forcing is centered sufficiently north of the equator ( $y_d = 1000$  and  $1500$  km,  $a_0 = 1250$  km), the surface wind field responds with strong negative vorticity at the center of the frictional forcing and weaker positive vorticity to the north and south at the surface (Fig. 4.12, bottom panels). The geopotential height field responds to the frictional forcing with large positive geopotential height anomalies where there is strong negative vorticity, and weaker negative geopotential height anomalies to the north and south of the high geopotential height region. The area south of the main Ekman pumping region has weaker geopotential height anomalies than the region north of the Ekman pumping, but it is more zonally asymmetric, with most of the response in and east of the forcing. As we will discuss in more detail in the next section, this asymmetry between the Ekman suction regions is due to the concept of Rossby length. The Rossby length is larger near the Ekman, enhancing horizontal flow fields.

#### 4.4 Shallow Circulations Forced by Ekman Pumping

The region where there is positive wind stress curl forces rising motion, or Ekman pumping, while the regions of weaker negative wind stress curl just north and south of the Ekman pumping consist of weaker sinking motion, referred to as Ekman suction. Even though the negative wind stress curl to the north and the south extend over the same horizontal distance, the Ekman suction to the north has a larger magnitude and is more horizontally confined, while the Ekman suction to the south has a smaller magnitude, and is broader in the meridional direction, crossing the equator.

In Fig. 4.14a and Fig. 4.14b, we illustrate the vertical-meridional cross section with a meridional slice on the west and east side of the center of the forcing, at  $x_s = \pm 278$  km, when  $y_d = 1000$  km,  $a_0 = 1250$  km.

The location of the meridional slice is where the maximum rising motion occurs, which happens to be on the west side of the forcing. Just like the case where the deep diabatic

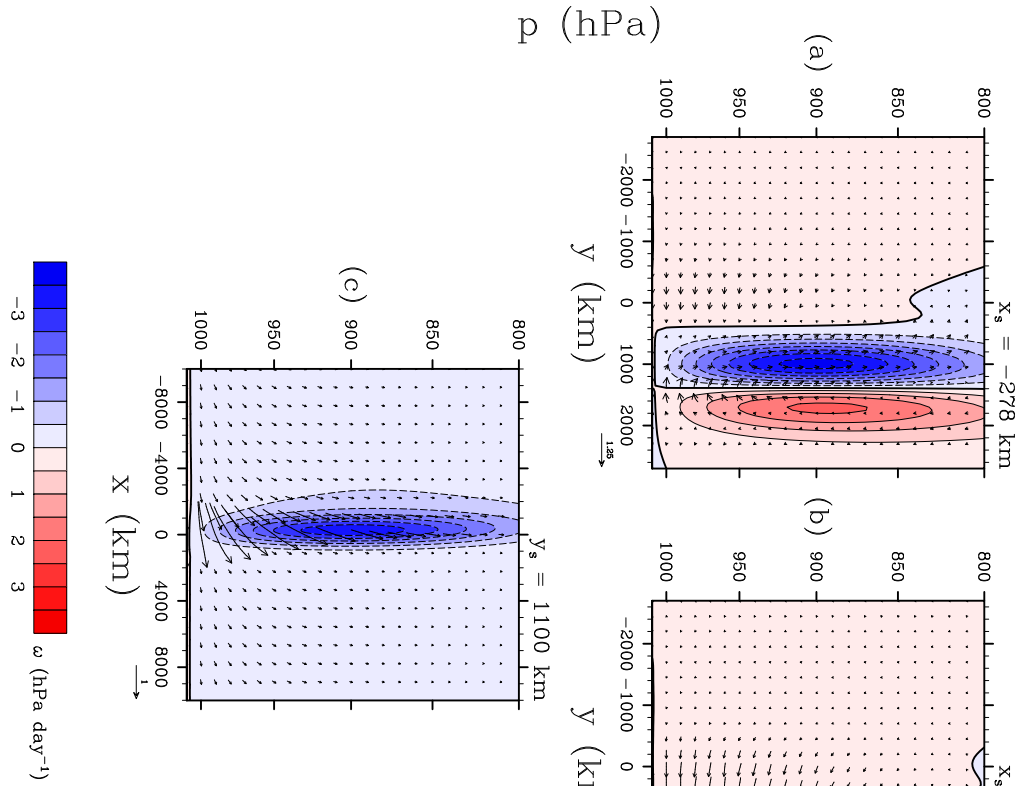


Figure 4.14: The steady-state vertical-meridional structure forced by a wind stress curl when taking a meridional slice at  $x_s = \pm 278$  km in (a) and (b) of the vertical-pressure velocity field ( $\text{hPa day}^{-1}$ ) and the wind field with the same zonal half-width  $a_0 = 1250$  km and meridional displacement  $y_d = 1100$  km (c). The vertical-pressure velocity field is shaded and contoured with the same contour specifications as Fig. 4.6, at an interval of  $0.5 \text{ hPa day}^{-1}$ . The maximum magnitude of the vertical-pressure velocity is  $3.731 \text{ hPa day}^{-1}$ . The same procedure applied in Fig. 4.6 is used for calculating wind vector magnitudes.

heating was our forcing, there is significant zonal asymmetry in the vertical-meridional cross section. Both sides have rising motion due to the contribution of inertia-gravity waves, but the east side contains intruding Rossby waves that take away from the surface convergence.

The Ekman pumping/suction theoretical arguments happen to blow up at the equator since  $f = \beta y = 0$ , so it is unclear what would happen to a source of Ekman suction near the equator. Although, we know that the inertial stability is very small near the equator. The inertial stability is included in a parameter called Rossby length ( $L_\ell = \left(\frac{A}{C}\right)^{1/2}$ , where  $A$  is the static stability,  $C$  is the inertial stability). The Rossby length increases and the Rossby depth decreases as one approaches the equator. This means that parcels in the Ekman suction region that crosses the equator are more likely to have relatively smaller sinking motion and larger horizontal winds while parcels in the Ekman suction region to the north are more likely to have relatively larger sinking motion and smaller horizontal winds, as illustrated in Fig. 4.14a and Fig. 4.14b. Therefore, we have confirmed that there are two SMCs, one shallower and broader SMC that crosses the equator, and the other deeper and narrower poleward of the ITCZ.

We now would like to investigate the possibility of a shallower vertical-zonal circulation. The left panel of Fig. 4.14c shows the vertical-zonal cross section, where  $y_s = 1100$  km,  $a_0 = 1250$  km. There are significant zonal winds at the surface and vertical motion in the BL near the frictional source, but no return flow. Therefore there is no shallow overturning circulation in the zonal direction due to our frictional forcing  $F$ . One of the main reasons why we tested this is because past studies, such as Trenberth et al. (2000) and Wu (2003), have shown that a shallow "Walker-like" circulation is possible in the vicinity of the ITCZ.

Despite the rising and sinking motion that the frictional forcing produces in the vertical direction, neither the meridional or zonal winds are large enough to produce any significant vertical-meridional or vertical-zonal MMCs when the frictional forcing is least zonally-elongated ( $a_0 = 1250$  km).

The frictional forcing must be sufficiently elongated in the zonal direction to notice

signs of a shallow vertical-meridional overturning circulation. There are some signs of this shallow vertical-meridional circulation when  $y_d = 1500$  km,  $a_0 = 2500$  km, but it becomes much more apparent when  $a_0 = 5000, 10000$  km (Fig. 4.15). As the frictional forcing is

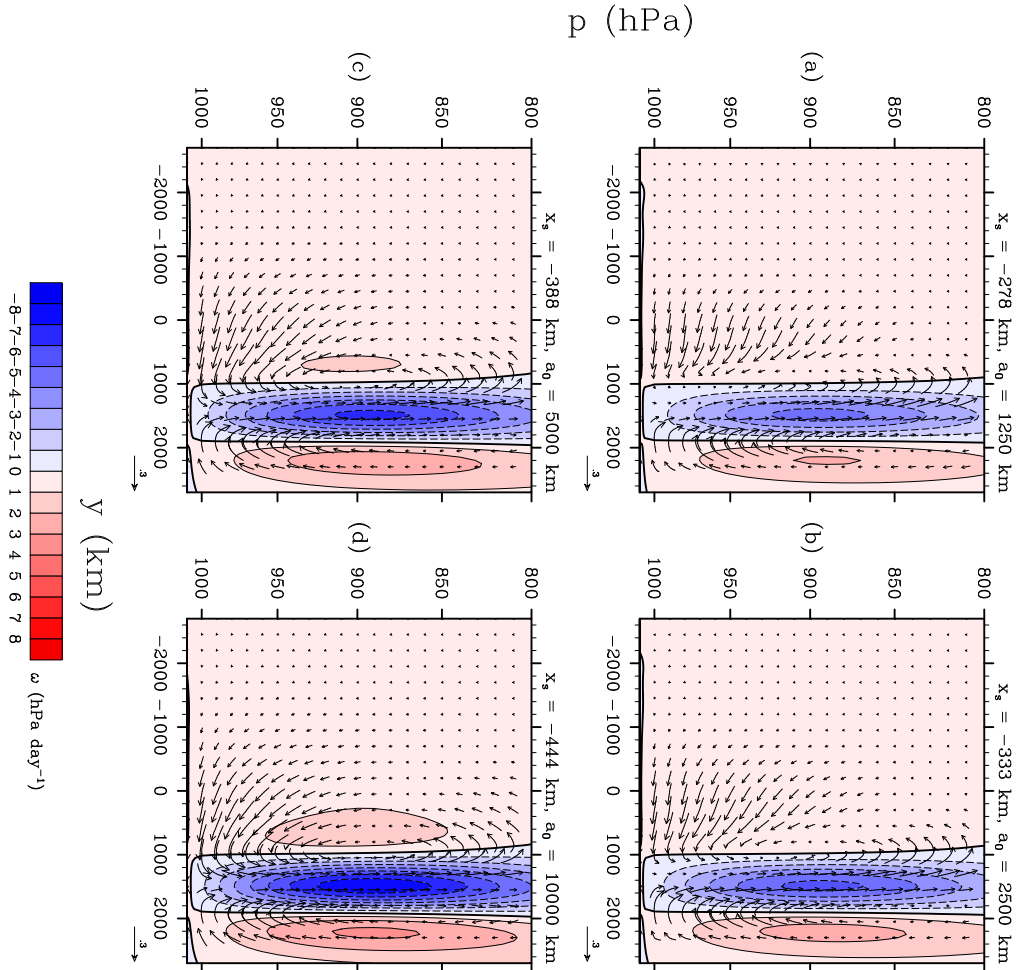


Figure 4.15: The steady-state vertical-meridional structure forced by a wind stress curl when taking a meridional slice at  $x_s = -278, -333, -388,$  and  $-444$  km of the vertical-pressure velocity field ( $\text{hPa day}^{-1}$ ) at the same meridional displacement:  $y_d = 1500$  km, and the wind field with the different zonal half-widths  $a_0 = 1250, 2500, 5000,$  and  $10000$  km in (a)–(d). The vertical-pressure velocity field is shaded and contoured with the same contour specifications as Fig. 4.2, at an interval of  $1 \text{ hPa day}^{-1}$ . The maximum magnitude of the vertical-pressure velocity is  $7.788 \text{ hPa day}^{-1}$ . The same procedure applied in Fig. 4.6 is used for calculating wind vector magnitudes.

zonally stretched, the convergence is forced to increase in the meridional direction (and decrease in the zonal direction), leading to larger meridional convergence at the surface and divergence at the top of the BL. By the laws of mass continuity, as this Shallow Meridional

Circulation (SMC) intensifies, so do the Ekman pumping, Ekman suction, and meridional divergence at the top of the BL. Still, the vertical motion induced by the frictional forcing is about 10 times smaller than the vertical motion induced by the deep diabatic heating. Also, the meridional winds are quite weak, being on the order of  $1 \text{ m s}^{-1}$  when  $a_0 = 10000$  km. The weaker meridional winds are due mainly to the fact that we are working with a three-dimensional model, and we have prescribed a zonal wind stress forcing that prefers a response in the zonal wind over the meridional winds. For a zonally symmetric model, we will have larger meridional winds than in our current model. As for the vertical motion, the rising motion associated with Ekman pumping, even though small compared to deep diabatic heating, is still relevant if we think of deep heating in the ITCZ to be variable on the order of a few days. The ITCZ breaks down, then it forms easterly waves and possibly tropical cyclones, and finally reforms on the order of days (Hack et al., 1989). Therefore there are days where the deep heating profile is nonexistent in the ITCZ, but the wind stress curl remains positive and zonally-elongated in the ITCZ. Therefore, this SMC associated with wind stress curl is always present.

It is interesting to note that there are SMCs both north and the south of the center of the positive wind stress curl that develop, with the SMC to the north containing relatively larger and deeper sinking motion and being more meridionally confined while the SMC to the south (cross-equatorial) consists of relatively smaller and shallower sinking motion and is more elongated in the meridional direction, crossing the equator. This owes to the concepts of Rossby length and Rossby depth that were mentioned before.

The vertical cross section on the west side of the center of the frictional forcing exhibits the most robust SMC, while the SMC at the center and on the east side of the frictional forcing show a weaker SMC. This is due mainly to the properties of Rossby waves that the frictional forcing projects onto. Rossby waves are dominated by their vorticity properties, which can be related to Ekman pumping and Ekman suction through wind stress curl. Kelvin waves have smaller vorticity and more divergent properties, leading to

weaker wind stress curl as seen in smaller values of the vertical pressure velocity. Also, all of the meteorological fields on the east side of the frictional forcing have much weaker response, as seen in the horizontal slices shown in (Fig. 4.12).

In the case where there are two localized regions both with positive wind stress curl north and south of the equator (i.e., when there is a DITCZ present), there are two shallow MMCs, one north of the equator and the other south of the equator (Fig. 4.16). The Ekman pumping occurs near the equator, while the Ekman suction is poleward of the Ekman pumping. There is a relative minimum in vertical motion on the equator due to the westerly wind stress that the frictional forcing imposes. As mentioned before, the frictional forcings north and south of the equator must be sufficiently elongated for the meridional wind anomalies to reverse direction at the top of the atmospheric BL.

When the frictional forcing is centered near the equator ( $y_d = 500$  km), the wind stress field that forces the atmospheric fields does not correspond to only positive wind stress curl north of the equator and weaker negative wind stress curl away from the positive wind stress curl (as discussed in last section). Instead, the wind stress field also produces positive wind stress curl on and just south of the equator since the wind stress south of the equator becomes more westerly as one approaches the equator from the south (cyclonic wind stress curl). This atmospheric situation occurs in the East Pacific region in boreal winter, as the cold tongue weakens. As the ITCZ approaches the equator a DITCZ does appear in the East Pacific. For a deep heating centered on the equator, it turns out that the surface winds and geopotential are similar to the case when there is a deep heating just to the north and south of the equator, or a DITCZ. It is interesting to note that a DITCZ sometimes forms during this time of the year when the cold tongue is the weakest. As deep convection in the ITCZ marches equatorward ( $y_d = 1500 \rightarrow 500$  km), the wind stress field forces a small remote response south of the equator in the form of shallow rising motion due to Ekman pumping. Whether this weak shallow rising motion can influence the buildup of convection south of the equator helping form a DITCZ needs to be investigated further.

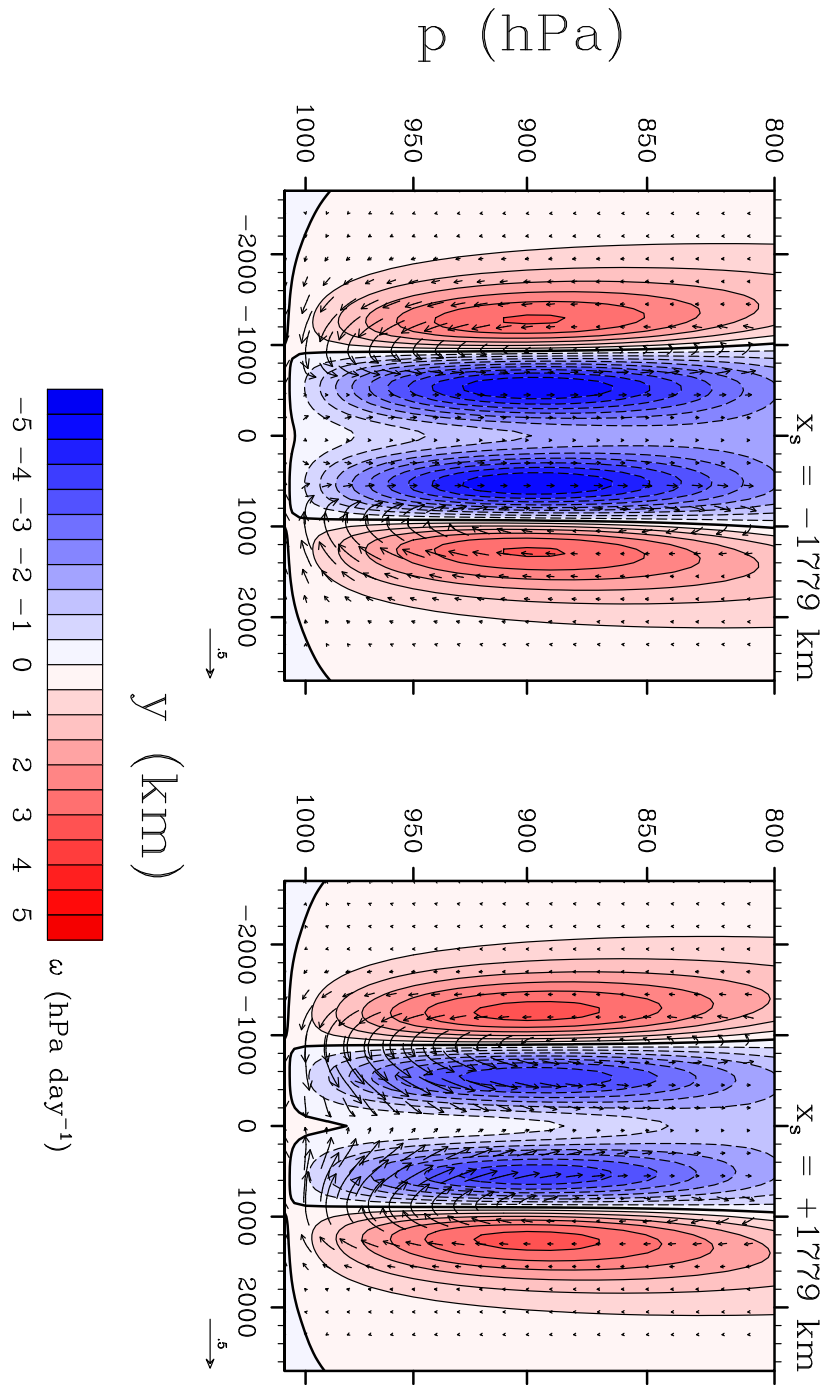


Figure 4.16: The steady-state vertical-meridional structure forced by a wind stress curl when taking a meridional slice at  $x_s = \pm 1779$  km of the vertical-pressure velocity field (hPa day<sup>-1</sup>) and the wind field with the same zonal half-width  $a_0 = 10000$  km at  $y_d = \pm 500$  km. The vertical-pressure velocity field is shaded and contoured with the same contour specifications as Fig. 4.2, at an interval of 0.5 hPa day<sup>-1</sup>. The maximum magnitude of the vertical-pressure velocity is 4.998 hPa day<sup>-1</sup>. The same procedure applied in Fig. 4.6 is used for calculating wind vector magnitudes.

## Chapter 5

### CONCLUSIONS

We have formulated a simple linear model that can be solved analytically in order to better understand deep and shallow circulations, and the dynamics near the Intertropical Convergence Zone (ITCZ) on the equatorial  $\beta$ -plane. The model can be forced by either deep diabatic heating, shallow diabatic non-precipitating heating, a zonal frictional wind stress field, or a meridional frictional wind stress field. We aimed to simulate the ITCZ region of the East Pacific because this region has been observed to have both shallow and deep vertical-horizontal circulations and convection, and a distinct ITCZ annual march. The ITCZ remains north of the equator throughout the entire year, except when a double ITCZ (DITCZ) that forms during the months of March and/or April.

When the diabatic heating forces the atmosphere the steady-state solutions at the surface are as follows:

- 1) There are negative geopotential height anomalies in the majority of the domain, especially near the center of the heating;
- 2) Rossby waves are located near and to the west of the heating, with large positive vorticity, large negative geopotential heights, and strong westerly wind anomalies;
- 3) Kelvin waves are located near and to the east of the heating, with zonal convergence and negative geopotential height anomalies;
- 4) Inertia-gravity waves and mixed Rossby-gravity waves are located near the heating center. Inertia-gravity waves contain large horizontal convergence and mixed Rossby-gravity waves have large meridional wind anomalies when the heating is displaced off the equator.

As the heating is displaced north of the equator (from  $y_d = \pm 500$  km to  $y_d = 500, 1000, 1500$  km), the Rossby gyre north of the equator intensifies by increasing its vorticity and by becoming more negative in the geopotential height anomaly field. All of the waves intensify in the northern hemisphere. The east side of the heating experiences minor changes when compared to the west side of the heating. Accompanied with these changes, the zonal and meridional wind anomaly fields change dramatically. The westerlies associated with the Rossby waves in the gyre north of the equator increase by over  $7 \text{ m s}^{-1}$ , and the meridional winds south and southeast of the heating center increase by over  $3.5 \text{ m s}^{-1}$ . The enhancement of the westerlies can be mainly attributed to the intensification of the Rossby gyre, while the increases in the meridional wind anomalies are mainly due to the increased contribution of mixed Rossby-gravity waves and asymmetric inertia-gravity waves.

When analyzing the vertical-horizontal structure when the atmosphere is forced by deep diabatic heating we find that both the deep Hadley (DHC) and deep Walker circulations (DWC) are present. There is a clear horizontal asymmetry for both the DHC and DWC, as expected when taking the asymmetry in the surface horizontal structure into consideration.

The vertical-meridional cross sections show that most of the rising motion is confined near the center of the heating with large meridional motions. The west side of the heating contains strong meridional surface convergence near the center of the heating and meridional divergence aloft while the east side of the heating contains weaker meridional surface divergence and meridional convergence aloft near the center of the heating. When there is a zonally symmetric heating, the Hadley circulation cell that crosses the equator dominates, which agrees with zonally-symmetric models, such as Hack et al. (1989), Hack and Schubert (1990).

The vertical-zonal cross sections also show that most of the rising motion is confined near the center of the heating with two circulation cells on both the west and east sides

of the heating. The circulation cell on the west side of the heating has larger zonal wind anomalies than the east side, which makes sense since this side contains enhanced surface westerlies. Just south of the heating there are also two circulation cells, one on the west side and the other on the east side of the heating. To the north of the heating, there is weaker horizontal motion, with only the east side of the heating containing a circulation cell.

As the heating is displaced farther away from the equator, the meridional wind anomalies increase, along with the increasing contribution of the mixed Rossby-gravity waves. When the heating is elongated in the zonal direction, the DWC weakens and the DHC strengthens as the horizontal convergence increases, especially in the meridional direction. The ITCZ in the real atmosphere is elongated in the zonal direction, therefore the DHC has a vital role in the general circulation.

The surface wind field that the deep diabatic heating forces leads to a frictional forcing, with a large positive wind stress curl near the center of the heating. Therefore we also force the atmosphere with a zonal wind stress frictional forcing. The wind stress forcing has a region of strong cyclonic wind stress curl with weaker anticyclonic wind stress curl to its north and south.

The wind stress field must be sufficiently displaced from the equator since the ITCZ never is centered on the equator in the East Pacific. Its annual march stays north of the equator except during some years when a DITCZ forms. Therefore, the frictional forcing is displaced north of the equator in all of the sensitivity runs, except one run, where there are two frictional forcings: one north and another south of the equator. The idealized frictional forcing for the DITCZ case are located at the same latitude and have the same amplitude for simplicity.

When a zonal wind stress curl forces the atmosphere, the steady-state solutions have the following characteristics:

- 1) The wind stress curl opposes the original flow field, as expected. This is often referred

to as spin down in the Ekman layer;

2) The majority of the atmospheric response can be attributed to Rossby waves, while the rest of the wave spectrum has a small contributing to the steady-state solution;

3) The wind stress curl imposes Ekman pumping where there was cyclonic wind stress curl, and Ekman suction where there was anticyclonic wind stress curl in the lower atmosphere, or boundary layer;

4) The vertical motion, for both Ekman pumping and Ekman suction, increases as the frictional forcing becomes more zonally-elongated;

5) Two shallow circulation cells are forced by the Ekman pumping, with the cross equatorial shallow circulation cell being broader in the meridional direction and shallower due to the large Rossby length near the equator.

Since the vertical motion is calculated using the vertical pressure-velocity, the mass transport also increases as the frictional forcing becomes more zonally-elongated. Another interesting result arises: the meridional wind anomalies experience minor changes when the wind stress curl is zonally-elongated. This is quite different from the atmospheric response to a zonally-elongated diabatic heating, where the mixed Rossby-gravity wave helps enhance the meridional wind to significantly larger values. Instead, the zonal wind anomalies increase due to the projection of the Rossby waves onto the wind stress curl. This is mainly because we have a three-dimensional model that prefers to force the zonal wind field when forced by a zonal wind stress curl. It would be interesting to see what a zonally-symmetric model's response to a zonal frictional forcing would be. In this case, we would analyze the mass flux using a more convenient parameter than the vertical pressure-velocity. We would instead use the streamfunction.

The original frictional forcing has both cyclonic and anticyclonic wind stress curl, but despite the fact that the anticyclonic wind stress curl regions have the same magnitude, the resulting magnitudes of Ekman suction are different. This can be explained by thinking about the concepts of Rossby length and Rossby depth. The Ekman suction region to the

north of the center of the frictional forcing has larger vertical motion and is narrower in the meridional direction than the Ekman suction region south of the center of the frictional forcing. The Rossby length increases as one approaches the equator because  $f \rightarrow 0$ , therefore the Ekman suction region to the north will have a smaller Rossby length, and a larger Rossby depth.

Despite the importance of the wind stress curl on the vertical pressure-velocity, the values we have calculated for our experiments involving wind stress curl are quite small when compared to the vertical motion imposed from a deep diabatic heating. In the ITCZ, there are also regions where convection is shallower, and these regions may have more intense SMC cells, depending on their vertical heating profile and other characteristics. These regions may also be affected by the wind stress curl. How they are affected is still unknown and a possible future research topic.

We also introduced a shallow diabatic heating as a forcing in our methodology, but the vertical structure of this forcing corresponds to non-precipitating clouds with a strong trade-wind inversion. The regions with this sort of vertical profile are located everywhere outside of the ITCZ region, therefore investigating their response is not as important for this particular study. However, a future model can use this diabatic heating profile.

For a future model, we propose there be a tropical region where diabatic heating in the ITCZ is prescribed to initially be either shallow precipitating or deep (bottom or top heavy), with the region outside of the ITCZ containing shallow non-precipitating heating. Sensitivity experiments where the wind stress and sea surface temperature (SST) fields can both be the initial forcing can be carried out. Therefore, the model solutions will have three main forcings: wind stress, SSTs, and diabatic heating. The linearized, equatorial  $\beta$ -plane transient model we have used in this study may be used, as well as a nonlinear version (with the addition of advection).

This model we have proposed is more complex, but still not much more complex than the model used in this study, and might gain some insight into wind stress, SSTs, diabatic

heating in the tropics, and deep versus shallow MMCs. Once we have a better grasp of these fundamental processes, we can improve our understanding of the general circulation and climate of our atmosphere.

## Appendix A

### DERIVATION FROM THE ORIGINAL PRIMITIVE EQUATIONS IN CARTESIAN COORDINATES

We begin with the quasi-static primitive equations on the equatorial  $\beta$ -plane in cartesian coordinates,

$$\frac{Du}{Dt} - \beta y v + \frac{1}{\rho} \frac{\partial p}{\partial x} = F, \quad (\text{A.1})$$

$$\frac{Dv}{Dt} + \beta y u + \frac{1}{\rho} \frac{\partial p}{\partial y} = G, \quad (\text{A.2})$$

$$\frac{\partial p}{\partial z} + \rho g = 0, \quad (\text{A.3})$$

$$\frac{\partial \rho}{\partial t} + \nabla \cdot (\rho \mathbf{V}) = 0, \quad (\text{A.4})$$

$$\frac{DT}{Dt} + \frac{1}{\rho c_p} \omega = \frac{Q}{c_p}. \quad (\text{A.5})$$

The first two equations (A.1) and (A.2) are the zonal and meridional momentum equations, respectively, (A.3) is the hydrostatic equation, (A.4) is the mass continuity equation, and (A.5) is the thermodynamic energy equation. We now define a new vertical coordinate,  $z^* = H \ln(p_0/p)$ , therefore  $p(z^*) = p_0 e^{-z^*/H}$ , and the hydrostatic equation can be rewritten as

$$\frac{\partial \phi}{\partial z^*} = \frac{RT}{H}, \quad (\text{A.6})$$

where  $\phi = gz$ , and we have used the ideal gas law  $p = \rho RT$  to simplify further. We can also use the definition of the scale height  $H = RT_0/g$  to arrive at

$$\frac{\partial \phi}{\partial z^*} = \frac{g}{T_0} T. \quad (\text{A.7})$$

This is the form of the hydrostatic equation in our new  $z^*$  vertical coordinate system. It can also be shown that

$$\frac{1}{\rho} \nabla_z p = \nabla_{z^*} \phi, \quad (\text{A.8})$$

where  $\nabla|_z, \nabla|_{z^*}$  are the horizontal gradient operators. Now we can rewrite the horizontal momentum equations (A.1) and (A.2) as

$$\frac{Du}{Dt} - \beta y v + \frac{\partial \phi}{\partial x} = F - \alpha u, \quad (\text{A.9})$$

$$\frac{Dv}{Dt} + \beta y u + \frac{\partial \phi}{\partial y} = G - \alpha v, \quad (\text{A.10})$$

which are their form in our new  $z^*$  vertical coordinate system. We have added a linear dissipation term to the horizontal frictional forcing (e.g.  $-\alpha u$ ) terms  $F$  and  $G$ , often referred to as Rayleigh frictional terms. Now we aim to write the mass continuity equation in our new coordinate system. It is convenient to write (A.4) in pressure coordinates

$$\frac{\partial u}{\partial x} + \frac{\partial v}{\partial y} + \frac{\partial \omega}{\partial p} = 0, \quad (\text{A.11})$$

where

$$\omega = -\frac{p}{H} \frac{Dz^*}{Dt} = -\frac{p}{H} w^*. \quad (\text{A.12})$$

We can rewrite  $\partial \omega / \partial p$  in terms of  $w^*$

$$\frac{\partial \omega}{\partial p} = -\frac{H}{p} \frac{\partial \omega}{\partial z^*} = \frac{\partial w^*}{\partial z^*} - \frac{w^*}{H}. \quad (\text{A.13})$$

Here is the form of the mass continuity equation in our new  $z^*$  vertical coordinate system

$$\frac{\partial u}{\partial x} + \frac{\partial v}{\partial y} + \frac{\partial w^*}{\partial z^*} - \frac{w^*}{H} = 0, \quad (\text{A.14})$$

We have yet to convert the thermodynamic equation to our new coordinate system. We first use (A.12) and  $H = RT_0/g$ , simplifying to (A.5)

$$\frac{DT}{Dt} + \frac{g}{T_0} \frac{T}{c_p} w^* = \frac{Q}{c_p}. \quad (\text{A.15})$$

If we multiply (A.15) by  $R/H$  and use  $\kappa = R/c_p$ , we obtain

$$\frac{g}{T_0} \frac{DT}{Dt} + \frac{g}{T_0} \frac{\kappa T}{H} w^* = \frac{g}{T_0} \frac{Q}{c_p}. \quad (\text{A.16})$$

We shall now introduce the Brünt Vaisala frequency

$$N^2 = \frac{g}{T_0} \left( \frac{d\bar{T}}{dz^*} + \frac{\kappa\bar{T}}{H} \right), \quad (\text{A.17})$$

where  $N^2$  is computed from a basic state temperature profile,  $\bar{T}(z)$ . Now our thermodynamic equation in the  $z^*$  coordinate system is

$$\frac{DT}{Dt} + \frac{T_0}{g} N^2 w^* = \frac{Q}{c_p} - \alpha T, \quad (\text{A.18})$$

where we have added a linear dissipation term  $-\alpha T$  often referred to as a Newtonian cooling term.

Now we have all of our primitive equations with  $z^*$  as our vertical coordinate (A.7, A.9, A.10, A.14, A.18). We now drop the  $*$  from all of the equations and linearize the equations about a basic resting state, thereby arriving at

$$\frac{\partial u}{\partial t} - \beta y v + \frac{\partial \phi}{\partial x} = F - \alpha u, \quad (\text{A.19})$$

$$\frac{\partial v}{\partial t} + \beta y u + \frac{\partial \phi}{\partial y} = G - \alpha v, \quad (\text{A.20})$$

$$\frac{\partial \phi}{\partial z} = \frac{g}{T_0} T, \quad (\text{A.21})$$

$$\frac{\partial u}{\partial x} + \frac{\partial v}{\partial y} + \frac{\partial w}{\partial z} - \frac{w}{H} = 0, \quad (\text{A.22})$$

$$\frac{\partial T}{\partial t} + \frac{T_0 N^2}{g} w = \frac{Q}{c_p} - \alpha T, \quad (\text{A.23})$$

which are the linearized primitive equations on the equatorial  $\beta$ -plane used in Chapter 2.

## Appendix B

### VERTICAL MODE TRANSFORM FOR CASE 3 WHEN $Z_T = Z_{\text{CRIT}}$

Case 3 occurs when  $\mu^2 = \lambda^2 = 0$ ,  $c = 4H^2N^2 = 210.857 \text{ m s}^{-1}$ . The second ordinary differential equation and boundary conditions that need to be solved are

$$\frac{d\Psi}{dz} = 0, \quad (\text{B.1})$$

$$\frac{d\Psi}{dz} + \frac{1}{2H}\Psi = 0 \quad \text{at } z = z_T, \quad (\text{B.2})$$

$$\frac{d\Psi}{dz} + \left( \frac{1}{2H} - \frac{N^2}{g} \right) \Psi = 0 \quad \text{at } z = 0. \quad (\text{B.3})$$

The linear solution to this set of equations is

$$\Psi(z) = Az + B. \quad (\text{B.4})$$

Now we must solve for both  $A$  and  $B$ . We use the boundary conditions

$$A + \frac{1}{2H}(Az + B) = 0 \quad \text{at } z = z_T, \quad (\text{B.5})$$

$$A + \left( \frac{1}{2H} - \frac{N^2}{g} \right) B = A + \gamma B = 0 \quad \text{at } z = 0, \quad (\text{B.6})$$

where  $\gamma = \frac{1}{2H} - \frac{N^2}{g}$ . Using B.6 we obtain

$$\Psi(z) = B(1 - \gamma z). \quad (\text{B.7})$$

In order for a nontrivial solution to be obtained from this homogeneous linear system of equations one must solve for  $z_T$  when the determinant of the matrix  $\mathcal{C}$  equals zero, where

$$\mathcal{C} = \begin{pmatrix} \frac{z_T}{2H} + 1 & \frac{1}{2H} \\ 1 & \gamma \end{pmatrix}. \quad (\text{B.8})$$

We find that  $z_T = c^2/2Hg\gamma$ , therefore we call the top height as  $z_{\text{crit}}$ . We realize that this case only needs to be used when the atmosphere's top height  $z_T$  equals  $z_{\text{crit}}$ . Our derivation is only for completeness. We have yet to solve for  $B$ , and we use properties (ii) and (iii) from Chapter 2. We normalize  $\Psi(z)$  so that

$$\int_0^{z_T} \mathcal{Z}_{\ell'}(z)\mathcal{Z}_{\ell}(z)e^{-z/H}dz = \begin{cases} 1 & \ell' = \ell, \\ 0 & \ell' \neq \ell, \end{cases} \quad (\text{B.9})$$

where  $\mathcal{Z}_{\ell}(z) = \mathcal{N}_{\ell}\Phi_{\ell}(z)e^{z/2H}$ . Since there is only one mode for this case, integrating  $\int_0^{z_T} \mathcal{Z}(z)\mathcal{Z}z)e^{-z/H}dz = 1$ , always. We use this to arrive at

$$\mathcal{N} = B = \left\{ z_{\text{crit}} \left[ 1 - \gamma z_{\text{crit}} + \frac{(\gamma z_{\text{crit}})^2}{3} \right] \right\}^{-\frac{1}{2}}, \quad (\text{B.10})$$

therefore

$$\Psi(z) = \mathcal{N}(1 - \gamma z) \quad \text{when} \quad z_T = z_{\text{crit}}. \quad (\text{B.11})$$

## Appendix C

### SKEW-HERMITIAN PROPERTY OF $\mathcal{L}$ FOR THE EQUATORIAL $\beta$ -PLANE

Consider the matrix operator

$$\mathcal{L} = \begin{pmatrix} 0 & -\beta y & im/a \\ \beta y & 0 & \partial/\partial y \\ c_\ell^2 im/a & c_\ell^2 \partial/\partial y & 0 \end{pmatrix}, \quad (\text{C.1})$$

and the inner product of any two vectors  $\mathbf{f}(y)$  and  $\mathbf{g}(y)$

$$(\mathbf{f}, \mathbf{g}) = \int_{-\infty}^{\infty} (f_1 g_1^* + f_2 g_2^* + \frac{1}{c_\ell^2} f_3 g_3^*) dy, \quad (\text{C.2})$$

where \* denotes the complex conjugate. We want to prove that the matrix operator  $\mathcal{L}$  is skew-Hermitian with respect to the inner product (C.2) first. Skew-Hermitian means that  $\mathcal{L}^\dagger = -\mathcal{L}$ , where  $\mathcal{L}^\dagger$ , the adjoint of  $\mathcal{L}$ , is defined by

$$(\mathcal{L}\mathbf{f}, \mathbf{g}) = (\mathbf{f}, \mathcal{L}^\dagger \mathbf{g}). \quad (\text{C.3})$$

Let's first figure out the form of  $\mathcal{L}^\dagger$ . We first note that

$$\mathcal{L}\mathbf{f} = \begin{pmatrix} 0 & -\beta y & im/a \\ \beta y & 0 & \partial/\partial y \\ c_\ell^2 im/a & c_\ell^2 \partial/\partial y & 0 \end{pmatrix} \begin{pmatrix} f_1 \\ f_2 \\ f_3 \end{pmatrix} = \begin{pmatrix} -\beta y f_2 + im f_3/a \\ \beta y f_1 + \partial f_3/\partial y \\ c_\ell^2 im f_1/a + c_\ell^2 \partial f_2/\partial y \end{pmatrix}. \quad (\text{C.4})$$

Then

$$(\mathcal{L}\mathbf{f}, \mathbf{g}) = \int_{-\infty}^{\infty} \left[ \left( -\beta y f_2 + \frac{1}{c_\ell^2} \frac{im}{a} f_3 \right) g_1^* + \left( \beta y f_1 + \frac{1}{c_\ell^2} \frac{\partial f_3}{\partial y} \right) g_2^* + \left( \frac{im}{a} f_1 + \frac{\partial f_2}{\partial y} \right) g_3^* \right] dy. \quad (\text{C.5})$$

After integrating the two derivative terms by parts, applying the boundary conditions, and rearranging, we obtain

$$(\mathcal{L}\mathbf{f}, \mathbf{g}) = \int_{-\infty}^{\infty} \left[ f_1 \left( \beta y g_2 - \frac{im}{a} g_3 \right)^* + f_2 \left( -\beta y g_1 - \frac{\partial g_3}{\partial y} \right)^* + \frac{f_3}{c_\ell^2} \left( -\frac{im}{a} g_1 - \frac{\partial g_2}{\partial y} \right)^* \right] dy. \quad (\text{C.6})$$

By the definition (C.3), the right hand side of (C.6) is  $(\mathbf{f}, \mathcal{L}^\dagger \mathbf{g})$ , so that

$$\mathcal{L}^\dagger = \begin{pmatrix} 0 & \beta y & -im/a \\ -\beta y & 0 & -\partial/\partial y \\ -c_\ell^2 im/a & -c_\ell^2 \partial/\partial y & 0 \end{pmatrix}. \quad (\text{C.7})$$

Since the comparison of (C.7) with (C.1) yields  $\mathcal{L}^\dagger = -\mathcal{L}$ , we have proved that  $\mathcal{L}$  is skew-Hermitian with respect to the inner product (C.2).

We now prove that the eigenfunctions of  $\mathcal{L}$  are orthogonal and that the eigenvalues of  $\mathcal{L}$  are pure imaginary. Let  $\mathbf{K}_{\ell mnr}(\hat{y}_\ell)$  and  $\mathbf{K}_{\ell' m' n' r'}(\hat{y}_\ell)$  represent two eigenfunctions of  $\mathcal{L}$ , i.e.,

$$\mathcal{L}\mathbf{K}_{\ell mnr} + i\nu_{\ell mnr}\mathbf{K}_{\ell mnr} = 0, \quad (\text{C.8})$$

$$\mathcal{L}\mathbf{K}_{\ell' m' n' r'} + i\nu_{\ell' m' n' r'}\mathbf{K}_{\ell' m' n' r'} = 0. \quad (\text{C.9})$$

Taking the inner product of (C.8) with  $\mathbf{K}_{\ell' m' n' r'}(\hat{y}_\ell)$ , and taking the inner product of  $\mathbf{K}_{\ell mnr}(\hat{y}_\ell)$  with (C.9), we obtain

$$(\mathcal{L}\mathbf{K}_{\ell mnr}, \mathbf{K}_{\ell' m' n' r'}) + (i\nu_{\ell mnr}\mathbf{K}_{\ell mnr}, \mathbf{K}_{\ell' m' n' r'}) = 0, \quad (\text{C.10})$$

$$(\mathbf{K}_{\ell mnr}, \mathcal{L}\mathbf{K}_{\ell' m' n' r'}) + (\mathbf{K}_{\ell mnr}, i\nu_{\ell' m' n' r'}\mathbf{K}_{\ell' m' n' r'}) = 0. \quad (\text{C.11})$$

Using the skew-Hermitian property of  $\mathcal{L}$ , (C.10) and (C.11) become

$$-(\mathbf{K}_{\ell mnr}, \mathcal{L}\mathbf{K}_{\ell' m' n' r'}) + i\nu_{\ell mnr}(\mathbf{K}_{\ell mnr}, \mathbf{K}_{\ell' m' n' r'}) = 0, \quad (\text{C.12})$$

$$(\mathbf{K}_{\ell mnr}, \mathcal{L}\mathbf{K}_{\ell' m' n' r'}) - i\nu_{\ell' m' n' r'}^*(\mathbf{K}_{\ell mnr}, \mathbf{K}_{\ell' m' n' r'}) = 0. \quad (\text{C.13})$$

The sum of (C.12) and (C.13) yields

$$(\nu_{\ell mnr} - \nu_{\ell' m' n' r'}^*)(\mathbf{K}_{\ell mnr}, \mathbf{K}_{\ell' m' n' r'}) = 0. \quad (\text{C.14})$$

If  $\ell = \ell'$ ,  $m = m'$ ,  $n = n'$ , and  $r = r'$ , then  $(\mathbf{K}_{\ell mnr}, \mathbf{K}_{\ell mnr}) \neq 0$  and we conclude from (C.14) that  $\nu_{\ell mnr} = \nu_{\ell mnr}^*$ , i.e.,  $\nu_{\ell mnr}$  is a pure real number, or, equivalently, the eigenvalue  $i\nu_{\ell mnr}$  is pure imaginary. If  $\nu_{\ell mnr} \neq \nu_{\ell' m' n' r'}$ , we conclude from (C.14) that  $(\mathbf{K}_{\ell mnr}, \mathbf{K}_{\ell' m' n' r'}) = 0$ , i.e., the eigenfunctions corresponding to distinct eigenvalues are orthogonal. If the eigenfunctions are appropriately normalized we then obtain the orthonormality relation

$$(\mathbf{K}_{\ell mnr}(\hat{y}_\ell), \mathbf{K}_{\ell' m' n' r'}(\hat{y}_\ell)) = \begin{cases} 1 & \text{if } (\ell' m' n' r') = (\ell mnr) \\ 0 & \text{if } (\ell' m' n' r') \neq (\ell mnr) \end{cases}. \quad (\text{C.15})$$

We can expand  $\hat{\mathbf{w}}(y, t)$  in a series of the basis functions  $\mathbf{K}_{\ell mnr} \hat{y}_\ell$ , i.e.,

$$\hat{\mathbf{w}}(y, t) = \sum_{\ell mnr} \hat{w}_{\ell mnr}(t) \mathbf{K}_{\ell mnr}(\hat{y}_\ell). \quad (\text{C.16})$$

This can be considered a generalization of the familiar Fourier series, with the scalar coefficients  $\hat{w}_{\ell mnr}(t)$  being the analog of the Fourier coefficients and the vector basis functions  $\mathbf{K}_{\ell mnr}(\hat{y}_\ell)$  being the analog of the Fourier basis functions (sines and cosines). Recall that all transforms come in pairs, e.g., the Fourier series involving a sum and the formula for the Fourier coefficients, involving an integral. Thus, (C.16) must have a companion, i.e., an integral formula to compute the coefficient  $\hat{w}_{\ell mnr}(t)$  from  $\hat{\mathbf{w}}(y, t)$ . We can obtain this companion formula from (C.16) and the orthonormality relation (C.15) as follows. Take the inner product of (C.16) with  $\mathbf{K}_{\ell' m' n' r'}(\hat{y}_\ell)$  to obtain

$$(\hat{\mathbf{w}}(y, t), \mathbf{K}_{\ell' m' n' r'}(\hat{y}_\ell)) = \sum_{\ell mnr} \hat{w}_{\ell mnr}(t) (\mathbf{K}_{\ell mnr} \hat{y}_\ell, \mathbf{K}_{\ell' m' n' r'} \hat{y}_\ell) = \hat{w}_{\ell' m' n' r'}(t). \quad (\text{C.17})$$

From the first and last parts of (C.17), we obtain

$$\hat{w}_{\ell mnr}(t) = (\hat{\mathbf{w}}(y, t), \mathbf{K}_{\ell mnr}(\hat{y}_\ell)). \quad (\text{C.18})$$

Equations (C.16) and (C.18) form a transform pair.

Now consider the computation of the normalization factor for the eigenfunctions of

the operator  $\mathcal{L}$ . Consider first the eigenfunction  $\mathbf{K}_{\ell mnr}(\hat{y}_\ell)$  for the  $n = -1$  case

$$\mathbf{K}_{\ell mnr}(\hat{y}_\ell) = A_{\ell mnr} e^{-\frac{1}{2} \text{hat} y_\ell^2} \begin{pmatrix} 1 \\ 0 \\ c_\ell \end{pmatrix}.$$

Using the definition of inner product (C.2) we have

$$(\mathbf{K}_{\ell mnr}(\hat{y}_\ell), \mathbf{K}_{\ell mnr}(\hat{y}_\ell)) = 2|A_{\ell mnr}|^2 \int_{-\infty}^{\infty} e^{-\hat{y}_\ell^2} d\hat{y}_\ell,$$

where  $|A_{\ell mnr}|^2$  represents the modulus square of the normalization constant. For normalization we want  $(\mathbf{K}_{\ell mnr}(\hat{y}_\ell), \mathbf{K}_{\ell mnr}(\hat{y}_\ell))$  to be unity. The value of the integral of  $e^{-\hat{y}_\ell^2}$  between  $\pm\infty$  is equal to  $\pi^{\frac{1}{2}}$ , so the normalization constant  $A_{\ell mnr}$  is

$$A_{\ell mnr} = 2^{-\frac{1}{2}} \pi^{-\frac{1}{4}} \quad (\text{C.19})$$

for the case  $n = -1$ .

For the general case  $n \geq 0$  we have to do a little more work. First we need to find a result involving the integral of two Hermite polynomials. Consider the functions  $\mathcal{Y}_n = e^{-\frac{1}{2}y^2} H_n(y)$  and  $\mathcal{Y}_{n'} = e^{-\frac{1}{2}y^2} H_{n'}(y)$ . These satisfy

$$\frac{d^2 \mathcal{Y}_n}{dy^2} + (2n + 1 - y^2) \mathcal{Y}_n = 0,$$

$$\frac{d^2 \mathcal{Y}_{n'}}{dy^2} + (2n' + 1 - y^2) \mathcal{Y}_{n'} = 0.$$

Multiplying the first equation by  $\mathcal{Y}_{n'}$  and the second one by  $\mathcal{Y}_n$  and subtracting one from the other, we obtain

$$\frac{d}{dy} \left( \mathcal{Y}_{n'} \frac{d\mathcal{Y}_n}{dy} - \mathcal{Y}_n \frac{d\mathcal{Y}_{n'}}{dy} \right) + 2(n - n') \mathcal{Y}_n \mathcal{Y}_{n'} = 0.$$

If we integrate this over the whole domain, the boundary terms vanish and we're left with

$$2(n - n') \int_{-\infty}^{\infty} \mathcal{Y}_n \mathcal{Y}_{n'} dy = 2(n - n') \int_{-\infty}^{\infty} e^{-y^2} H_n(y) H_{n'}(y) dy = 0.$$

When  $n \neq n'$  the integral must vanish, while for  $n = n'$  the value is a finite number which depends on  $n$ , so that

$$\int_{-\infty}^{\infty} e^{-y^2} H_n(y) H_{n'}(y) dy = \begin{cases} \pi^{\frac{1}{2}} 2^n n! & \text{if } n = n' \\ 0 & \text{if } n \neq n'. \end{cases} \quad (\text{C.20})$$

Now we are ready to compute the normalization factor for the general  $n \geq 0$ . For  $n \geq 0$  the eigenfunction  $\mathbf{K}_{\ell mnr}(\hat{y}_\ell)$  is given by

$$\mathbf{K}_{\ell mnr}(\hat{y}_\ell) = A_{\ell mnr} \begin{pmatrix} \epsilon_\ell^{\frac{1}{4}} \left[ \left( \frac{n+1}{2} \right)^{\frac{1}{2}} \left( \epsilon_\ell^{\frac{1}{2}} \hat{\nu}_{\ell mnr} + m \right) \mathcal{H}_{n+1}(\hat{y}_\ell) + \left( \frac{n}{2} \right)^{\frac{1}{2}} \left( \epsilon_\ell^{\frac{1}{2}} \hat{\nu}_{\ell mnr} - m \right) \mathcal{H}_{n-1}(\hat{y}_\ell) \right] \\ -i \left( \epsilon_\ell \hat{\nu}_{\ell mnr}^2 - m^2 \right) \mathcal{H}_n(\hat{y}_\ell) \\ c_\ell \epsilon_\ell^{\frac{1}{4}} \left[ \left( \frac{n+1}{2} \right)^{\frac{1}{2}} \left( \epsilon_\ell^{\frac{1}{2}} \hat{\nu}_{\ell mnr} + m \right) \mathcal{H}_{n+1}(\hat{y}_\ell) - \left( \frac{n}{2} \right)^{\frac{1}{2}} \left( \epsilon_\ell^{\frac{1}{2}} \hat{\nu}_{\ell mnr} - m \right) \mathcal{H}_{n-1}(\hat{y}_\ell) \right] \end{pmatrix}.$$

If we take the inner product of  $\mathbf{K}_{\ell mnr}(y)$  with itself, and apply (C.20), we have

$$\begin{aligned} (\mathbf{K}_{\ell mnr}(\hat{y}_\ell), \mathbf{K}_{\ell mnr}(\hat{y}_\ell)) &= |A_{\ell mnr}|^2 \int_{-\infty}^{\infty} e^{-\hat{y}_\ell^2} \left[ -\epsilon_\ell^{1/2} (n+1) \left( \epsilon_\ell^{1/2} \hat{\nu}_{\ell mnr} + m \right)^2 \left( \pi^{1/2} 2^{n+1} (n+1)! \right)^{-1} H_{n+1}(\hat{y}_\ell) H_{n+1}(\hat{y}_\ell) \right. \\ &\quad + \left. \left( \epsilon_\ell \hat{\nu}_{\ell mnr}^2 - m^2 \right)^2 \left( \pi^{1/2} 2^n (n)! \right)^{-1} H_n(\hat{y}_\ell) H_n(\hat{y}_\ell) \right. \\ &\quad \left. - \epsilon_\ell^{1/2} n \left( \epsilon_\ell^{1/2} \hat{\nu}_{\ell mnr} - m \right)^2 \left( \pi^{1/2} 2^{n-1} (n-1)! \right)^{-1} H_{n-1}(\hat{y}_\ell) H_{n-1}(\hat{y}_\ell) \right] d\hat{y}_\ell = \\ &|A_{\ell mnr}|^2 \left[ -\epsilon_\ell^{1/2} (n+1) \left( \epsilon_\ell^{1/2} \hat{\nu}_{\ell mnr} + m \right)^2 + n \left( \epsilon_\ell^{1/2} \hat{\nu}_{\ell mnr} - m \right)^2 - \epsilon_\ell^{1/2} \left( \hat{\nu}_{\ell mnr}^2 - m^2 \right)^2 \right]. \end{aligned}$$

Since we want the inner product  $(\mathbf{K}_{\ell mnr}(\hat{y}_\ell), \mathbf{K}_{\ell mnr}(\hat{y}_\ell))$  to equal unity,  $A_{\ell mnr}$  must satisfy

$$A_{\ell mnr} = \left[ \epsilon_\ell^{\frac{1}{2}} (n+1) \left( \epsilon_\ell^{\frac{1}{2}} \nu_{\ell mnr} + m \right)^2 + \epsilon_\ell^{\frac{1}{2}} n \left( \epsilon_\ell^{\frac{1}{2}} \nu_{\ell mnr} - m \right)^2 + \left( \epsilon_\ell \nu_{\ell mnr}^2 - m^2 \right)^2 \right]^{-\frac{1}{2}}. \quad (\text{C.21})$$

In summary, combining the results (C.19) and (C.21), we have

$$\begin{aligned}
 A_{\ell mnr} = & \\
 & \begin{cases} \left[ \epsilon_{\ell}^{\frac{1}{2}} (n+1) \left( \epsilon_{\ell}^{\frac{1}{2}} \nu_{\ell mnr} + m \right)^2 + \epsilon_{\ell}^{\frac{1}{2}} n \left( \epsilon_{\ell}^{\frac{1}{2}} \nu_{\ell mnr} - m \right)^2 + (\epsilon_{\ell} \nu_{\ell mnr}^2 - m^2)^2 \right]^{-\frac{1}{2}}, & n \geq 0 \\ 2^{-\frac{1}{2}} \pi^{-\frac{1}{4}}, & n = -1, \end{cases} \\
 & \hspace{20em} \text{(C.22)}
 \end{aligned}$$

## BIBLIOGRAPHY

- Back, L. E., and C. S. Bretherton, 2009: On the relationship between SST gradients, boundary layer winds, and convergence over the tropical oceans. *J. Climate*, **29**, 4182–4196.
- Blandford, R., 1966: Mixed Rossby-gravity waves in the ocean. *Deep-Sea Res.*, **13**, 941–961.
- DeMaria, M., 1985: Linear response of a stratified tropical atmosphere to convective forcing. *J. Atmos. Sci.*, **142**, 1944–1959.
- Fulton, S. R., 1980: Geostrophic adjustment in a stratified atmosphere. Master’s thesis, Colorado State University, 97 pp.
- Fulton, S. R., and W. H. Schubert, 1985: Vertical normal mode transforms: Theory and application. *Mon. Wea. Rev.*, **113**, 647–658.
- Gill, A. E., 1980: Some simple solutions for heat-induced tropical circulation. *Quart. J. Roy. Meteor. Soc.*, **16**, 447–462.
- Gill, A. E., and P. J. Philips, 1986: Nonlinear effects on heat-induced circulation of the tropical atmosphere. *Quart. J. Roy. Meteor. Soc.*, **112**, 69–92.
- Hack, J. J., and W. H. Schubert, 1990: Some dynamical properties of idealized thermally-forced meridional circulations in the tropics. *Meteorol. Atmos. Phys.*, **44**, 101–117.
- Hack, J. J., W. H. Schubert, D. E. Stevens, and H.-C. Kwo, 1989: Response of the Hadley circulation to convective forcing in the ITCZ. *J. Atmos. Sci.*, **46**, 2957–2973.
- Held, I. M., 2005: The gap between simulation and understanding in climate modeling. *Bull. Amer. Meteor. Soc.*, **29**, 1609–1614.
- Lindzen, R. S., and S. Nigam, 1987: On the role of sea surface temperature gradients in forcing low-level winds and convergence in the tropics. *J. Atmos. Sci.*, **44**, 2418–2436.
- Matsuno, T., 1966: Quasi-Geostrophic motions in the equatorial area. *J. Meteor. Soc. Japan*, **44**, 25–43.
- Milliff, R. F., and J. Morzel, 2001: The global distribution of the time-average wind stress curl from NSCAT. *J. Atmos. Sci.*, **58**, 109–131.
- Mora, G., 2008: Low-level jets in the tropical Americas. Master’s thesis, Colorado State University, 110 pp.

- Morse, P. M., and H. Feshbach, 1953: *Methods of Theoretical Physics, Part I*. New York: McGraw-Hill, 657 pp.
- Nitta, T., and S. Esbensen, 1974: Heat and moisture budget analyses using BOMEX data. *Mon. Wea. Rev.*, **102**, 17–28.
- Nolan, D. S., S. W. Powell, C. Zhang, and B. E. Mapes, 2010: Idealized simulations of the Intertropical Convergence Zone and its multilevel flows. *J. Atmos. Sci.*, **67**, 4028–4053.
- Nolan, D. S., C. Zhang, and S. hua Chen, 2007: Dynamics of the Shallow Meridional Circulation around Intertropical Convergence Zones. *J. Atmos. Sci.*, **64**, 2262–2285.
- Raupp, C. F. M., and P. L. Silva Dias, 2006: Dynamics of resonantly interacting equatorial waves. *Tellus*, **58A**, 263–279.
- Risien, C. M., and D. B. Chelton, 2008: A global climatology of surface wind and wind stress fields from eight years of QuikSCAT scatterometer data. *J. Phys. Oceanogr.*, **38**, 2379–2413.
- Schneider, E. K., and R. S. Lindzen, 1977: Axially symmetric steady-state models of the basic state for instability and climate studies. i. Linearized calculations. *J. Atmos. Sci.*, **34**, 263–279.
- Schubert, W. H., and M. T. Masarik, 2006: Potential vorticity aspects of the MJO. *Dynam. Atmos. Oceans*, **42**, 127–151. Doi: 10.1016/j.dynatmoce.2006.02.003.
- Schubert, W. H., and B. D. McNoldy, 2010: Application of the concepts of Rossby length and Rossby depth to tropical cyclone dynamics. *J. Adv. Model. Earth. Syst.*, **2**, Art. 7, 13 pp. Doi:10.3894/JAMES.2010.2.7.
- Silva Dias, P. L., W. H. Schubert, and M. DeMaria, 1983: Large-scale response of the tropical atmosphere to transient convection. *J. Atmos. Sci.*, **40**, 2689–2707.
- Stevens, B., J. J. Duan, J. C. McWilliams, M. Münnich, and J. D. Neelin, 2002: Entrainment, Rayleigh friction, and boundary layer winds over the tropical Pacific. *J. Climate*, **15**, 30–44.
- Trenberth, K. E., D. P. Stepaniak, and J. M. Caron, 2000: The global monsoon as seen through the divergent atmospheric circulation. *J. Climate*, **13**, 3969–3993.
- Waliser, D. E., and C. Gautier, 1993: A satellite-derived climatology of the ITCZ. *J. Climate*, **6**, 2162–2174.
- Wallace, J. M., T. P. Mitchell, and C. Deser, 1989: The influence of sea-surface temperature upon surface wind in the eastern equatorial Pacific: Seasonal and interannual variability. *J. Climate*, **2**, 1492–1499.
- Webster, P. J., 1972: Response of the tropical atmosphere to steady forcing. *Mon. Wea. Rev.*, **100**, 518–541.
- Wu, Z., 2003: A shallow CISK, deep equilibrium mechanism for the interaction between large-scale convection and large-scale circulations in the tropics. *J. Atmos. Sci.*, **60**, 377–392.

- Yanai, M., S. Esbensen, and J.-H. Chu, 1973: Determination of bulk properties of tropical cloud clusters from large-scale heat and moisture budgets. *J. Atmos. Sci.*, **30**, 611–627.
- Žagar, N., 2004: Dynamical aspects of atmospheric data assimilation in the tropics. Ph.D. thesis, Stockholm: Universitetservice, 45 pp.
- Zhang, C., M. McGauley, and N. A. Bond, 2004: Shallow Meridional Circulation in the tropical eastern Pacific. *J. Climate*, **17**, 133–139.
- Zhang, C., D. S. Nolan, C. D. Thorncroft, and H. Nguyen, 2008: Shallow Meridional Circulations in the tropical atmosphere. *J. Climate*, **64**, 3453–3470.
- Zhang, C., P. Woodworth, and G. Gu, 2006: The seasonal cycle in the lower troposphere over west Africa from sounding observations. *J. Climate*, **132**, 2559–2582.